


2022

Heterogeneous oxidation of multi-component aqueous organic aerosols: The effect of transport phenomena and reaction compartment on reaction kinetics.

Tadini wenyika Masaya
West Virginia University, tm0082@mix.wvu.edu

Follow this and additional works at: <https://researchrepository.wvu.edu/etd>

 Part of the [Analytical Chemistry Commons](#), [Computational Chemistry Commons](#), and the [Physical Chemistry Commons](#)

Recommended Citation

Masaya, Tadini wenyika, "Heterogeneous oxidation of multi-component aqueous organic aerosols: The effect of transport phenomena and reaction compartment on reaction kinetics." (2022). *Graduate Theses, Dissertations, and Problem Reports*. 11505.
<https://researchrepository.wvu.edu/etd/11505>

This Dissertation is protected by copyright and/or related rights. It has been brought to you by the The Research Repository @ WVU with permission from the rights-holder(s). You are free to use this Dissertation in any way that is permitted by the copyright and related rights legislation that applies to your use. For other uses you must obtain permission from the rights-holder(s) directly, unless additional rights are indicated by a Creative Commons license in the record and/ or on the work itself. This Dissertation has been accepted for inclusion in WVU Graduate Theses, Dissertations, and Problem Reports collection by an authorized administrator of The Research Repository @ WVU. For more information, please contact researchrepository@mail.wvu.edu.

Heterogeneous oxidation of multi-component aqueous organic aerosols: The effect of transport phenomena and reaction compartment on reaction kinetics.

Tadini Wenyika Masaya

Dissertation submitted to the Eberly College of Arts and Sciences
at West Virginia University
in partial fulfilment of the requirement
for the degree of
Doctor of Philosophy
In
Chemistry

Fabien Goulay, Ph.D.

Blake Mertz, Ph.D.

Justin Legleiter, Ph.D.

Stephen J Valentine, Ph.D.

Dady Dadyburjor, Ph.D.

C. Eugene Bennett Department of Chemistry
Morgantown, West Virginia
2022

Keywords: Aqueous organic aerosols, molecular dynamics simulation, reactive uptake coefficient, interfacial reaction, solvation, reaction Kinetics, partitioning, rate coefficients, Bulk Composition, molecule orientation.

Copyright 2022 Tadini Wenyika Masaya

Abstract

Heterogeneous oxidation of multi-component aqueous organic aerosols: The effect of transport phenomena and reaction compartment on reaction kinetics.

Tadini Wenyika Masaya

The surface-bulk partitioning of small organic molecules in aqueous droplets was investigated using molecular dynamics. The air-particle interface was modeled using a 80-Å cubic water box containing series of organic molecules and surrounded by gaseous OH radicals. The properties of the organic solutes within the interface and the water-bulk were examined at a molecular-level using density profiles and radial pair distribution functions. Molecules containing only polar functional groups such as urea and glucose are found predominantly in the water bulk, forming an exclusion layer near the water surface. Substitution of a single polar group by an alkyl group in sugars and amides leads to the migration of the molecule toward the interface. Within the first 2 nm from the water surface, surface-active solutes lose their rotational freedom and adopt a preferred orientation with the alkyl group pointing toward the surface. The different packing within the interface leads to different solvation shell structures and enhanced interaction between the organic molecules and absorbed OH radicals. The simulations provide quantitative information about the dimension, composition, and organization of the air-water interface as well as about the non-reactive interaction of the OH radicals with the organic solutes. It reveals that the enhanced reactivity of surface-active molecules is due to increased concentrations, preferred orientation, and decreased solvation near the air-water surface. The results are important to explain how heterogeneous oxidation mechanisms and kinetics within interfaces may differ from those of the bulk.

An atmospheric pressure flow-tube reactor coupled with offline GC-MS analysis techniques was used to determine the kinetics of the OH-initiated oxidation of equimolar aqueous organic aerosol. Saccharides (glucose and MGP) and amides (propionamide, urea, and acetamide), were chosen as model molecules because of their partitioning properties, availability in the atmosphere, and the important role they play in atmospheric chemistry. The decay rates of the solutes (saccharides and amides) were determined by measuring the loss in signal of solutes in

the particle phase as a function of OH exposure (time-integrated total concentration of OH radical). The reactivity of MGP towards OH radicals was shown to be higher in the presence of urea (a surface in-active molecule) than when in the presence of propionamide (a surface in-active molecule). The decreases in MGP reactivity was shown by the change in rate coefficients from $1.2(\pm 0.1) \times 10^{-11} \text{ cm}^{-3} \text{ s}^{-1}$ in the urea-MGP particles to $4.7(\pm 0.3) \times 10^{-12} \text{ cm}^{-3} \text{ s}^{-1}$ in the propionamide-MGP particles. These findings highlight the importance of surface interactions over bulk interactions in determining the reaction rate of reactive species in aqueous aerosols. The change in particle size with change in chemical composition was also demonstrated.

Acknowledgments

I would like to express my deepest gratitude to my advisor, Dr Fabien Goulay, for his inspirational mentorship and unwavering support throughout the entirety of my Graduate studies. I greatly appreciate how he encouraged and assisted me to explore new frontiers. I am also thankful for all the assistance you gave me to allow me to meet other non-academic needs. I am greatly indebted to Dr Blake Mertz and the Mertz group for their support and assistance with the computational aspects of my research. I am also grateful for the feedback and assistance I got from my committee members, Dr Stephen Valentine, Dr Dady Dadyburjor, and Dr Justin Legleiter. My gratitude also goes to the past and present members of the Goulay group. I would also like to thank the staff of the C. Eugene Bennett Department of Chemistry for their assistance rendered in different ways.

Finally, I would like to express my deepest thanks to my family and friends, especially my wife, for their material and emotional support.

Table of Contents

Abstract	ii
List of Figures	xii
List of Table	xix

Chapter 1: Introduction

1.1 Chemical species in the atmosphere	1
1.1.1 Oxidants	1
1.1.2 Organics	2
1.2 Atmospheric aerosols.....	2
1.2.1 Formation of atmospheric particles.....	3
1.2.1.1 Amides and Saccharides in atmospheric aerosols.....	4
1.2.2 Chemical, physical, and optical properties Atmospheric aerosol particle	5
1.2.2.1 Chemical properties.....	5
1.2.2.2 Physical properties	6
1.2.2.3 Optical properties	7
1.3 Chemistry of the interface: Heterogeneous chemistry of atmospheric organic aerosol particles.....	9
1.3.1 Liquid surface.....	9
1.3.2 Thermodynamics of gas-liquid interfaces	10
1.3.3 Reaction mechanisms and kinetics of heterogeneous oxidation of atmospheric particles	

1.3.4	The reactive uptake coefficient (γ).....	12
1.3.5	Chemistry reactions in the bulk-phase and at the air-water(liquid) interface	15
1.4	Drastic changes to chemistry at the interface of spherical particles	17
1.5	MD simulation of the interface: A computational look at the Gas- liquid interface	19
1.5.1	Classical Computational methodologies	20
1.5.2	Properties of the gas-liquid interface	22
1.6	The aims and objectives of this thesis.....	23

Chapter 2: Experimental methods, theoretical simulations, and models

2.1	Overall experimental setup	54
2.1.1	Physical Particle Characterization: Scanning Mobility Particle Sizer	56
2.1.2	Particle Composition Characterization: GC-MS analysis.....	59
2.1.3	Relative Rate Measurements in Gas-phase Reactions: GC-FID and Hexane.....	59
2.1.4	Reactive uptake measurement.....	61
2.2	Molecular Dynamics Algorithms: (MD) Simulations setup.....	63
2.2.1	Periodic Boundary Conditions	63
2.2.2	Thermostats and Barostats (Temperature and Pressure Control).....	65
2.2.3	Ensembles.....	65
2.2.4	Langevin Dynamics.....	66
2.2.5	Initial Conditions.....	66

2.2.6	Numerical Integration	67
2.2.7	Integration Timestep	67
2.2.8	Minimization	68
2.3	Inter-atomic Interactions and Force Fields	68
2.3.1	Bonded Interaction	68
2.3.2	Non-Bonded Interaction	69
2.3.3	Polarization	71
2.3.4	Several Force Fields and Water Models	71
2.4	Software Packages	72
2.4.1	MD Simulation Software	72

Chapter 3: A molecular dynamics study of the effects of partitioning on the OH radical interaction with solutes in multicomponent aqueous aerosols

3.1	Introduction	80
3.2	Methods	85
3.2.1	Molecular dynamic	85
3.2.2	Data analysis	87
3.3	Model validation	88
3.4	Results and Discussion	93
3.4.1	Organic solute density profiles	93

3.4.2	Molecular orientation	97
3.4.3	Interfacial solvation and OH-solute interactions.....	100
3.5	Conclusion and implications for atmospheric heterogeneous chemistry.....	103

Chapter 4: Method development and validation of a reverse phase gas chromatographic methods (GC-MS) for the simultaneous quantification of saccharides and amides.

4.1	Introduction.....	125
4.2	Materials and methods	126
4.2.1	Instrumentation and conditions	126
4.2.1.1	GC-MS conditions.....	127
4.2.2	Reagents and Chemicals.....	127
4.2.2.1	Preparation of Stock solution and calibration Standard solutions.....	128
4.2.3	Aqueous organic aerosol collection and preparation (actual sample).....	129
4.2.4	Derivatization.....	129
4.2.4.1	BSA Silylation.....	130
4.2.4.2	BSA-TMCS Silylation	130
4.2.5	Preparation of Calibration Curves.....	131
4.2.5.1	Calibration Curves for MGP-Urea-Xylose method: Internal standard xylose.....	131
4.2.5.2	Calibration Curves for MGP-Propionamide-Urea method: Internal standard urea	132
4.2.5.3	Calibration Curves for Propionamide-Urea-MGP method: Internal standard MGP ...	132

4.3	Method Validation	132
4.3.1	Specificity.....	132
4.3.1.1	Identity	132
4.3.1.2	Assay Tests.....	133
4.3.2	Precision.....	133
4.3.2.1	Repeatability.....	133
4.3.2.2	Intermediate Precision.....	133
4.3.3	Linearity	133
4.3.4	Detection Limit	134
4.3.4.1	Visual Evaluation	134
4.3.4.2	Standard Deviation of the Response and the slope	134
4.3.5	Quantitation Limit.....	134
4.3.5.1	Visual Evaluation	134
4.3.5.2	Standard Deviation of the Response and the slope	134
4.3.6	Robustness.....	135
4.3.7	Accuracy.....	135
4.4	Results and Discussion	135
4.4.1	Method Development.....	135
4.4.1.1	Optimization of silylation derivatization.....	135
4.4.1.2	Optimization of GC-MS parameters	139

4.4.1.2.1	MGP-Urea-Xylose method.....	139
4.4.1.2.2	MGP-Propionamide-Urea method and Propionamide-Urea-MGP method	140
4.4.2	Method Validation.....	141
4.4.2.1	Specificity.....	142
4.4.2.1.1	Identity.....	142
4.4.2.1.2	Assay Tests.....	147
4.4.2.2	Precision.....	148
4.4.2.2.1	Repeatability.....	148
4.4.2.2.2	Intermediate Precision	149
4.4.2.3	Calibration Curves, Linearity, Range, L.O.D and L.O.Q	151
4.4.3	Analysis of a real sample	155
4.5	Conclusion	155

Chapter 5: Heterogeneous oxidation of multi-component aqueous organic aerosols

5.1	Introduction.....	164
5.2	MD simulation	166
5.3	Experimental results.....	167
5.3.1	Particle size characterization.....	167
5.3.2	Kinetic results.....	174
5.4	Discussion.....	177

5.4.1	Particle characterization	177
5.4.2	Kinetics.....	179
5.5	Conclusion	182

Chapter 6: Conclusion

6.1	MD simulation studies	189
6.2	The kinetics of OH+aqueous organic particles	190
	Appendix A.....	192

List of Figures

Figure 1.1 Schematic of gasSOA and aqSOA formation pathways in the gas and aqueous phases of the atmosphere. Dashed arrows denote oxidation reactions. ^{56,60}	4
Figure 1.2 Viscosities and the corresponding phases of atmospheric aerosol particles. All the images used are from http://www.google.com.image	6
Figure 1.3 Interaction of an atmospheric aerosol particle with solar radiation.....	8
Figure 1.4 Generalized illustration of the processes occurring at the liquid surface and involved in the heterogeneous oxidation of an aqueous organic aerosol particle.....	10
Figure 1.5 (1) Diagram of the Langmuir-Hinshelwood (L-H) reaction G (gas-phase reactants) + B (bulk molecule) \rightarrow P (products). The G need to adsorb on the surface (a) before reacting to form P (b), which may remain on the surface (c) or desorb (d). (2) Diagram of the Eley-Rideal (E-R) reaction, the G does not adsorb onto the surface prior to reaction (a, b). The P may remain on the surface (c) or desorb (d). ^{137,138}	14
Figure 1.6 A schematic of two reaction channels (surface heterogeneous reaction and bulk homogeneous reaction) for gas-phase oxidants reacting with organic reactive reactants in the aqueous droplet. A_s and A_b are the reactive organic species at the surface of aqueous droplet and in the bulk of droplet. Oxs and Oxb are the gas-phase oxidants at the surface of aqueous droplet and in the bulk of droplet. P is the product. ¹⁴⁸	17
Figure 1.7 The Molecular Dynamics simulation procedure.	22
Figure 2.1 A depiction of the experimental setup used for the offline kinetics studies of the heterogeneous oxidation of aqueous organic aerosol particles.....	56
Figure 2.2 Schematic of the components making up the particle classifying system. ²	58

Figure 3.1 Initial water-box configuration of the constant NVT simulation cell.	86
Figure 3.2 OH radical density profiles for a MGP–urea mixture (black line), (b) acetamide–propionamide (blue line), and (c) acetamide–MGP (red line) across the water-box (blue shaded area).....	92
Figure 3.3 Scattering plot of one OH radical (black dots) within the last 7 ns of the simulation. Different trajectories of the radical are highlighted, gas-surface adsorption (green), desorption (red), absorption (purple), and bulk-to-interface transfer (dark blue). The blue shaded area is the water box.....	93
Figure 3.4 Density profiles of (a) MGPL (blue open diamonds) and urea (green filled diamonds), (b) acetamide (purple stars) and propionamide (open green triangles), and (c) acetamide (purple stars) and MGP (blue open diamonds) across the water-bulk (blue shaded area), air-water interface (purple shaded area), and air (unshaded area).	95
Figure 3.5 Atom density profiles for (a) MGP, (b) acetamide, and (c) propionamide across the water-bulk (turquoise blue), air-water interface (purple) interface).	99
Figure 3.6 Snapshot of the air–water interface showing an oriented methyl α -D-glucopyranoside molecules.	99
Figure 3.7 Radial pair distribution functions of the OH radical H atom with the carbonyl oxygen atom for (a) urea, (b) acetamide, and (c) propionamide in the bulk (red lines) and at the air-water interface (blue lines). The profiles are normalized by the area under the curve.....	102
Figure 4.1	136

Figure 4.2 Effect of derivatization parameters; A) reaction temperature B) reaction time and C) BSA reagent volume relative to peak area..... 138

Figure 4.3 The total ion chromatogram (TIC) of an MGP-Urea aerosol sample with xylose as an internal standard. Several peaks were obtained corresponding to the derivatization products of urea (blue), Xylose (black), and MGP (red). 140

Figure 4.4 The total ion chromatogram (TIC) of an MGP-Propionamide aerosol sample with Urea as an internal standard. Several peaks were obtained corresponding to the derivatization products of propionamide (green), Urea (blue), and MGP (red). 141

Figure 4.5 The total ion chromatogram (TIC) of a urea standard sample silylated using BSA and TMCS. A) A full chromatogram of the Derivatized Urea standard; B) Mass spectrum of first peak at retention time 2.760min. C) Mass spectrum of second peak at retention time 3.0324min. 143

Figure 4.6 The total ion chromatogram (TIC) of a xylose standard sample silylated using BSA and TMCS. A) A full chromatogram of the Derivatized xylose standard; B) Mass spectrum of third peak at retention time 5.759min. C) Mass spectrum of fourth peak at retention time 6.348min 143

Figure 4.7 The total ion chromatogram (TIC) of a MGP standard sample silylated using BSA and TMCS. A) A full chromatogram of the Derivatized MGP standard; B) Mass spectrum the peak at retention time 7.997min..... 144

Figure 4.8 The total ion chromatogram (TIC) of a propionamide standard sample silylated using BSA. A) A full chromatogram of the Derivatized propionamide standard; B) Mass spectrum of peak at retention time 1.765min..... 145

Figure 4.9 The total ion chromatogram (TIC) of a urea standard sample silylated using BSA. A) A full chromatogram of the Derivatized urea standard; B) Mass spectrum of first peak at retention time 2.770min. C) Mass spectrum of second peak at retention time 3.049min. 146

Figure 4.10 The total ion chromatogram (TIC) of an MGP standard sample silylated using BSA. A) A full chromatogram of the derivatized MGP standard; B) Mass spectrum of first peak at retention time 6.202min. C) Mass spectrum of second peak at retention time 6.784min. C) Mass spectrum of third peak at retention time 8.029min. 146

Figure 4.11 The total ion chromatogram (TIC) of a glucose standard sample silylated using BSA..... 147

Figure 4.12 Standard calibration curve for MGP(red) and urea(blue) obtained for the MGP-Urea-Xylose method. The coefficients a and b represent the y-intercept and the slope respectively. 151

Figure 4.13 Standard calibration curve for propionamide(green) and MGP(red) obtained for the MGP-Propionamide-Urea method. The coefficients a and b represent the y-intercept and the slope respectively..... 152

Figure 4.14 Standard calibration curve for propionamide(green) and urea(blue) obtained for the Propionamide-Urea-MGP method. The coefficients a and b represent the y-intercept and the slope respectively..... 154

Figure 5.1 Particle size distribution for an aerosol generated from a pure MGP solution before exposure to OH radical (black) and after (red). Left) size distribution expressed as diameter concentration(mm/cm³) and right) size distribution expressed as number concentration (#/cm³). 168

Figure 5.2 Particle size distribution for an aerosol generated from a pure glucose solution before exposure to OH radical (black) and after (red). Left) size distribution expressed as diameter concentration(mm/cm^3) and right) size distribution expressed as number concentration ($\#/ \text{cm}^3$).
..... 169

Figure 5.3 Particle size distribution for an aerosol generated from a pure urea solution before exposure to OH radical (blue) and after (red). Left) size distribution expressed as diameter concentration(mm/cm^3) and right) size distribution expressed as number concentration ($\#/ \text{cm}^3$).
..... 170

Figure 5.4 Particle size distribution for an aerosol generated from a pure propionamide solution before exposure to OH radical (green) and after (red). Left) size distribution expressed as diameter concentration(mm/cm^3) and right) size distribution expressed as number concentration ($\#/ \text{cm}^3$)..... 171

Figure 5.5 Particle size distribution for an aerosol generated from a pure acetamide solution before exposure to OH radical (purple) and after (red). Left) size distribution expressed as diameter concentration(mm/cm^3) and right) size distribution expressed as number concentration ($\#/ \text{cm}^3$)..... 172

Figure 5.6 Particle size distribution for aerosols generated from a pure Urea solution (dark Blue), water (turquoise), acetamide (purple), and propionamide (green) before exposure to OH radical. Left) size distribution expressed as diameter concentration(mm/cm^3) and right) size distribution expressed as number concentration ($\#/ \text{cm}^3$)..... 172

Figure 5.7 a) Particle size distribution for an aerosol generated from a pure MGP-Propionamide solution before exposure to OH radical (purple) and after (red), size distribution expressed as

number concentration ($\#/cm^3$). b) Percentage change in number concentration ($\#/cm^3$) at different OH exposures..... 173

Figure 5.8 Relative signal of unreacted urea (blue dots) and methyl β -D-glucopyranoside (red triangles) in mixed equimolar aqueous aerosols as a function of OH exposure. The solid lines are exponential fits to the experimental data over the whole full range. 175

Figure 5.9 Relative signal of unreacted propionamide (green dots) and methyl β -D-glucopyranoside (red triangles) in mixed equimolar aqueous aerosols as a function of OH exposure. The solid lines are exponential fits to the experimental data over the whole full range. 176

Figure A1 Radial pair distribution functions for A) water O-water O B) MGP-MGP, and C) OH radical O-OH radical O. 192

Figure A2 Scattering plot of 40 OH radicals (red dots) within the last 50 ns of the simulation. The interfacial region is indicated by the purple area, and the turquoise blue area represents the water box..... 192

Figure A3. Density profiles of MGP (blue open diamonds) and glucose (black open circles), (b) acetamide (purple stars) and propionamide (open green triangles), and (c) acetamide (purple)193

Figure A4. Labeling of the carbon atom in methyl β -D-glucopyranoside (MGP) 193

Figure A5. Atom density profiles for (a) urea and (b) glucose across the water-bulk (turquoise blue), air-water interface (purple) interface)..... 194

Figure A6. Radial pair distribution functions of the OH radical H atom with the nitrogen and carbon atoms of (a and d) urea, (b and e) acetamide, and (c and f) propionamide in the bulk (a, b,

c) and at the air-water interface (d, e, f). The profiles are normalized by the area under the curve.

..... 195

List of Tables

Table 3.1 Name, structure, and partition coefficient for the organic solutes used in the MD studies	84
Table 3. 2 Comparison of different water properties determined experimentally and theoretically using the TIP3 water model.	89
Table 3.3 Comparison of Oxygen-Oxygen and Oxygen-Hydrogen pair distribution functional determined experimentally and theoretical using the TIP3P water model.	90
Table 3.4 First and second peak position of water-OH DRFs.	90
Table 3. 5 Simulated surface tension values	91
Table 3.6 Normalized integrated density profiles (% of total area)	96
Table 3.7 Number of molecules around solutes. The number in parenthesis indicates the cutoff distance for determination of the solvation sphere.	100
Table 4.1 Instrument optimum operating conditions for the MGP-Urea-Xylose method.	128
Table 4.2 Instrument optimum operating conditions for the MGP-Propionamide-Urea method and Propionamide-Urea-MGP method.	129
Table 4.3 Peak resolutions for MGP-Urea-Xylose method.	148
Table 4.4 Peak resolutions for MGP-Propionamide-Urea method and Propionamide-Urea-MGP method.....	148
Table 4. 5 Repeatability calculations for MGP-Urea-Xylose method.	149
Table 4.6 Repeatability calculations for MGP-Propionamide-Urea method and Propionamide-Urea-MGP method.....	150
Table 4.7 Inter-day precision calculations for MGP-Urea-Xylose method.	150

Table 4.8 Inter-day precision calculations for for MGP-Propionamide-Urea method and Propionamide-Urea-MGP method.....	151
Table 4.9 linearity and range for MGP-Urea-Xylose method.....	152
Table 4.10 L.O.D MGP-Urea-Xylose method.	152
Table 4. 11 L.O.Q MGP-Urea-Xylose method.	152
Table 4.12 linearity and range for MGP-Propionamide-Urea method.....	153
Table 4.13 L.O.D for MGP-Propionamide-Urea method.	153
Table 4.14 L.O.Q for MGP-Propionamide-Urea method.	153
Table 4.15 linearity and range for Propionamide-Urea-MGP.....	154
Table 4.16 L.O.D for Propionamide-Urea-MGP.	154
Table 4.17 L.O.Q for Propionamide-Urea-MGP.	154
Table 5.1 List of aqueous solutions used to generate along with corresponding density, viscosity, and surface tension data.	166
Table 5.2 Mean diameter of aerosol particles made from different solutions.....	167
Table 5.3 Mean number of aerosol particles made from different solutions.	167
Table 5.4 Reaction and diffusion parameters from bulk solution studies.....	175
Table 5.5 Rate constant and uptake coefficients for the heterogeneous oxidation of organic compounds in aqueous aerosol particles.....	175

1 Introduction

1.1 Chemical species in the atmosphere

The earth's atmosphere is composed of several chemical species, some of which serve as part of the protective envelope of gases surrounding the planet. The major components of the complex mixture we define as the earth's atmosphere are N_2 , O_2 , and Ar.¹ Water, CO_2 , Ne, He, CH_4 , Kr, H_2 , N_2O , CO, O_3 , and Xe exist as minor components of the atmosphere, while NH_3 , NO, SO_2 and H_2S exist as trace components.²⁻⁴ The composition of the atmosphere also extends to include many radicals, inorganic, and organic species. The complex nature of the earth's atmosphere and its ever-evolving composition make the full understanding and mastery of it very elusive. However, the dependence of all life on the atmosphere makes research to understand the earth's atmosphere not only worthy but a necessary endeavor.

1.1.1 Oxidants

The atmosphere's oxidative capacity is a measure of the combined ability of all the oxidants present in the atmosphere to oxidize reactive species in the atmosphere such as emitted pollutants. The oxidants present in the atmosphere include ozone (O_3), hydroxyl radical (OH), Nitrate radical (NO_3), and Hydrogen peroxide.⁵ OH radicals and hydrogen peroxide, are formed via photodissociation from the most abundant oxidant, O_3 .⁶⁻⁸ The nitrate radical (NO_3) has been proven to be the main oxidant in the atmosphere at night to a point where the oxidative capacity of the atmosphere at night can be defined in terms of NO_3 and O_3 only.⁹⁻¹⁵ Lastly, the OH radical has been identified as the detergent of the atmosphere¹⁶ due to its ability to oxidize most of the chemicals in the atmosphere. This capability has led to the OH radical being identified as the most important oxidizing species in the atmosphere.¹⁶⁻²¹ A study of the atmosphere with the intent to understand the fate of chemical species ejected into or formed in the atmosphere can

therefore not ignore the above-mentioned oxidants. The OH radical due to its elevation above the other oxidates demands even more attention.

1.1.2 Organics

From as early as 1950 it had become apparent that organic compounds are present in the earth's atmosphere and by the late 1980s 1000s of individual species had been identified.²² Since then the number has grown to over 10000 species and these include alkanes, alkenes, aromatics, carboxylic acids and their derivatives, saccharides, amine, amides, alcohols and carbonyl compounds.²³⁻³⁸ All these chemical species are believed to be involved in the processes happening in the atmosphere either as gases or as constituents in atmospheric aerosols. The existence of so many species that form a very complex chemical system present obvious challenges to any attempt to understand processes in the atmosphere or in subcomponent of the atmosphere such as organic aerosols. The challenges include difficulties in separation and identification of compounds, and in keeping track of multiple simultaneous reactions. It is therefore necessary to focus on a few species that can act as surrogates, looking at properties that can be extrapolated to other species not studied.

1.2 Atmospheric aerosols

Atmospheric aerosols are technically understood as being a suspension of fine solid or liquid particles (of a complex chemical nature) in the air, with a particle diameter ranging from 1nm to 10 μm .³⁹⁻⁴¹

Atmospheric aerosols are found in the atmosphere either as a result of 1) being directly ejected into the atmosphere or 2) being formed from the interaction of gaseous components present in the atmosphere, (e.g., the reaction of volatile organic compounds (VOCs) with atmospheric oxidants to form secondary organic aerosols (SOAs)). The ejection of aerosols into the

atmosphere occurs during both natural processes, such as volcanic eruptions, and anthropogenic activity, such as the generation of thermal power from coal.⁴²⁻⁴⁵ Likewise, the gaseous components that react to form particles in the atmosphere originate from natural processes and anthropogenic processes.⁴⁶⁻⁴⁸

Cloud formation and earth's solar radiation management have been proven to be influenced by atmospheric aerosols, therefore linking global climate to atmospheric aerosol chemistry.⁴⁹⁻⁵¹

Several health conditions have also been linked directly and indirectly to atmospheric aerosols.⁵²⁻⁵⁴ This suggests that the continuity of high quality living on the planet will depend significantly on understanding the chemistry of atmospheric aerosol.

1.2.1 Formation of atmospheric particles

Atmospheric particles can either be emitted directly into the atmosphere as primary particles, having been formed during other processes such as fossil fuel combustion, or be produced in situ from the reaction of atmospheric oxidants with VOCs. The latter produces organic aerosol referred to as secondary organic aerosols (SOAs).

The formation of SOAs is believed to proceed via one of two mechanisms, either by the condensation of gaseous components on to pre-existing particles or by nucleation of new particles.^{55,56} The formation of SOAs by nucleation begins with different gas phase molecules colliding with one another and coalescing due to the combined effect of intermolecular interaction (chemical bonding, hydrogen bonding, and Coulombic or Van De Waals interactions). This results in small clusters that may then grow if they can become stable against evaporation of the building constituents. Continued interaction with other gaseous components can then lead to additional uptake which subsequently leads to further growth. The small cluster may also coagulate to form larger particles.^{55,57-59} Figure 1.1 Captures a depiction of the

formation of aqueous (AqSOA) and non-aqueous (GasSOA) SOAs as postulated by several researchers over the years.

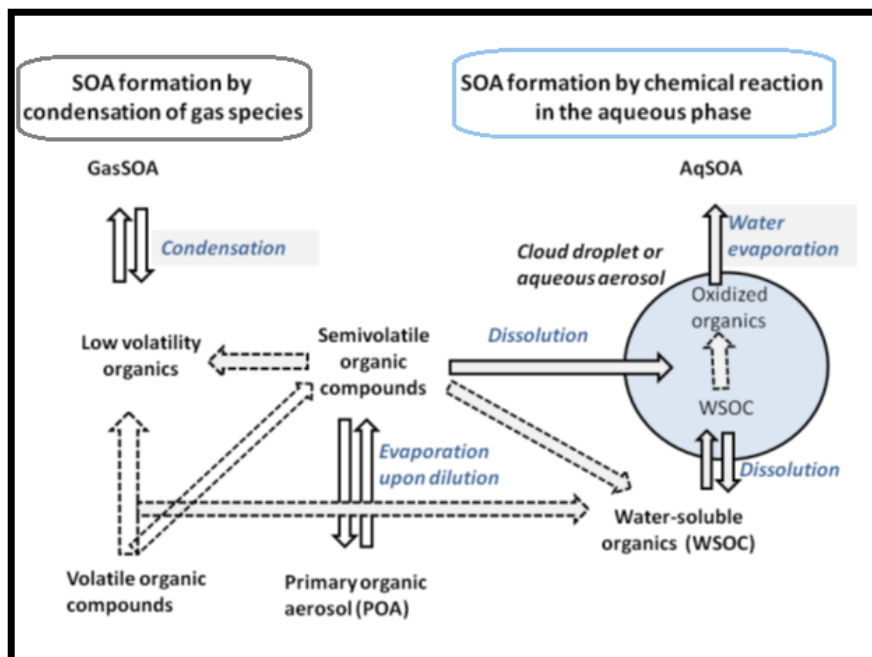


Figure 1.1 Schematic of gasSOA and aqSOA formation pathways in the gas and aqueous phases of the atmosphere. Dashed arrows denote oxidation reactions.^{56,60}

Formation of secondary inorganic aerosols (SIA) is comparatively well understood and similar; with the major difference being the nature of compounds that combine to form SIAs. SIA consist mainly of ammonium nitrate ($\text{NH}_4 \text{NO}_3$), ammonium sulfate ($(\text{NH}_4)_2 \text{SO}_4$) and sodium nitrate (NaNO_3).^{61,62}

1.2.1.1 Amides and Saccharides in atmospheric aerosols

Amides present as a good organic molecules to look at in the atmosphere because of their amphiphiles nature, which allow for the simultaneous studying of hydrophobic and hydrophilic interactions in atmospheric aerosol particles.⁶³ The risk that the products of the radical oxidation of amides pose on human health and the evidence of amide presence in the atmosphere make

amides worthy of investigation.^{38,64-67} Evidence of amides being involved in new particle formation (NPF) in the atmosphere has also started to slowly emerge.^{68,69} NPF as an important mechanism for the formation of aerosols has been credited with the formation of over half the global budget of the atmosphere's cloud condensation nuclei (CCN), which influences cloud processes and energy balance on the planet.⁷⁰⁻⁷² Given the involvement of amides in atmospheric processes, potential health risk and potential involvement in key atmospheric nucleation mechanism, it is vital to study amides in the atmosphere.

Water-soluble organic components (WSOC) have been established as the most important species amongst all organics making up organic aerosols, with the percentage of WSOC going as high as 80% in some organic aerosols.⁷³⁻⁷⁵ Saccharides are one of the top substances making up WSOC with maritime aerosols containing up to 63% by mass saccharides and continental aerosols containing anywhere between 13-26% by mass.⁷⁶⁻⁷⁸ The sources of the three classes of saccharides (anhydro-saccharides, primary saccharides, and saccharide alcohols) present in the atmosphere have been shown to have multiple sources from natural and human activities.⁷⁹⁻⁸⁵ Given the overwhelming presence of saccharides in organic aerosols it is credible to seek an understanding of how saccharides influence atmospheric processes including the chemistry of other organic species present.

1.2.2 Chemical, physical, and optical properties Atmospheric aerosol particle

1.2.2.1 Chemical properties

The chemical constituents of atmospheric aerosol particles can be divided into two distinct groups, inorganic, and organic compounds. From these two divisions, three groups of aerosols are formed: organic aerosols (OAs), inorganic aerosols (IAs), and organic-inorganic aerosols.⁸⁶⁻

⁸⁸ Organic aerosols are the most abundant atmospheric aerosols making approximately 50% of

the total aerosols⁸⁹⁻⁹¹, followed by inorganic aerosols and lastly organic-inorganic aerosols. For all three types of aerosols water-soluble organic components (WSOC)⁷³⁻⁷⁵ and water-soluble inorganic ions (WSII)⁹²⁻⁹⁴ have been established as the most important species amongst all chemical components making up atmospheric aerosols.

1.2.2.2 Physical properties

Atmospheric aerosol particles exist in various phases ranging from solid, semi-solid to liquid particles⁹⁵⁻⁹⁸ or as a combination of phases^{99,100}. Particle are ascribed a phase based on the particle's viscosity.^{97,101} Figure 1.2 shows viscosities and the corresponding phases.

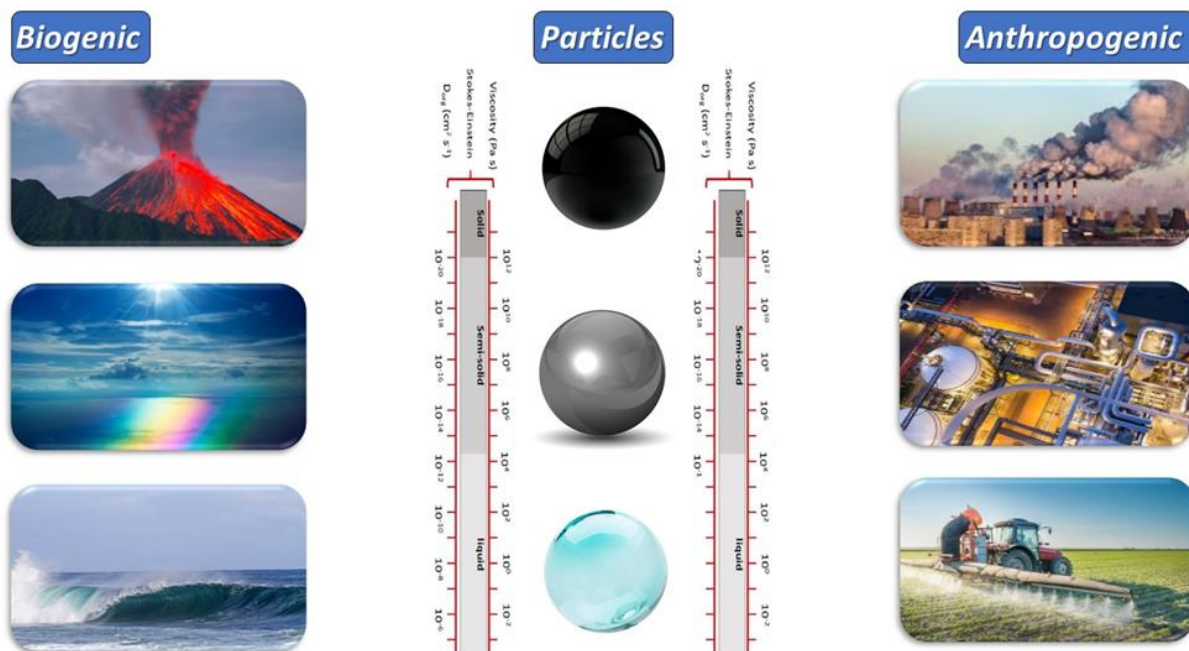


Figure 1.2 Viscosities and the corresponding phases of atmospheric aerosol particles. All the images used are from <http://www.google.com.image>.

The viscosity of atmospheric aerosol particles is dependent on the chemical composition of the particles and the prevailing conditions of the immediate environment. Viscosity being a measure

of resistance to motion is inevitably related to diffusion as a measure of net motion.¹⁰² The two properties are related by the Stokes-Einstein equation:

$$D = \frac{k_B T}{6\pi r \eta} \quad (1.1)$$

Where D is the bulk molecule diffusion, k_B is the Boltzmann constant, T is the temperature(K), r is the radius of the diffusing molecule and η is the dynamic viscosity. Atmospheric aerosol particles are suspended in a gas(air) with other gaseous chemical components, because of this gas-particle equilibrium is reached or attempted. The establishment of the gas-particle equilibrium is governed by three processes: gas-phase diffusion, interfacial transport, and particle phase diffusion. The time taken to establish equilibrium is expressed by the equilibrium partitioning time scale τ_{eq} ^{103,104}:

$$\tau_{eq} = \frac{R_p^2}{\pi^2 D_b} \quad (1.2)$$

Where R_p is the particle radius, D_b is molecular diffusion coefficient of the condensing species in the particle. Liquid atmospheric aerosol particles allow for solute molecules to have large diffusion coefficients thereby reaching equilibrium extremely fast. This leads to the conclusion that the interaction of gas and bulk phase components are not limited by particle bulk-phase diffusion. On the other hand, semi-solid atmospheric aerosol particle components prove to be limited by particle-bulk phase diffusion.

1.2.2.3 Optical properties

Atmospheric aerosol particles possess the ability to scatter, absorb and transmit solar radiation as depicted in Figure 1.3. These optical properties are expressed quantitatively by values such as scattering coefficient, absorption coefficient, extinction coefficient, single scattering albedo and

optical depth. The optical properties of the atmosphere have a huge effect on the atmospheric global radiation and therefor global climate. The optical properties of the aerosols not only affect climate but also affect the environment directly through formation of haze and change of visibility. All the optical properties of atmospheric aerosols are summed up and best described by the complex refractive index (m):

$$m = n + ik \quad (1.3)$$

where n is the real part of the complex refractive index, describing the scattering characteristics of the particle and k is the imaginary part describing the absorbing characteristics.^{105–107} The optical properties of the atmospheric aerosol particles are dependent on the chemical composition, shape, and size of the particles.¹⁰⁸

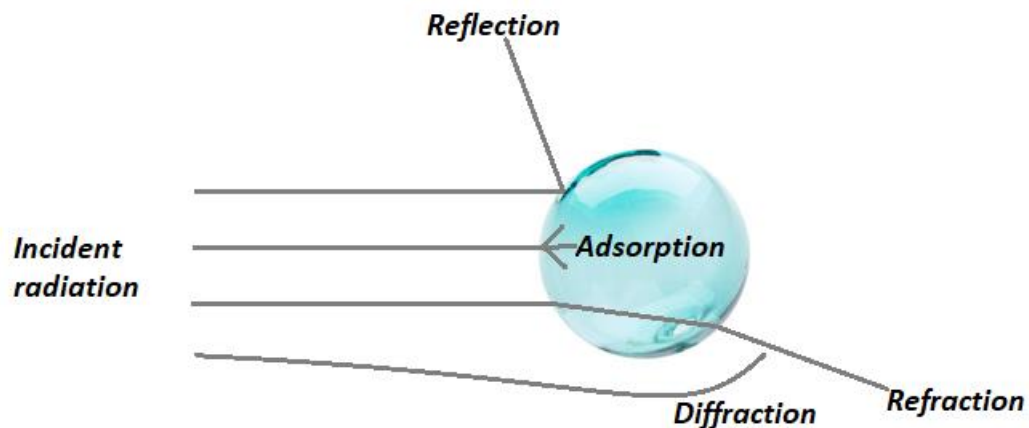


Figure 1.3 Interaction of an atmospheric aerosol particle with solar radiation.

1.3 Chemistry of the interface: Heterogeneous chemistry of atmospheric organic aerosol particles

1.3.1 Liquid surface

The liquid surface is a hive of activity, molecules constantly evaporate from the liquid into the gas phase, while gas phase molecules also adsorb on to the liquid surface and diffuse into to the liquid bulk(Figure 1.4). This implies that a liquid surface is not an infinitesimal sharp boundary in the direction of its normal, but rather it is of a significant thickness. The mass transportation that occurs at the surface also make it clear that the liquid surface is an interface between the bulk of the liquid and the next medium (gas). The thickness of this interface has then to be defined and this can be done by looking at density ρ . If the density normal to a surface is considered, it is observed that within a few molecules the density decreases from the maxima of the liquid bulk to the minima of the gas medium.^{109,110} The interface thickness can also be determined looking at the orientation of the liquid molecules. Interfacial liquid molecules tend to be oriented in a specific way and they lose this orientation the further they moves into the bulk.^{111,112} The most fundamental quantity to the liquid surface is surface tension, which is arguably a property not just of the liquid but of the interaction of the liquid surface and the gas phase components near the surface.¹¹³

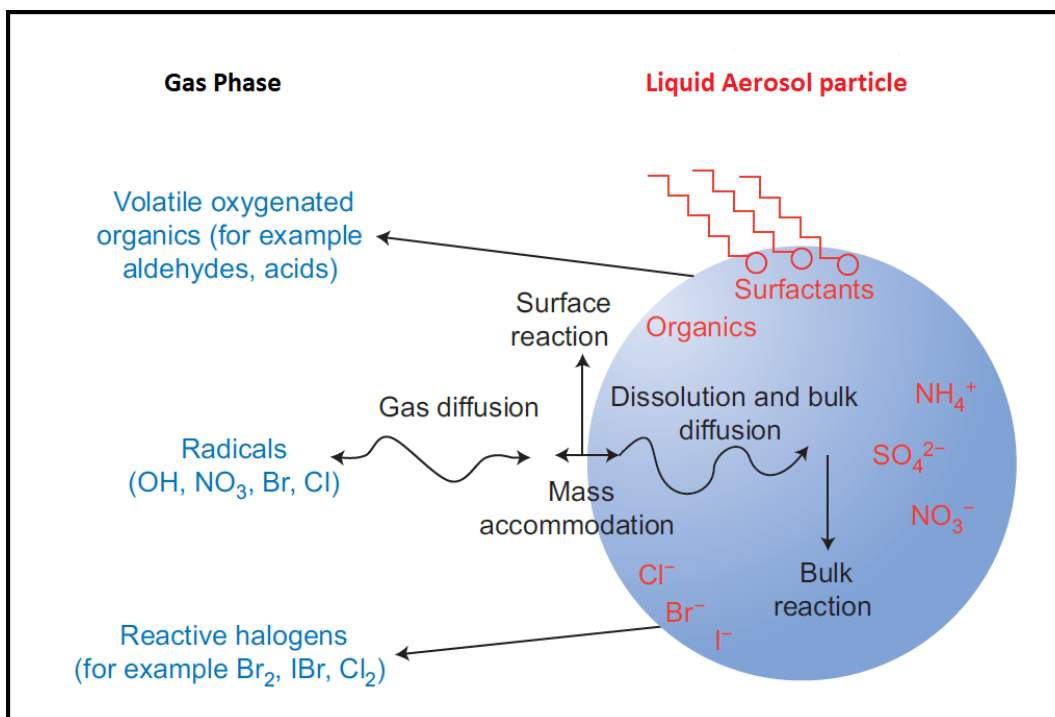


Figure 1.4 Generalized illustration of the processes occurring at the liquid surface and involved in the heterogeneous oxidation of an aqueous organic aerosol particle.

1.3.2 Thermodynamics of gas-liquid interfaces

To be able to apply the thermodynamic formality to the liquid surface, an ideal interface has had to be defined. This ideal dividing plane has been defined as being infinitely thin (assumed to be 0 in most instances). Important excess quantities such as internal excess, can then be defined with respect to the positioning of the ideal Gibbs interface. The internal excess is a measure of the amount of substances that add to or are removed from the interface. Using the ideal Gibbs interface, the Gibbs adsorption isotherm relating surface tension to the amount of solute adsorbed at the interface is expressed as follows:

$$\Gamma = -\frac{1}{RT} \frac{\delta\gamma}{\delta a} \quad (1.4)$$

Where Γ is the internal excess, γ is the surface tension and a is activity. For every gain in solute at the interface the surface tension decreases. When solute avoids the interface surface tension increases.^{114–116}

Partitioning Gibbs free energy can be used to quantitatively describe the partitioning behavior of solutes dissolved in a liquid exposed to a gas. Surface-active (having a higher affinity for the interfacial region) molecule has a negative value of partitioning Gibbs free energy and surface-inactive (having a higher affinity for the liquid bulk region) molecules have a positive partitioning Gibbs free energy. The Partitioning Gibbs free energy is calculated as follows:

$$\Delta_p G^o = -RT \ln K_{p,i} \quad (1.5)$$

Where $K_{p,i}$ is partitioning equilibrium constant, R the ideal gas constant, and T the temperature.¹¹⁷

$$K_{p,i} = \frac{[M_i]_{\Sigma}}{[M_i]_B} \quad (1.6)$$

Where M_i is a molecular species in bulk solution (B) migrating to the gas-liquid(water) interface, $[M_i]_{\Sigma}$ and $[M_i]_B$ are interface and bulk concentrations respectively.

1.3.3 Reaction mechanisms and kinetics of heterogeneous oxidation of atmospheric particles

The overall kinetics of the heterogeneous oxidation of atmospheric aerosols encompass the following separate physicochemical processes^{118–121}:

1. Gas-phase diffusion: gas-phase species diffuses from the gas phase to the surface of the atmospheric particles.

2. Mass accommodation: gas-phase species strikes a given particle surface via collision, stick (adsorption) to the surface or bounce(desorption) back to the gas phase.
3. Surface chemical reaction: the gas-phase species react with surface-bounded particle molecules.
4. Dissolution and bulk diffusion: unreacted gas-phase species dissolve in the bulk phase which depends on their solubility, the dissolved gas phase species then diffuse into the bulk phase. The products of surface reaction desorb into the gas phase or dissolve into the bulk phase.
5. Bulk chemical reaction: the gas-phase species and surface reaction products react with bulk-phase species.

While research is still on going to understand all the processes listed above, the reactions at the liquid surface are the least understood. Surface reactivity for radicals, such as OH radical, is supported by calculation of the reacto-diffusive length, that is, the extent to which a reactant will penetrate the bulk phase before reaction.¹²²

1.3.4 The reactive uptake coefficient (γ)

The reactive uptake coefficient (γ) is a quantity that expresses the probability that a reaction will occur after a gas-surface collision. This parameter has been used in models to determine the importance of given heterogenous reaction in the atmosphere. Reactive uptake coefficient (γ) values that are ≥ 0.1 signify that a reaction is efficient, while values ≤ 0.1 indicate the opposite. Numerous studies have been done to determine the uptake of radicals, the studies have shown that OH and Cl radical reactions are very efficient with $\gamma \geq 0.11$.¹²³⁻¹²⁶ OH uptake coefficients cannot exceed 1, however, reactive uptake coefficient for the reaction of OH radicals and organics have been reported to go higher than 1.0. Reactive uptake coefficient values ≥ 1 reflect not only loss of the gas-phase radicals to the particle surface, but also hint at secondary

chemistry leading to loss of reactants from reaction with particle-phase intermediates. The traditional approach of measuring gas-phase radical loss cannot be used in these kind of studies and an approach of measuring decay of particle-phase species and monitoring them as a function of radical exposure time is used instead.^{127–130} As an indicator of the overall reaction efficient, reactive uptake coefficient (γ) is related to all the physicochemical processes involved in the heterogenous oxidation of atmospheric aerosols. This is presented in the following equation:

$$\frac{1}{\gamma} = \frac{1}{\Gamma_g} + \frac{1}{\alpha} + \frac{1}{\Gamma_{rxn}} + \frac{1}{\Gamma_{sol}} \quad (1.7)$$

Where Γ_g is the gas-phase diffusion, Γ_α is the mass accommodation, Γ_{rxn} accounts for the reaction term and Γ_{sol} accounts for solubility (dissolution).¹³¹ The reactive uptake coefficient (γ) is calculated from the following formular:

$$\gamma = \frac{2k_{org}d_p\rho_0N_A}{3cM} \quad (1.8)$$

were k_{org} is the observed apparent decay rate constant of the particle species (the second order of heterogeneous reaction rate coefficient). ρ_0 , M , and N_A are the density of particle, the molecular weight of particle species and the Avogadro's number. d_p is the mean surface-weighted particle diameter and c is the mean speed of gas-phase reactant.^{132–134}

The radical uptake onto the surface can occur in one of two ways, either by following the Eley–Rideal (ER) (one-step reaction) or Langmuir–Hinshelwood (LH) (two-step reaction) kinetic mechanisms.^{135,136} The ER mechanism suggests that the radical does not adsorb onto the surface of the particle before reacting with the Bulk-phase species, rather the radical collides directly with the reactive bulk phase species and react. The LH mechanism suggests that the gas-phase

radical first adsorbs on to the surface and then reacts with the bulk-phase reactant.^{137,138} Figure 1.5 show a depiction of the two mechanisms

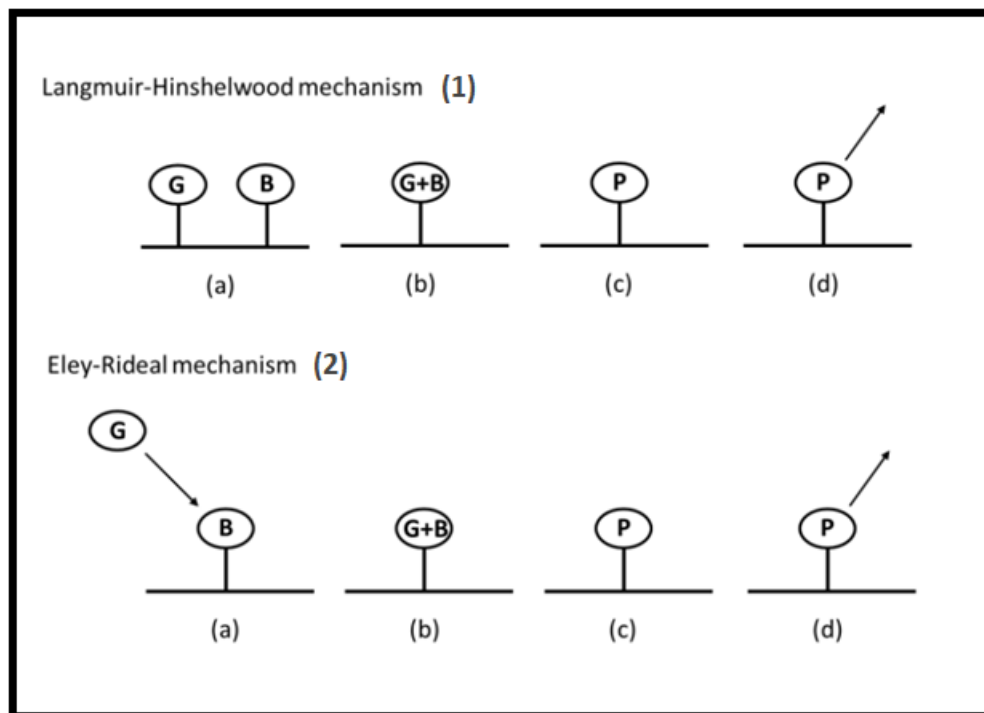


Figure 1.5 (1) Diagram of the Langmuir-Hinshelwood (L-H) reaction G (gas-phase reactants) + B (bulk molecule) \rightarrow P (products). The G need to adsorb on the surface (a) before reacting to form P (b), which may remain on the surface (c) or desorb (d). (2) Diagram of the Eley-Rideal (E-R) reaction, the G does not adsorb onto the surface prior to reaction (a, b). The P may remain on the surface (c) or desorb (d).^{137,138}

Radical uptake could occur via one of the mechanism or could involve both. Experiment have been conducted to try and establish with mechanism is prevailing for OH radical oxidations.¹³⁶ In some studies, the Inelastic scattering of OH radicals from squalane surfaces has been observed, and this is suggestive of OH radical being adsorbed on the surface for a considerable period.¹³⁹ Several other experiments have also produced evidence of OH radical adsorption and therefor

suggesting LH mechanism.¹⁴⁰ Despite the above mentions results no unambiguous confirmation of LH or ER mechanism through kinetic observations has not been demonstrated.

1.3.5 Chemistry reactions in the bulk-phase and at the air-water(liquid) interface

The comparison of the kinetic for the radical uptake onto the surface with analogous gas-phase reaction and bulk-phase reactions suggest that the presence of an interface greatly alters the reaction rates.¹⁴¹ Enhancement of slow gas-phase reactions at the interface has been proven for radicals such NO₃ and Br. OH radical reaction have been shown to be able to proceed near the collision limit once at the interface.¹²⁶ Several explanation for this enhancement have been proposed such as longer residence times of radicals on interface because of following the LH reaction mechanism, low activation energies for surface reaction, more favorable reaction energetics through alternative reaction pathways and micro-confinement effects.^{142,143} This enhancement also makes it clear that while well understood analogous gas-phase and bulk-phase mechanisms make good initial assumptions for the mechanisms at the interface reactions, they are inadequate to explain surface oxidation chemistry.

Several other studies have also highlighted other significant changes other than rate that have been caused by reactant species interacting at the interface. Prisle et al.¹⁴⁴ reported increased acid production at the interface compared to the bulk due to a different acid-base chemistry occurring at the interface. Kumar et al¹⁴⁵ study highlights an even more drastic difference between bulk and interface as it suggests a different reaction product from the same reactants. Suggesting hydroxyethyl hydroperoxide as the product for the surficial reaction, and nitroxyethyl hydroperoxide for the bulk reaction. Kusaka et al¹⁴⁶ also reports the extreme change between the bulk and the interface chemistry as they report the photochemical reaction of phenol to be 10000 times faster at the interface.

The partitioning properties of the bulk-phase reactants are key factor to the reactions that occur both at the interface and in the bulk. Some species in the bulk-phase are surface-active molecules, this means having a higher affinity for the interfacial region (higher number density at the interface than in the bulk). Other species will prove to be surface-inactive molecules, this means having a higher affinity for the bulk region (higher number density in the bulk than at the interface).¹⁴⁷ The overall reaction rate of the heterogeneous oxidation of aqueous(liquid) atmospheric aerosol particles is therefore a summation of the surface rate and the bulk rate. The rate has to also take into account the thickness of the interface. The overall pseudo-first order reaction rate is given by the following equation:

$$k_1 = k_{bulk} + \left(\frac{k_{1,\sigma}}{\delta}\right) \quad (1.9)$$

were k_{bulk} and $k_{1,\sigma}$ are respectively the homogenous bulk (aqueous)-phase and heterogeneous surface reaction rate constants, and δ is surface water film thickness. Experimental studies have shown that as δ decreases, the contribution of $k_{1,\sigma}$ to the overall reaction rate k_1 increases.¹⁴⁷⁻

¹⁴⁹Figure 1.6 shows the kinetics framework for gas-phase oxidants reacting with reactive species in an aqueous(liquid) particle.

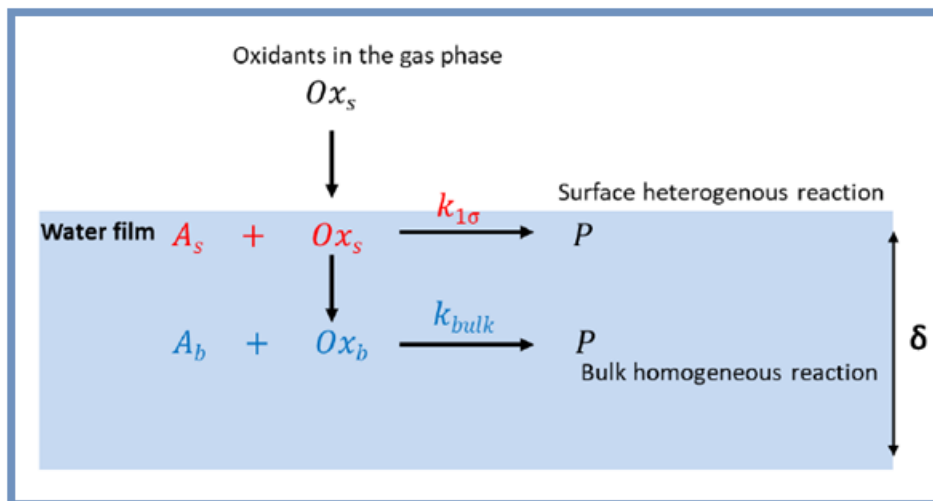


Figure 1.6 A schematic of two reaction channels (surface heterogeneous reaction and bulk homogeneous reaction) for gas-phase oxidants reacting with organic reactive reactants in the aqueous droplet. A_s and A_b are the reactive organic species at the surface of aqueous droplet and in the bulk of droplet. Ox_s and Ox_b are the gas-phase oxidants at the surface of aqueous droplet and in the bulk of droplet. P is the product.¹⁴⁸

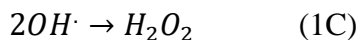
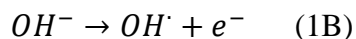
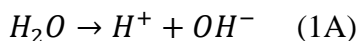
Experimental studies suggest that the reaction mechanism in the bulk of aqueous(liquid) atmospheric aerosol remains similar to regular reaction occurring in bulk solvent e.g. water.¹⁴⁵

1.4 Drastic changes to chemistry at the interface of spherical particles

As has been already pointed out in previous sections there is growing evidence that the chemical reactions at the interface of liquid particles and microdroplets^{150,151} are by several orders of magnitude enhanced compared to their bulk counterparts.

However, even more drastic changes have been attributed to the liquid particle interface, such as the spontaneous formation of H_2O_2 ^{152–154}, the occurrences of phosphorylation reaction in microdroplets¹⁵⁵, and a different electric field.¹⁵⁶ The Zare and Mishra laboratories have detected H_2O_2 being produced at the interface of pure water microdroplets.^{157,158} As the H_2O_2 has not been detected in bulk water or at the interface of non-spherical large volumes of water, this

phenomenon has been attributed solely to the liquid particle interface. A mechanism for the formation of the H_2O_2 has been proposed:



However, this mechanism can only be plausible if the interfacial environment on liquid droplets can create a means to overcome the highly unfavorable ionization step 1B. Investigations to determine if the interfacial environment poses the ability to alter the ionization energy demands of step B were conducted using ab initio calculations and reactive MD simulations. Some of the key findings from the investigations were that ionization energy of OH^- increases with increasing water molecules in the solvation shell due to cluster induced stability, and that the water molecules continue to add stability beyond the first solvation shell. Leading to the conclusion that the interface OH^- has a different ionization compared to bulk water OH^- and therefore the interfacial environment makes OH^- more susceptible to oxidation. The electric fields specific only to the air-water interface of aqueous droplets also make the limiting energetic step(1B) accessible.

Phosphorylation which is known to be thermodynamically unfavorable in solution has been shown to have a $-\Delta G$ of reaction in microdroplets. Inho Nam and Co found that sugar phosphorylation in microdroplets had a reduced entropic cost compared to bulk solution.¹⁵⁵ The entropic change for the chemical reaction has been attributed to molecular orientation and reactants alignment at the air-water interface of aqueous droplets and a strong electric field in the interfacial region.¹⁵⁹⁻¹⁶²

The above mentioned recent observations that have been tied to the liquid particle and particularly the interface of the particle, show that little is understood about the air-liquid interface. The vast difference between interfacial chemistry and bulk chemistry is still yet to be fully explored. Understanding of interfacial chemistry in liquid particles presents us with new reactive possibilities previous not accessible.

1.5 MD simulation of the interface: A computational look at the Gas- liquid interface

Computer simulations of chemical systems can basically be divided into two major divisions. Classical mechanical simulations and quantum mechanical (QM) simulations. Quantum mechanical (QM) simulations present the best approximation to real life chemical systems and therefore give the highest accuracy.¹⁶³ However, QM is limited to very small systems due to it being computationally expensive and having limited theory. Because of this, the classical mechanics approach is the go-to for most simulations of relatively large chemical systems.^{164,165} A method known as QM/MM (quantum mechanics/molecular mechanics) method that harnesses the advantages of both classical mechanical simulations and quantum mechanical (QM) simulations has also been developed and continues to gain popularity.¹⁶⁶

In classical mechanical simulations Newton's second law is numerically integrated to give time trajectories for a system of interacting atoms, ions and/or molecules. The position and velocity of an atom in the system can be determined from:

$$\vec{F}_i = m_i \vec{a}_i = -\frac{\partial U}{\partial r_i} \quad (1.10)$$

Where \vec{F}_i is the force on a particle i with a mass m_i and an acceleration \vec{a}_i , U is the interatomic potential energy and r_i represents the cartesian set of coordinates of a particle i .¹⁶⁷ An ideal

model would be one that is able to fully describe a chemical system including properties such as the dynamics of electrons and nuclei of the atoms in the system. However, due to the extremely different time scales between nuclei and electron motions, classical simulations are unable to capture both these dynamic. To address this limitation, classical simulations invoke the Born-Oppenheimer approximation.¹⁶⁸⁻¹⁷⁰ The approximation allows for the examination of the dynamical evolution of the nuclei without considering explicitly the contribution from the electrons. This then prevents the use of classical simulation to model effects such as bond formation and bond breaking amongst other quantum mechanical effects. The time step used in the numerical integration (femtoseconds) also make the use of classical simulations to model processes occurring at much slower time scales (seconds) very computationally expensive and slow.

1.5.1 Classical Computational methodologies

Several different Classical simulations methods exist. These are Monte Carlo (MC) simulations, Langevin dynamics (LD) simulations, Brownian dynamics (BD) simulations, and molecular dynamics (MD) simulations.

Monte Carlo Simulation, also known as the Monte Carlo Method, is a mathematical technique, which uses randomly generated probabilities to decide if the movement of a given molecule is permissible. MC simulation server to generate an ensemble of representative configurations under specific thermodynamics conditions for a chemical system. From these configurations thermodynamic quantities such as free energy may be determine. MC simulations are incapable of giving information about time depended changes but play a critical role in other simulation methods that are capable of time evolution studies.^{171,172}

Langevin dynamics simulations like MC simulations attempt to describe the dynamics of molecular systems utilizing Langevin equations.^{173,174} Brownian dynamics (BD) simulations are simplified versions of Langevin dynamics and are sometimes referred to as overdamped Langevin dynamics.¹⁷⁵ Both LD and BD simulations use a simplified description of the chemical system where solvent molecules are not treated individually.

An **MD simulation** may be defined as a computer simulation technique that allows the prediction of time evolution of an interacting system of atoms or molecules, by generating atomic trajectories of the system using numerical integration of Newton's equation of motion for a specific interatomic potential defined by an initial condition and boundary condition. Figure 1.7 shows the MD simulation procedure. Governed by classic mechanics, the Hamiltonian of a system model using MD simulation is given by the following equation:

$$H(p, r) = \sum_i \frac{p_i^2}{2m_i} + U \quad (1.11)$$

Where H is the total energy (Hamiltonian) of the system, P is the momentum, r is the position, m is the mass, and U is the potential energy. From this Hamiltonian the equations of motion can then be derived. The classical equations of motion utilized are as follows:

$$\dot{r}_i = \frac{\partial H}{\partial p_i} = \frac{p_i}{m_i} \quad (1.12)$$

$$\dot{p}_i = -\frac{\partial H}{\partial r_i} = -\nabla_r U \quad (1.13)$$

Where $-\nabla_r U$ is the force on the atoms in the system. From the above equations it becomes possible to calculate the position of atoms in the system at any time $t + \Delta t$ and write a trajectory.^{176,177}

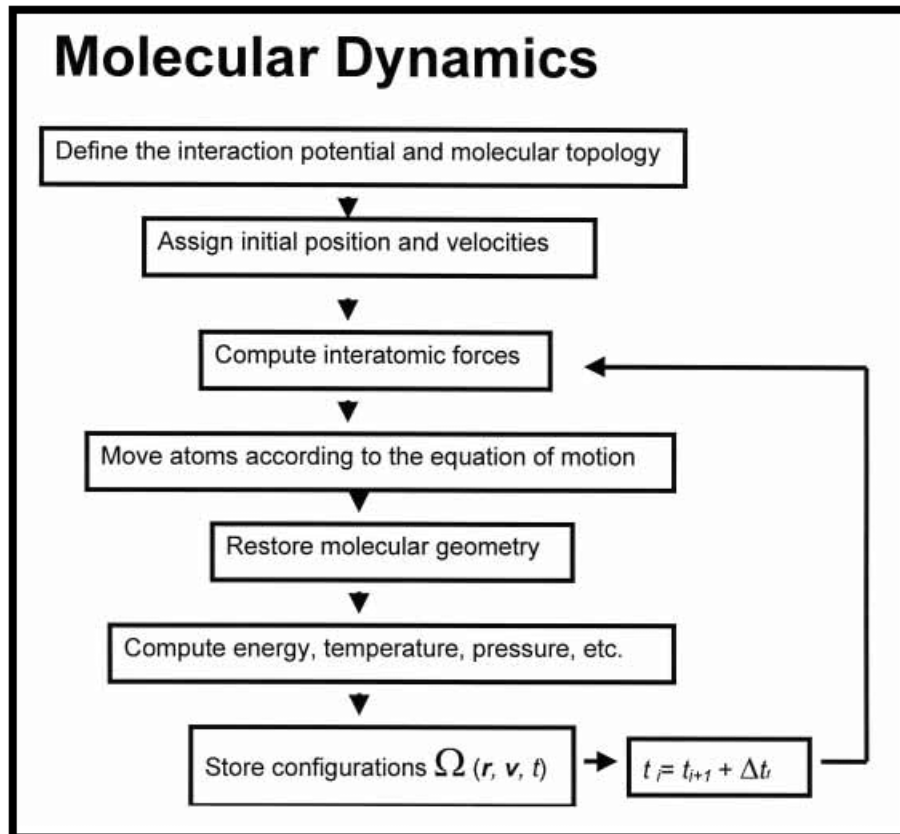


Figure 1.7 The Molecular Dynamics simulation procedure.

1.5.2 Properties of the gas-liquid interface

Due to its ability to probe areas that remain inaccessible to available experimental techniques MD simulations have found extensive use in heterogenous chemistry and surface chemistry.^{178,179} Over the years a lot of insight on bulk-phase and interface interactions has been obtained using MD simulations. Studies have look at structure and dynamics at the interface between water and air and have reported on specific properties such as surface tension, water molecule orientation and proton hopping.¹⁸⁰⁻¹⁸² The partitioning of solutes between the bulk-phase and the interface has also been investigated using MD simulations looking at both organic and inorganic solutes.¹⁸³⁻¹⁸⁵ MD simulations have also been very instrumental in the study of OH

radical as an oxidant, with key results such as OH radical interface preference, solvation and its mobility mechanism in water being reported.^{186,187}

1.6 The aims and objectives of this thesis

Atmospheric aerosols are at the center stage of global climate, contributing directly to global climate by absorbing or scattering incoming solar radiation, and indirectly via cloud condensation effects. Plenty of research hours have gone into understanding atmospheric aerosols, however, a lot about atmospheric aerosol remains unknown^{188–191}.

The consensus in Heterogeneous chemistry studies is that the heterogeneous chemistry of aerosol particles is controlled by chemical and physical processes occurring in the particle bulk and at the gas-condensed-phase interfaces.^{190,192–194} The relative importance of each of these properties changes depending on the chemical composition and physical properties of the aerosol particles, and the ambient condition.^{97,144,195,196} This is best demonstrated by the influence of transport phenomena such as mass transfer on the chemical evolution of an aerosol particle. Evidence shows that mass transfer influence decreases with decreasing particle viscosity and increasing rates of diffusion.^{196–199}

Aerosol particles have been treated and modeled as single-compartment reactors.¹⁹⁶ However, evidence continues to grow that suggests that the aerosol particle is a complex multi-compartment reactor, with each compartment having different conditions capable of producing unique chemistry. One of these compartments that has gained much notoriety is the gas-condensed-phase interface. Many researchers suggest that the dominant chemical processes in the heterogeneous chemistry of aerosol particles occur in this small 1 to 2nm compartment.^{144,145,192,194–203} This idea holds so much sway that key reactivity accessing

coefficients are calculated on the premise that reactive interactions occur mainly on the interface.²⁰³ The reactive uptake coefficient can be used to compare the reactivity of a solute in particles of different sizes and densities. The importance of the interface has led to the conclusion that the chemical aging of aerosol particles is dependent on the ability of the chemical species in the aerosol to migrate to and populate the interfacial region.

This thesis attempts to contribute to the existing pool of knowledge on the following key areas as they relate to the heterogeneous oxidation of aqueous organic aerosols:

- The effect of intramolecular interaction between coexisting solutes, the solvent, and the gas-phase reactant, on chemical and physical evolution of aqueous aerosols.
- The effect of chemical composition change on the reactivity of reactive species in the aqueous aerosols.
- The importance of interfacial interactions and reaction on the heterogeneous oxidation of aqueous aerosols.

In chapter three MD simulations are used to develop and probe close enough approximations of atmospheric multicomponent aqueous particles. The air-water interface and particle bulk properties were closely examined, giving quantitative information about the dimensions and composition of each compartment. The influence of molecular structure and solvation structure was also investigated.

In the fourth chapter, two similar analytical methods for the quantification and identification of amide and monosaccharides in aqueous aerosols were developed and validated. The methods were developed to meet the specific needs of the studies done in chapter 5. However, it was designed to be easily adopted for other similar compounds relevant to atmospheric chemistry.

In chapter 5 the effect of chemical composition on the reactivity of solutes in aqueous aerosol particles was investigated. The kinetics were measured by monitoring the loss of the particle-phase reactants using an offline GC-MS. In the fifth chapter the importance of surface reaction and partitioning was also investigated.

Reference

1. Singh HB. Composition Chemistry and_Climate_of_the. *Van Nostrand Reinhold*.
Published online 1995:32.
2. Jones G. The atmosphere and the environment. *People Environ*. Published online
2021:95-125. doi:10.4324/9781315838366-15
3. Rusch DW, Clancy RT. Minor constituents in the upper stratosphere and mesosphere. *Rev
Geophys*. 1987;25(3):479-486. doi:10.1029/RG025i003p00479
4. Johansson S, Höpfner M, Kirner O, et al. Pollution trace gas distributions and their
transport in the Asian monsoon upper troposphere and lowermost stratosphere during the
StratoClim campaign 2017. *Atmos Chem Phys*. 2020;20(23):14695-14715.
doi:10.5194/acp-20-14695-2020
5. Thompson AM. The Oxidizing Capacity of the Earth's Atmosphere: Probable Past and
Future Changes. *Science (80-)*. 1992;256(5060):1157-1165.
doi:10.1126/science.256.5060.1157
6. Stephens ER. Chemistry of atmospheric oxidants. *J Air Pollut Control Assoc*.
1969;19(3):181-185. doi:10.1080/00022470.1969.10466475
7. Ren X, Van Duin D, Cazorla M, et al. Atmospheric oxidation chemistry and ozone
production: Results from SHARP 2009 in Houston, Texas. *J Geophys Res Atmos*.
2013;118(11):5770-5780. doi:10.1002/jgrd.50342
8. Jacob DJ. The Oxidizing Power Of The Atmosphere. In: ; 2000.
9. Heintz F, Platt U, Flentje H, Dubois R. Long-term observation of nitrate radicals at the

- Tor Station, Kap Arkona (Rügen). *J Geophys Res Atmos.* 1996;101(D17):22891-22910.
doi:<https://doi.org/10.1029/96JD01549>
10. Platt U, Perner D, Schröder J, Kessler C, Toennissen A. The diurnal variation of NO₃. *J Geophys Res Ocean.* 1981;86(C12):11965-11970.
doi:<https://doi.org/10.1029/JC086iC12p11965>
 11. Finlayson-Pitts BJ, Pitts JN. CHAPTER 14 - Global Tropospheric Chemistry and Climate Change. In: Finlayson-Pitts BJ, Pitts JN, eds. *Chemistry of the Upper and Lower Atmosphere*. Academic Press; 2000:762-843. doi:<https://doi.org/10.1016/B978-012257060-5/50016-2>
 12. Seinfeld JH, Seinfeld PDCJH, Pandis SN. *Atmospheric Chemistry and Physics: From Air Pollution to Climate Change*. Wiley; 2006.
<https://books.google.com/books?id=tZEpAQAAMAAJ>
 13. Lee Ng N, Brown SS, Archibald AT, et al. Nitrate radicals and biogenic volatile organic compounds: Oxidation, mechanisms, and organic aerosol. *Atmos Chem Phys.* 2017;17(3):2103-2162. doi:10.5194/acp-17-2103-2017
 14. Foulds A, Khan MAH, Bannan TJ, Percival CJ, Lowenberg MH, Shallcross DE. Abundance of no₃ derived organo-nitrates and their importance in the atmosphere. *Atmosphere (Basel)*. 2021;12(11). doi:10.3390/atmos12111381
 15. Khan MAH, Cooke MC, Utembe SR, et al. Global modeling of the nitrate radical (NO₃) for present and pre-industrial scenarios. *Atmos Res.* 2015;164-165(3):347-357.
doi:10.1016/j.atmosres.2015.06.006

16. Gligorovski S, Strekowski R, Barbati S, Vione D. Environmental Implications of Hydroxyl Radicals ($\bullet\text{OH}$). *Chem Rev.* 2015;115(24):13051-13092. doi:10.1021/cr500310b
17. Alvarez EG, Amedro D, Afif C, et al. Unexpectedly high indoor hydroxyl radical concentrations associated with nitrous acid. *Proc Natl Acad Sci U S A.* 2013;110(33):13294-13299. doi:10.1073/pnas.1308310110
18. Riedel K, Lassey K. Detergent of the atmosphere. *Water Atmos.* 2008;16(1):22-23. <https://www.niwa.co.nz/sites/niwa.co.nz/files/import/attachments/detergent.pdf>
19. Stone D, Whalley LK, Heard DE. Tropospheric OH and HO₂ radicals: Field measurements and model comparisons. *Chem Soc Rev.* 2012;41(19):6348-6404. doi:10.1039/c2cs35140d
20. Bianco A, Passananti M, Brigante M, Mailhot G. Photochemistry of the cloud aqueous phase: A review. *Molecules.* 2020;25(2):1-23. doi:10.3390/molecules25020423
21. Li M, Karu E, Brenninkmeijer C, Fischer H, Lelieveld J, Williams J. Tropospheric OH and stratospheric OH and Cl concentrations determined from CH₄, CH₃Cl, and SF₆ measurements. *npj Clim Atmos Sci.* 2018;1(1):1-7. doi:10.1038/s41612-018-0041-9
22. Goldstein A, Galbally I. Known and Unexplored Organic Constituents in the Earth's Atmosphere. *Environ Sci Technol.* 2007;41. doi:10.1021/es072476p
23. Chebbi A, Carlier P. Carboxylic acids in the troposphere, occurrence, sources, and sinks: A review. *Atmos Environ.* 1996;30(24):4233-4249. doi:10.1016/1352-2310(96)00102-1
24. Väitilingom M, Charbouillot T, Deguillaume L, et al. Atmospheric chemistry of carboxylic acids: Microbial implication versus photochemistry. *Atmos Chem Phys.*

- 2011;11(16):8721-8733. doi:10.5194/acp-11-8721-2011
25. Li J, Li K, Li H, et al. Long-chain alkanes in the atmosphere: A review. *J Environ Sci.* 2022;114:37-52. doi:<https://doi.org/10.1016/j.jes.2021.07.021>
 26. Carter WPL, Atkinson R. Atmospheric chemistry of alkanes. *J Atmos Chem.* 1985;3(3):377-405. doi:10.1007/BF00122525
 27. Gao Y, Li M, Wan X, et al. Important contributions of alkenes and aromatics to VOCs emissions, chemistry and secondary pollutants formation at an industrial site of central eastern China. *Atmos Environ.* 2021;244:117927. doi:<https://doi.org/10.1016/j.atmosenv.2020.117927>
 28. Rhew RC, Deventer MJ, Turnipseed AA, et al. Ethene, propene, butene and isoprene emissions from a ponderosa pine forest measured by relaxed eddy accumulation. *Atmos Chem Phys.* 2017;17(21):13417-13438. doi:10.5194/acp-17-13417-2017
 29. Hites RA. Polycyclic Aromatic Hydrocarbons in the Atmosphere near the Great Lakes: Why Do Their Concentrations Vary? *Environ Sci Technol.* 2021;55(14):9444-9449. doi:10.1021/acs.est.0c06905
 30. Taraborrelli D, Cabrera-Perez D, Bacer S, et al. Influence of aromatics on tropospheric gas-phase composition. *Atmos Chem Phys.* 2021;21(4):2615-2636. doi:10.5194/acp-21-2615-2021
 31. Chen Y, Guo H, Nah T, et al. Low-Molecular-Weight Carboxylic Acids in the Southeastern U.S.: Formation, Partitioning, and Implications for Organic Aerosol Aging. *Environ Sci Technol.* 2021;55(10):6688-6699. doi:10.1021/acs.est.1c01413

32. Li F, Wang H, Wang X, et al. Pollution characteristics of atmospheric carbonyls in urban Linfen in winter. *Atmosphere (Basel)*. 2020;11(7):1-14. doi:10.3390/atmos11070685
33. Grosjean D. Atmospheric chemistry of alcohols. *J Braz Chem Soc*. 1997;8(5):433-442. doi:10.1590/S0103-50531997000500002
34. Colmenar I, Martin P, Cabañas B, Salgado S, Tapia A, Aranda I. Atmospheric fate of a series of saturated alcohols: Kinetic and mechanistic study. *Atmos Chem Phys*. 2020;20(2):699-720. doi:10.5194/acp-20-699-2020
35. Warneck P, ed. Chapter 10 Sulfur Compounds in the Atmosphere. In: *Chemistry of the Natural Atmosphere*. Vol 41. International Geophysics. Academic Press; 1988:484-542. doi:https://doi.org/10.1016/S0074-6142(08)60637-3
36. Marynowski L, Simoneit BRT. Saccharides in atmospheric particulate and sedimentary organic matter: Status overview and future perspectives. *Chemosphere*. 2022;288(P1):132376. doi:10.1016/j.chemosphere.2021.132376
37. Mckee GA. the Nature, Origin and Preservation of Amide Organic Nitrogen in Organic Matter. *PhD thesis*. 2011;(July 2006). doi:10.25777/ng41-5t14
38. Bunkan AJC, Mikoviny T, Nielsen CJ, Wisthaler A, Zhu L. Experimental and Theoretical Study of the OH-Initiated Photo-oxidation of Formamide. *J Phys Chem A*. 2016;120(8):1222-1230. doi:10.1021/acs.jpca.6b00032
39. Armand P, Tâche J. 3D modelling and simulation of the dispersion of droplets and drops carrying the SARS - CoV - 2 virus in a railway transport coach. *Sci Rep*. 2022;(0123456789):1-22. doi:10.1038/s41598-022-08067-6

40. Hinds WC. Aerosol Technology.
41. Farmer DK, Boedicker EK, DeBolt HM. Dry Deposition of Atmospheric Aerosols: Approaches, Observations, and Mechanisms. *Annu Rev Phys Chem.* 2021;72(1):375-397. doi:10.1146/annurev-physchem-090519-034936
42. Pitari G, Genova G Di, Mancini E, Visioni D, Gandolfi I, Cionni I. Stratospheric Aerosols from Major Volcanic Eruptions : A Composition-Climate Model Study of the Aerosol Cloud Dispersal and e -folding Time. Published online 2016. doi:10.3390/atmos7060075
43. Kirk-Davidoff D. Chapter 3.4 - The Greenhouse Effect, Aerosols, and Climate Change. In: Török B, Dransfield TBTGC, eds. Elsevier; 2018:211-234. doi:https://doi.org/10.1016/B978-0-12-809270-5.00009-1
44. Mushtaq Z, Sharma M, Bangotra P, Sagar A, Sneha G. Atmospheric Aerosols : Some Highlights and Highlighters , Past to Recent Years Aerosol Radiative forcing. *Aerosol Sci Eng.* 2022;6(2):135-145. doi:10.1007/s41810-022-00133-w
45. Bandyopadhyay J, Mohammad L, Mondal I, Kanti K. Identification and characterization the sources of aerosols over Jharkhand state and surrounding areas , India using AHP model over Jharkhand state and surrounding areas , India using. *Geomatics, Nat Hazards Risk.* 2021;12(1):2194-2224. doi:10.1080/19475705.2021.1949395
46. Montero-montoya R, López-vargas R, Arellano-aguilar O. Volatile Organic Compounds in Air : Sources , Distribution , Exposure and Associated Illnesses in Children. 2018;84(2):225-238.
47. He Z, Wang X, Ling Z, et al. Contributions of different anthropogenic volatile organic

- compound sources to ozone formation at a receptor site in the Pearl River Delta region and its policy implications. 2019;(x):8801-8816.
48. Gu S, Guenther A, Faiola C. Effects of Anthropogenic and Biogenic Volatile Organic Compounds on Los Angeles Air Quality. Published online 2021.
doi:10.1021/acs.est.1c01481
 49. France OB, France CG, Germany CH, Uk AJ. Clouds and Aerosols.
 50. York N, States U, Gebremariam S, Li S, Weldegaber M. Observed Correlation between Aerosol and Cloud Base Height for Low Clouds at Baltimore and. Published online 2018.
doi:10.3390/atmos9040143
 51. Andreae MO, Rosenfeld D. Earth-Science Reviews Aerosol – cloud – precipitation interactions . Part 1 . The nature and sources of cloud-active aerosols. 2008;89:13-41.
doi:10.1016/j.earscirev.2008.03.001
 52. Shiraiwa M, Ueda K, Pozzer A, et al. Aerosol Health Effects from Molecular to Global Scales. *Environ Sci Technol*. 2017;51(23):13545-13567. doi:10.1021/acs.est.7b04417
 53. Partanen A ilari. Climate and health implications of future aerosol emission scenarios OPEN ACCESS Climate and health implications of future aerosol emission scenarios. Published online 2018.
 54. Bernstein JA, Alexis N, Barnes C, et al. Health effects of air pollution. *J Allergy Clin Immunol*. 2004;114(5):1116-1123. doi:10.1016/j.jaci.2004.08.030
 55. Zhang R. Getting to the Critical Nucleus of Aerosol Formation. *Science (80-)*. 2010;328:1366-1367. doi:10.2307/40656064

56. Robinson AL, Donahue NM, Shrivastava MK, et al. Rethinking organic aerosols: semivolatile emissions and photochemical aging. *Science*. 2007;315(5816):1259-1262. doi:10.1126/science.1133061
57. Zhang R, Khalizov A, Wang L, Hu M, Xu W. Nucleation and Growth of Nanoparticles in the Atmosphere. Published online 2012:1957-2011.
58. Myllys N, Olenius T, Kurte T, Vehkama H, Riipinen I, Elm J. Effect of Bisulfate, Ammonia, and Ammonium on the Clustering of Organic Acids and Sulfuric Acid. Published online 2017. doi:10.1021/acs.jpca.7b03981
59. Elm J. Toward a Holistic Understanding of the Formation and Growth of Atmospheric Molecular Clusters: A Quantum Machine Learning Perspective. Published online 2021. doi:10.1021/acs.jpca.0c09762
60. Ervens B, Turpin BJ, Weber RJ, Brunswick N, Scienc e A. and Physics Secondary organic aerosol formation in cloud droplets and aqueous particles (aqSOA): a review of laboratory, field and model studies. Published online 2011:11069-11102. doi:10.5194/acp-11-11069-2011
61. Allen S adeaga A, Godson A, Ayodeji S adeaga M, Deborah S adeaga E, Ejike M. Secondary inorganic aerosols: impacts on the global climate system and human health. 2019;3(6):249-259. doi:10.15406/bij.2019.03.00152
62. Quality AIR, Group E. *Particulate Matter in Particulate Matter In*.
63. Yang F, Duan Z, Liu D, et al. Multi-alkylated aromatic amides amphiphiles effectively stabilize the associated asphaltene particles in crude oil. *J Pet Sci Eng*.

- 2022;212(February):110204. doi:10.1016/j.petrol.2022.110204
64. Ge X, Wexler AS, Clegg SL. Atmospheric amines - Part I. A review. *Atmos Environ.* 2011;45(3):524-546. doi:10.1016/j.atmosenv.2010.10.012
65. Yao L, Wang MY, Wang XK, et al. Detection of atmospheric gaseous amines and amides by a high-resolution time-of-flight chemical ionization mass spectrometer with protonated ethanol reagent ions. *Atmos Chem Phys.* 2016;16(22):14527-14543. doi:10.5194/acp-16-14527-2016
66. Borduas N, da Silva G, Murphy JG, Abbatt JPD. Experimental and theoretical understanding of the gas phase oxidation of atmospheric amides with OH radicals: kinetics, products, and mechanisms. *J Phys Chem A.* 2015;119(19):4298-4308. doi:10.1021/jp503759f
67. Zhu L, Schade GW, Nielsen CJ. Real-time monitoring of emissions from monoethanolamine-based industrial scale carbon capture facilities. *Environ Sci Technol.* 2013;47(24):14306-14314. doi:10.1021/es4035045
68. Saeki K, Ikari K, Yokoi H, Ohira SI, Okochi H, Toda K. Biogenic Diamines and Their Amide Derivatives Are Present in the Forest Atmosphere and May Play a Role in Particle Formation. *ACS Earth Sp Chem.* 2022;6(2):421-430. doi:10.1021/acsearthspacechem.1c00404
69. Zhao H, Tang S, Xu X, Du L. Hydrogen bonding interaction between atmospheric gaseous amides and methanol. *Int J Mol Sci.* 2017;18(1):1-16. doi:10.3390/ijms18010004
70. Kulmala M. How Particles Nucleate and Grow. *Science (80-).* 2003;302(5647):1000-

1001. doi:10.1126/science.1090848
71. Bianchi F, Tröstl J, Junninen H, et al. New particle formation in the free troposphere: A question of chemistry and timing. *Science* (80-). 2016;352(6289):1109-1112.
doi:10.1126/science.aad5456
72. Duplissy J, Williamson C, Ortega IK, et al. Global atmospheric particle formation from CERN CLOUD measurements. 2016;354(6316).
73. Duarte RMBO, Santos EBH, Pio CA, Duarte AC. Comparison of structural features of water-soluble organic matter from atmospheric aerosols with those of aquatic humic substances. *Atmos Environ*. 2007;41(37):8100-8113. doi:10.1016/j.atmosenv.2007.06.034
74. Lopes SP, Matos JT V, Silva AMS, Duarte AC, Duarte RMBO. 1H NMR studies of water- and alkaline-soluble organic matter from fine urban atmospheric aerosols. *Atmos Environ*. 2015;119:374-380. doi:https://doi.org/10.1016/j.atmosenv.2015.08.072
75. Estimation C. Saccharides Emissions from Biomass and Coal Burning in Northwest China and Their Application in Source Contribution Estimation. Published online 2021.
76. Simoneit BRT, Elias VO, Kobayashi M, et al. Sugars - Dominant water-soluble organic compounds in soils and characterization as tracers in atmospheric particulate matter. *Environ Sci Technol*. 2004;38(22):5939-5949. doi:10.1021/es0403099
77. Marynowski L, Simoneit BRT. Chemosphere Saccharides in atmospheric particulate and sedimentary organic matter : Status overview and future perspectives. *Chemosphere*. 2022;288(P1):132376. doi:10.1016/j.chemosphere.2021.132376
78. Hasencz ES, Kaluarachchi CP, Lee HD, Tivanski A V, Stone EA. Saccharide Transfer to

Sea Spray Aerosol Enhanced by Surface Activity, Calcium, and Protein Interactions.

Published online 2019. doi:10.1021/acsearthspacechem.9b00197

79. Després VR, Alex Huffman J, Burrows SM, et al. Primary biological aerosol particles in the atmosphere: A review. *Tellus, Ser B Chem Phys Meteorol.* 2012;64(1).
doi:10.3402/tellusb.v64i0.15598
80. Rogge WF, Medeiros PM, Simoneit BRT. Organic marker compounds in surface soils of crop fields from the San Joaquin Valley fugitive dust characterization study. *Atmos Environ.* 2007;41(37):8183-8204. doi:10.1016/j.atmosenv.2007.06.030
81. Véléz H, Glassbrook NJ, Daub ME. Mannitol metabolism in the phytopathogenic fungus *Alternaria alternata*. *Fungal Genet Biol.* 2007;44(4):258-268.
doi:10.1016/j.fgb.2006.09.008
82. Xiao M, Wang Q, Qin X, Yu G, Deng C. Saccharides in a Coastal Urban Site of China. Published online 2018. doi:10.3390/atmos9070274
83. Wang Z, Wu D, Li Z, Shang X, Li Q, Li X. Saccharide composition in atmospheric fine particulate matter during spring at the remote sites of Southwest China and estimates of source contributions. Published online 2005:1-37.
84. Caseiro A, Marr IL, Claeys M, Kasper-giebl A, Puxbaum H, Pio CA. Determination of saccharides in atmospheric aerosol using anion-exchange high-performance liquid chromatography and pulsed-amperometric detection. 2007;1171:37-45.
doi:10.1016/j.chroma.2007.09.038
85. Srithawirat T, Brimblecombe P. Seasonal Variation of Saccharides and Furfural in

Atmospheric Aerosols at a Semi-Urban Site. Published online 2015:821-832.

doi:10.4209/aaqr.2014.07.0136

86. Richards DS, Trobaugh KL, Hajek-herrera J, et al. Ion-molecule interactions enable unexpected phase transitions in organic-inorganic aerosol. Published online 2020:1-12.
87. Cochran RE, Jonathan V, Elizabeth A, et al. Molecular Diversity of Sea Spray Aerosol Particles : Impact of Ocean Biology on Particle Composition and Hygroscopicity
Molecular Diversity of Sea Spray Aerosol Particles : Impact of Ocean Biology on Particle Composition and Hygroscopicity. :655-667. doi:10.1016/j.chempr.2017.03.007
88. Mikhailov E, Vlasenko S, Martin ST, Koop T. and Physics Amorphous and crystalline aerosol particles interacting with water vapor : conceptual framework and experimental evidence for restructuring , phase transitions and kinetic limitations. Published online 2009:9491-9522.
89. Jimenez JL, Canagaratna MR, Donahue NM, et al. Evolution of Organic Aerosols in the Atmosphere. *Science* (80-). 2009;326(5959):1525-1529. doi:10.1126/science.1180353
90. Gouw JDE, Jimenez JL. Organic Aerosols in the Earth ' s Atmosphere. 2009;43(20):7614-7618.
91. Gupta T, Rajeev P, Rajput R. Emerging Major Role of Organic Aerosols in Explaining the Occurrence , Frequency , and Magnitude of Haze and Fog Episodes during Wintertime in the Indo Gangetic Plain. Published online 2022. doi:10.1021/acsomega.1c05467
92. Lin C, Huo T, Yang F, Wang B, Chen Y, Wang H. Characteristics of Water-soluble Inorganic Ions in Aerosol and Precipitation and their Scavenging Ratios in an Urban

Environment in Southwest China.

93. Satsangi A, Pachauri T, Singla V, Lakhani A, Kumari KM. Water Soluble Ionic Species in Atmospheric Aerosols : Concentrations and Sources at Agra in the Indo-Gangetic Plain (IGP). Published online 2013:1877-1889. doi:10.4209/aaqr.2012.08.0227
94. Huy DH, Thanh LT, Hien TT, Takenaka N. Comparative study on water-soluble inorganic ions in PM_{2.5} from two distinct climate regions and air quality. *J Environ Sci.* 2020;88:349-360. doi:https://doi.org/10.1016/j.jes.2019.09.010
95. Kwon HS, Ryu MH, Carlsten C. Ultrafine particles: unique physicochemical properties relevant to health and disease. *Exp Mol Med.* 2020;52(3):318-328. doi:10.1038/s12276-020-0405-1
96. Gieré R, Querol X. Solid particulate matter in the atmosphere. *Elements.* 2010;6(4):215-222. doi:10.2113/gselements.6.4.215
97. Koop T, Bookhold J, Shiraiwa M, Pöschl U. Glass transition and phase state of organic compounds: dependency on molecular properties and implications for secondary organic aerosols in the atmosphere. *Phys Chem Chem Phys.* 2011;13(43):19238-19255. doi:10.1039/C1CP22617G
98. Shiraiwa M, Ammann M, Koop T, Pöschl U. Gas uptake and chemical aging of semisolid organic aerosol particles. *Proc Natl Acad Sci U S A.* 2011;108(27):11003-11008. doi:10.1073/pnas.1103045108
99. Gaikwad S, Jeong R, Kim D, et al. Microscopic observation of a liquid-liquid-(semi)solid phase in polluted PM_{2.5}. *Front Environ Sci.* 2022;10(July):1-9.

doi:10.3389/fenvs.2022.947924

100. Huang Y, Mahrt F, Xu S, Shiraiwa M, Zuend A, Bertram AK. Coexistence of three liquid phases in individual atmospheric aerosol particles. *Proc Natl Acad Sci U S A*. 2021;118(16). doi:10.1073/pnas.2102512118
101. Song YC, Lilek J, Lee JB, et al. Viscosity and phase state of aerosol particles consisting of sucrose mixed with inorganic salts. *Atmos Chem Phys*. 2021;21(13):10215-10228. doi:10.5194/acp-21-10215-2021
102. Ullmann DA, Hinks ML, MacLean AM, et al. Viscosities, diffusion coefficients, and mixing times of intrinsic fluorescent organic molecules in brown limonene secondary organic aerosol and tests of the Stokes-Einstein equation. *Atmos Chem Phys*. 2019;19(3):1491-1503. doi:10.5194/acp-19-1491-2019
103. Shiraiwa M, Seinfeld JH. Equilibration timescale of atmospheric secondary organic aerosol partitioning. *Geophys Res Lett*. 2012;39(24):1-6. doi:10.1029/2012GL054008
104. Saleh R, Donahue NM, Robinson AL. Time scales for gas-particle partitioning equilibration of secondary organic aerosol formed from alpha-pinene ozonolysis. *Environ Sci Technol*. 2013;47(11):5588-5594. doi:10.1021/es400078d
105. Zhao D, Yin Y, Zhang M, et al. The optical properties of aerosols at the summit of Mount Tai in May and June and the retrieval of the complex refractive index. *Atmosphere (Basel)*. 2020;11(6). doi:10.3390/atmos11060655
106. Di Biagio C, Formenti P, Balkanski Y, et al. Complex refractive indices and single-scattering albedo of global dust aerosols in the shortwave spectrum and relationship to

- size and iron content. *Atmos Chem Phys*. 2019;19(24):15503-15531. doi:10.5194/acp-19-15503-2019
107. Hänel G. Optical properties of atmospheric particles: complete parameter sets obtained through polar photometry and an improved inversion technique. *Appl Opt*. 1994;33(30):7187-7199. doi:10.1364/AO.33.007187
108. Cotterell MI, Knight JW, Reid JP, Orr-Ewing AJ. Accurate Measurement of the Optical Properties of Single Aerosol Particles Using Cavity Ring-Down Spectroscopy. *J Phys Chem A*. 2022;126(17):2619-2631. doi:10.1021/acs.jpca.2c01246
109. Panayiotou C. Interfacial tension and interfacial profiles of fluids and their mixtures. *Langmuir*. 2002;18(23):8841-8853. doi:10.1021/la0204139
110. Sedlmeier F, Horinek D, Netz RR. Nanoroughness, Intrinsic Density Profile, and Rigidity of the Air-Water Interface. *Phys Rev Lett*. 2009;103(13):136102. doi:10.1103/PhysRevLett.103.136102
111. Söngen H, Schlegel SJ, Morais Jaques Y, et al. Water Orientation at the Calcite-Water Interface. *J Phys Chem Lett*. 2021;12(31):7605-7611. doi:10.1021/acs.jpcclett.1c01729
112. Cipcigan FS, Sokhan VP, Jones AP, Crain J, Martyna GJ. Hydrogen bonding and molecular orientation at the liquid-vapour interface of water. *Phys Chem Chem Phys*. 2015;17(14):8660-8669. doi:10.1039/c4cp05506c
113. Hauner IM, Deblais A, Beattie JK, Kellay H, Bonn D. The Dynamic Surface Tension of Water. *J Phys Chem Lett*. 2017;8(7):1599-1603. doi:10.1021/acs.jpcclett.7b00267
114. Gibbs G.W. - Collected works. Thermodynamics. Volume 1-Longmans (1928).pdf.

115. Meza MSP, Cantero-López P, Sotelo DEP, Arias FJP, Varilla LAA. A strategy for characterizing the surface layer at the liquid-vapor interface of binary liquid mixtures containing non-ionic surfactants: An approach from Gibbs adsorption isotherm. *Fluid Phase Equilib.* 2021;541:113090. doi:<https://doi.org/10.1016/j.fluid.2021.113090>
116. Radke CJ. Gibbs adsorption equation for planar fluid-fluid interfaces: Invariant formalism. *Adv Colloid Interface Sci.* 2015;222:600-614. doi:10.1016/j.cis.2014.01.001
117. Pegram LM, Record MT. Using surface tension data to predict differences in surface and bulk concentrations of nonelectrolytes in water. *J Phys Chem C.* 2009;113(6):2171-2174. doi:10.1021/jp8073305
118. Whitman WG. The two film theory of gas absorption. *Int J Heat Mass Transf.* 1962;5(5):429-433. doi:10.1016/0017-9310(62)90032-7
119. Ponche JL, George C, Mirabel P. Mass transfer at the air/water interface: Mass accommodation coefficients of SO₂, HNO₃, NO₂ and NH₃. *J Atmos Chem.* 1993;16(1):1-21. doi:10.1007/BF00696620
120. Harriott P. A random eddy modification of the penetration theory. *Chem Eng Sci.* 1962;17(3):149-154. doi:[https://doi.org/10.1016/0009-2509\(62\)80026-8](https://doi.org/10.1016/0009-2509(62)80026-8)
121. Mansfield ML. Mass transport of gases across the air-water interface: implications for aldehyde emissions in the Uinta basin, Utah, USA. *Atmosphere (Basel).* 2020;11(10). doi:10.3390/atmos11101057
122. Lee L, Wilson K. The Reactive-Diffusive Length of OH and Ozone in Model Organic Aerosols. *J Phys Chem A.* 2016;120(34):6800-6812. doi:10.1021/acs.jpca.6b05285

123. Moise T, Rudich Y. Reactive uptake of ozone by aerosol-associated unsaturated fatty acids: kinetics, mechanism, and products. *J Phys Chem B*. 2002;106(27):6469-6476. doi:10.1021/jp025597e
124. Bertram AK, Ivanov A V, Hunter M, Molina LT, Molina MJ. The reaction probability of OH on organic surfaces of tropospheric interest. *J Phys Chem A*. 2001;105. doi:10.1021/jp0114034
125. Molina MJ, Ivanov A V., Trakhtenberg S, Molina LT. Atmospheric evolution of organic aerosol. *Geophys Res Lett*. 2004;31(22):1-5. doi:10.1029/2004GL020910
126. Moise T, Rudich Y. Uptake of Cl and Br by organic surfaces - A perspective on organic aerosols processing by tropospheric oxidants. *Geophys Res Lett*. 2001;28(21):4083-4086. doi:10.1029/2001GL013583
127. Lambe AT, Miracolo MA, Hennigan CJ, Robinson AL, Donahue NM. Effective rate constants and uptake coefficients for the reactions of organic molecular markers (n-alkanes, hopanes, and steranes) in motor oil and diesel primary organic aerosols with hydroxyl radicals. *Environ Sci Technol*. 2009;43(23):8794-8800. doi:10.1021/es901745h
128. Smith JD, Kroll JH, Cappa CD, et al. The heterogeneous reaction of hydroxyl radicals with sub-micron squalane particles: A model system for understanding the oxidative aging of ambient aerosols. *Atmos Chem Phys*. 2009;9(9):3209-3222. doi:10.5194/acp-9-3209-2009
129. McNeill VF, Yatavelli RLN, Thornton JA, Stipe CB, Landgrebe O. Heterogeneous OH oxidation of palmitic acid in single component and internally mixed aerosol particles: Vaporization and the role of particle phase. *Atmos Chem Phys*. 2008;8(17):5465-5476.

doi:10.5194/acp-8-5465-2008

130. Li J, Knopf DA. Representation of Multiphase OH Oxidation of Amorphous Organic Aerosol for Tropospheric Conditions. *Environ Sci Technol*. 2021;55(11):7266-7275.
doi:10.1021/acs.est.0c07668
131. Worsnop DR, Morris JW, Shi Q, Davidovits P, Kolb CE. A chemical kinetic model for reactive transformations of aerosol particles. *Geophys Res Lett*. 2002;29(20):4-7.
doi:10.1029/2002GL015542
132. Smith JD, Kroll JH, Cappa CD, et al. The heterogeneous reaction of hydroxyl radicals with sub-micron squalane particles: A model system for understanding the oxidative aging of ambient aerosols. *Atmos Chem Phys*. 2009;9(9):3209-3222. doi:10.5194/acp-9-3209-2009
133. Renbaum-Wolff L, Smith GD. “Virtual injector” flow tube method for measuring relative rates kinetics of gas-phase and aerosol species. *J Phys Chem A*. 2012;116(25):6664-6674.
doi:10.1021/jp303221w
134. Cheng Y. Reactive uptake coefficients for multiphase reactions determined by a dynamic chamber system. *Atmos Meas Tech*. 2022;(July):1-23.
https://amt.copernicus.org/preprints/amt-2022-211/?utm_source=researcher_app&utm_medium=referral&utm_campaign=RESR_MRKT_Researcher_inbound
135. Prigogine I. Chemical kinetics and dynamics. *Ann N Y Acad Sci*. 2003;988:128-132.
doi:10.1111/j.1749-6632.2003.tb06091.x

136. George IJ, Abbatt JPD. Heterogeneous oxidation of atmospheric aerosol particles by gas-phase radicals. *Nat Chem*. 2010;2(9):713-722. doi:10.1038/nchem.806
137. Steinfeld JI, Francisco JS, Hase WL. *Chemical Kinetics and Dynamics*. Prentice Hall Upper Saddle River, NJ; 1999.
138. Weinberg WH. Eley-Rideal Surface Chemistry: Direct Reactivity of Gas Phase Atomic Hydrogen with Adsorbed Species. *Acc Chem Res*. 1996;29(10):479-487. doi:10.1021/ar9500980
139. Bagot PAJ, Waring C, Costen ML, McKendrick KG. Dynamics of inelastic scattering of OH radicals from reactive and inert liquid surfaces. *J Phys Chem C*. 2008;112(29):10868-10877. doi:10.1021/jp8024683
140. Vlasenko A, George IJ, Abbatt JPD. Formation of volatile organic compounds in the heterogeneous oxidation of condensed-phase organic films by gas-phase OH. *J Phys Chem A*. 2008;112(7):1552-1560. doi:10.1021/jp0772979
141. Ishiyama T, Tahara T, Morita A. Why the Photochemical Reaction of Phenol Becomes Ultrafast at the Air-Water Interface: The Effect of Surface Hydration. *J Am Chem Soc*. 2022;144(14):6321-6325. doi:10.1021/jacs.1c13336
142. Gross S, Iannone R, Xiao S, Bertram AK. Reactive uptake studies of NO₃ and N₂O₅ on alkenoic acid{,} alkanoate{,} and polyalcohol substrates to probe nighttime aerosol chemistry. *Phys Chem Chem Phys*. 2009;11(36):7792-7803. doi:10.1039/B904741G
143. Wilson KR, Prophet AM, Rovelli G, Willis MD, Rapf RJ, Jacobs MI. A kinetic description of how interfaces accelerate reactions in micro-compartments. *Chem Sci*.

2020;11(32):8533-8545. doi:10.1039/d0sc03189e

144. Prisle NL, Ottosson N, Öhrwall G, Söderström J, Dal Maso M, Björneholm O. Surface/bulk partitioning and acid/base speciation of aqueous decanoate: Direct observations and atmospheric implications. *Atmos Chem Phys*. 2012;12(24):12227-12242. doi:10.5194/acp-12-12227-2012
145. Kumar M, Zhong J, Zeng XC, Francisco JS. Reaction of Criegee Intermediate with Nitric Acid at the Air-Water Interface. *J Am Chem Soc*. 2018;140(14):4913-4921. doi:10.1021/jacs.8b01191
146. Kusaka R, Nihonyanagi S, Tahara T. The photochemical reaction of phenol becomes ultrafast at the air-water interface. *Nat Chem*. 2021;13(4):306-311. doi:10.1038/s41557-020-00619-5
147. Valsaraj KT. A Review of the Aqueous Aerosol Surface Chemistry in the Atmospheric Context. 2012;2012(February):58-66.
148. Chen J, Ehrenhauser FS, Valsaraj KT, Wornat MJ. Uptake and UV-photooxidation of gas-phase PAHs on the surface of atmospheric water films. 1. Naphthalene. *J Phys Chem A*. 2006;110(29):9161-9168. doi:10.1021/jp062560b
149. Chen J, Ehrenhauser FS, Valsaraj KT, Wornat MJ. Adsorption and UV photooxidation of gas-phase phenanthrene on atmospheric films. *ACS Symp Ser*. 2009;1005:127-146. doi:10.1021/bk-2009-1005.ch009
150. Yan X, Bain RM, Cooks RG. Organic Reactions in Microdroplets: Reaction Acceleration Revealed by Mass Spectrometry. *Angew Chemie Int Ed*. 2016;55(42):12960-12972.

doi:<https://doi.org/10.1002/anie.201602270>

151. Li Y, Mehari TF, Wei Z, Liu Y, Cooks RG. Reaction acceleration at air-solution interfaces: Anisotropic rate constants for Katritzky transamination. *J Mass Spectrom.* 2021;56(4):1-8. doi:10.1002/jms.4585
152. Lee JK, Walker KL, Han HS, et al. Spontaneous generation of hydrogen peroxide from aqueous microdroplets. *Proc Natl Acad Sci U S A.* 2019;116(39):19294-19298. doi:10.1073/pnas.1911883116
153. Lee JK, Han HS, Chaikasetsin S, et al. Condensing water vapor to droplets generates hydrogen peroxide. *Proc Natl Acad Sci U S A.* 2020;117(49):30934-30941. doi:10.1073/pnas.2020158117
154. Musskopf NH, Gallo AJ, Zhang P, Petry J, Mishra H. The Air–Water Interface of Water Microdroplets Formed by Ultrasonication or Condensation Does Not Produce H₂O₂. *J Phys Chem Lett.* 2021;12(46):11422-11429. doi:10.1021/acs.jpcclett.1c02953
155. Nam I, Lee JK, Nam HG, Zare RN. Abiotic production of sugar phosphates and uridine ribonucleoside in aqueous microdroplets. *Proc Natl Acad Sci U S A.* 2017;114(47):12396-12400. doi:10.1073/pnas.1714896114
156. Hao H, Leven I, Head-Gordon T. Can electric fields drive chemistry for an aqueous microdroplet? *Nat Commun.* 2022;13(1):1-8. doi:10.1038/s41467-021-27941-x
157. Lee JK, Walker KL, Han HS, et al. Spontaneous generation of hydrogen peroxide from aqueous microdroplets. *Proc Natl Acad Sci U S A.* 2019;116(39):19294-19298. doi:10.1073/pnas.1911883116

158. Gallo Jr. A, Musскопff NH, Liu X, et al. On the formation of hydrogen peroxide in water microdroplets. *Chem Sci*. 2022;13(9):2574-2583. doi:10.1039/D1SC06465G
159. Gassin PM, Girard L, Martin-Gassin G, et al. Surface Activity and Molecular Organization of Metallacarboranes at the Air–Water Interface Revealed by Nonlinear Optics. *Langmuir*. 2015;31(8):2297-2303. doi:10.1021/acs.langmuir.5b00125
160. Shultz MJ, Vu TH, Meyer B, Bisson P. Water: a responsive small molecule. *Acc Chem Res*. 2012;45(1):15-22. doi:10.1021/ar200064z
161. Chen X, Minofar B, Jungwirth P, Allen HC. Interfacial Molecular Organization at Aqueous Solution Surfaces of Atmospherically Relevant Dimethyl Sulfoxide and Methanesulfonic Acid Using Sum Frequency Spectroscopy and Molecular Dynamics Simulation. *J Phys Chem B*. 2010;114(47):15546-15553. doi:10.1021/jp1078339
162. Watry MR, Richmond GL. Orientation and Conformation of Amino Acids in Monolayers Adsorbed at an Oil/Water Interface As Determined by Vibrational Sum-Frequency Spectroscopy. *J Phys Chem B*. 2002;106(48):12517-12523. doi:10.1021/jp021469e
163. Rode BM, Schwenk CF, Randolph BR. Classical Versus Quantum Mechanical Simulations: The Accuracy of Computer Experiments in Solution Chemistry BT - Novel Approaches to the Structure and Dynamics of Liquids: Experiments, Theories and Simulations. In: Samios J, Durov VA, eds. Springer Netherlands; 2004:41-52. doi:10.1007/978-1-4020-2384-2_3
164. Ponder JW, Case DA. Force fields for protein simulations. *Adv Protein Chem*. 2003;66:27-85. doi:10.1016/s0065-3233(03)66002-x

165. Barnett RN, Landman U. Born-Oppenheimer molecular-dynamics simulations of finite systems: Structure and dynamics of $(\mathrm{H})_2\mathrm{O}$. *Phys Rev B*. 1993;48(4):2081-2097. doi:10.1103/PhysRevB.48.2081
166. Azam S, Ul-Haq Z, Fatmi MQ. Classical and QM/MM MD simulations of sodium(I) and potassium(I) ions in aqueous solution. *J Mol Liq*. 2010;153:95-100. doi:10.1016/j.molliq.2010.01.005
167. Frenkel D, Smit B. Understanding molecular simulation. From algorithms to applications (2002, Academic Press). Published online 2002:658. [https://www.eng.uc.edu/~beaucag/Classes/AdvancedMaterialsThermodynamics/Books/%5BComputational science \(San Diego, Calif.\)%5D Daan Frenkel_ Berend Smit - Understanding molecular simulation _ from algorithms to applications \(2002, Academic Press \) - libgen](https://www.eng.uc.edu/~beaucag/Classes/AdvancedMaterialsThermodynamics/Books/%5BComputational%20science%20(San%20Diego,%20Calif.)%5D%20Daan%20Frenkel%20Berend%20Smit%20-%20Understanding%20molecular%20simulation%20-%20from%20algorithms%20to%20applications%20(2002,%20Academic%20Press)%20-%20libgen)
168. Akbas H, Turgut OT. Born-Oppenheimer approximation for a singular system. *J Math Phys*. 2018;59(1):12107. doi:10.1063/1.5021364
169. Combes JM, Duclos P, Seiler R. The Born-Oppenheimer Approximation BT - Rigorous Atomic and Molecular Physics. In: Velo G, Wightman AS, eds. Springer US; 1981:185-213. doi:10.1007/978-1-4613-3350-0_5
170. Woolley RG, Sutcliffe BT. Molecular structure and the born—Oppenheimer approximation. *Chem Phys Lett*. 1977;45(2):393-398. doi:https://doi.org/10.1016/0009-2614(77)80298-4
171. Duane S, Kennedy AD, Pendleton BJ, Roweth D. Hybrid Monte Carlo. *Phys Lett B*. 1987;195(2):216-222. doi:https://doi.org/10.1016/0370-2693(87)91197-X

172. Fichthorn KA, Weinberg WH. Theoretical foundations of dynamical Monte Carlo simulations. *J Chem Phys.* 1991;95(2):1090-1096. doi:10.1063/1.461138
173. Izvekov S, Voth GA. Modeling real dynamics in the coarse-grained representation of condensed phase systems. *J Chem Phys.* 2006;125(15):151101. doi:10.1063/1.2360580
174. Wu X, Brooks BR. Self-guided Langevin dynamics simulation method. *Chem Phys Lett.* 2003;381(3-4):512-518. doi:10.1016/j.cplett.2003.10.013
175. Erban R. From molecular dynamics to Brownian dynamics. *Proc R Soc A Math Phys Eng Sci.* 2014;470(2167). doi:10.1098/rspa.2014.0036
176. Roy K, Kar S, Das RN. Chapter 5 - Computational Chemistry. In: Roy K, Kar S, Das RN, eds. *Computational Chemistry: The B of Q for A in PS and RA*, eds. Academic Press; 2015:151-189. doi:https://doi.org/10.1016/B978-0-12-801505-6.00005-3
177. Scott A, Hollingsworth, Ron O, Dror. Molecular dynamics simulation for all. *Neuron.* 2018;99(6)(1):1129-1143. doi:10.1016/j.neuron.2018.08.011.Molecular
178. Wang X, Chen C, Binder K, et al. Molecular dynamics simulation of the surface tension of aqueous sodium chloride: from dilute to highly supersaturated solutions and molten salt. *Atmos Chem Phys.* 2018;18(23):17077-17086. doi:10.5194/acp-18-17077-2018
179. Vieceli J, Roeselova M, Potter N, Dang LX, Garrett BC, Tobias DJ. Molecular dynamics simulations of atmospheric oxidants at the air-water interface: solvation and accommodation of OH and O₃. *J Phys Chem B.* 2005;109(33):15876-15892. doi:10.1021/jp051361+
180. Pezzotti S, Serva A, Gaigeot MP. 2D-HB-Network at the air-water interface: A structural

- and dynamical characterization by means of ab initio and classical molecular dynamics simulations. *J Chem Phys.* 2018;148(17):174701. doi:10.1063/1.5018096
181. Liu P, Harder E, Berne BJ. Hydrogen-Bond Dynamics in the Air - Water Interface. Published online 2005:2949-2955.
182. Kühne TD, Pascal TA, Kaxiras E, Jung Y. New insights into the structure of the vapor/water interface from large-scale first-principles simulations. *J Phys Chem Lett.* 2011;2(2):105-113. doi:10.1021/jz101391r
183. Pegram LM, Record MT. Partitioning of atmospherically relevant ions between bulk water and the water/vapor interface. *Proc Natl Acad Sci U S A.* 2006;103(39):14278-14281. doi:10.1073/pnas.0606256103
184. Litwinienko G, Ingold KU. Solvent effects on the rates and mechanisms of reaction of phenols with free radicals. *Acc Chem Res.* 2007;40(3):222-230. doi:10.1021/ar0682029
185. Ghosal S, Brown MA, Bluhm H, Krisch MJ, Jungwirth P, Hemminger JC. solution : A model for aqueous sea salt aerosols.
186. Roeselová M, Vieceli J, Dang LX, Garrett BC, Tobias DJ. Hydroxyl radical at the air-water interface. *J Am Chem Soc.* 2004;126(50):16308-16309. doi:10.1021/ja045552m
187. Rana B, Herbert JM. Hidden Hemibonding in the Aqueous Hydroxyl Radical. *J Phys Chem Lett.* 2021;12(33):8053-8060. doi:10.1021/acs.jpcclett.1c02283
188. Ruehl CR, Davies JF, Wilson KR. An interfacial mechanism for cloud droplet formation on organic aerosols. *Science.* 2016;351(6280):1447-1450. doi:10.1126/science.aad4889
189. Boyer HC, Dutcher CS. Atmospheric Aqueous Aerosol Surface Tensions: Isotherm-Based

- Modeling and Biphasic Microfluidic Measurements. *J Phys Chem A*. 2017;121(25):4733-4742. doi:10.1021/acs.jpca.7b03189
190. Burkholder JB, Abbatt JPD, Barnes I, et al. The Essential Role for Laboratory Studies in Atmospheric Chemistry. *Environ Sci Technol*. 2017;51(5):2519-2528. doi:10.1021/acs.est.6b04947
191. Shepherd RH, King MD, Rennie AR, et al. Measurement of gas-phase OH radical oxidation and film thickness of organic films at the air-water interface using material extracted from urban, remote and wood smoke aerosol. *Environ Sci Atmos*. 2022;2(4):574-590. doi:10.1039/d2ea00013j
192. Ravishankara AR. Heterogeneous and Multiphase Chemistry in the Troposphere. *Science* (80-). 1997;276(5315):1058-1065. doi:10.1126/science.276.5315.1058
193. Gubanova DP, Elansky NF, Skorokhod AI, et al. Physical and chemical properties of atmospheric aerosols in Moscow and its suburb for climate assessments. *IOP Conf Ser Earth Environ Sci*. 2020;606(1). doi:10.1088/1755-1315/606/1/012019
194. Su H, Cheng Y, Pöschl U. New Multiphase Chemical Processes Influencing Atmospheric Aerosols, Air Quality, and Climate in the Anthropocene. *Acc Chem Res*. 2020;53(10):2034-2043. doi:10.1021/acs.accounts.0c00246
195. Shiraiwa M, Zuend A, Bertram AK, Seinfeld JH. Gas-particle partitioning of atmospheric aerosols: interplay of physical state{,} non-ideal mixing and morphology. *Phys Chem Chem Phys*. 2013;15(27):11441-11453. doi:10.1039/C3CP51595H
196. Houle FA, Hinsberg WD, Wilson KR. Oxidation of a model alkane aerosol by OH radical:

- the emergent nature of reactive uptake. *Phys Chem Chem Phys*. 2015;17(6):4412-4423.
doi:10.1039/C4CP05093B
197. Davies J, Haddrell A, Miles R, Bull C, Reid J. Bulk, Surface, and Gas-Phase Limited Water Transport in Aerosol. *J Phys Chem A*. 2012;116. doi:10.1021/jp3086667
198. Davies JF, Haddrell AE, Miles REH, Bull CR, Reid JP. Bulk, surface, and gas-phase limited water transport in aerosol. *J Phys Chem A*. 2012;116(45):10987-10998.
doi:10.1021/jp3086667
199. Shiraiwa M, Pöschl U. Mass accommodation and gas-particle partitioning in secondary organic aerosols: Dependence on diffusivity, volatility, particle-phase reactions, and penetration depth. *Atmos Chem Phys*. 2021;21(3):1565-1580. doi:10.5194/acp-21-1565-2021
200. Knipping EM, Lakin MJ, Foster KL, et al. Experiments and Simulations of Ion-Enhanced Interfacial Chemistry on Aqueous NaCl Aerosols. *Science (80-)*. 2000;288(5464):301-306. <http://www.jstor.org/stable/3075145>
201. Woden B, Skoda MWA, Hagreen M, Pfrang C. Night-Time Oxidation of a Monolayer Model for the Air–Water Interface of Marine Aerosols—A Study by Simultaneous Neutron Reflectometry and in Situ Infra-Red Reflection Absorption Spectroscopy (IRRAS). *Atmosphere (Basel)*. 2018;9(12). doi:10.3390/atmos9120471
202. Compounds VO, Rao RG, Vejerano EP. *Version of Record*:
<https://www.sciencedirect.com/science/article/pii/S0045653518315534>.; 2018.
203. Smith GD, Woods E, DeForest CL, Baer T, Miller RE. Reactive Uptake of Ozone by

Oleic Acid Aerosol Particles: Application of Single-Particle Mass Spectrometry to Heterogeneous Reaction Kinetics. *J Phys Chem A*. 2002;106(35):8085-8095.

doi:10.1021/jp020527t

2 Experimental methods, theoretical simulations, and models

2.1 Overall experimental setup

Figure 2.1 depicts the setup of the flow reactor used for the offline kinetics experiments done in this study. Firstly, an aerosol of multicomponent aqueous organic particles was generated by nebulizing an equimolar aqueous solution using a constant output atomizer (TSI, model3076). The solution being nebulized contained a combination of any two of the molecules of interest (propionamide, acetamide, urea, glucose, MGP, and lactose) at a concentration of 0.0128Mol/L for each reactant. The aqueous solution was nebulized under a 1.5L min^{-1} N_2 flow. The 1.5L min^{-1} particle flow was then flown into a 3 L Erlenmeyer flask which served both as a mixing chamber and a flow stabilizer. The residue time in the mixing chamber was estimated to be 84s. 0.1L min^{-1} of O_2 (~5% of overall flow) and 0.2L min^{-1} of a varying O_3 to N_2 ratio was added to the 1.5L min^{-1} aerosol flow before being flown into the reaction tube. The total flow (1.9L min^{-1}) was then flown into a 45-inch long and 1-inch I.D. quartz tube surrounded by three UV lamps (UVP, $\lambda=254\text{ nm}$). A total resident time of the order of 18s in the flow tube was determined.

The O_3 was generated by passing a flow varying O_3 to N_2 ratio, through an ozone generator (AC-500G, Ozone Solutions, 0.87 g/hr). The O_3 concentration in the flow tube was consequently varied by the ratio of O_3 to N_2 flowing through the ozone generator. The OH radicals were then generated by photolysis of ozone in the presence of water vapor. The amount of OH radicals was varied by changing the concentration of ozone in the flow tube.

The mixed-phase relative rate approach was used in this kinetic study and hexane was chosen as the gas-phase reference compound to quantify the time average OH radical concentration. The initial hexane concentration entering the flow tube was 3 ppm and was injected at a height of 2/5 of the total tube length from the bottom of the flow tube through a 1/8-inch I.D. Teflon tube. The

OH exposure for the whole flow tube was obtained by injecting hexane first into the top of the flow tube and then separately through the bottom 2/5 of the flow tube at a relatively low O₃ concentration. A correction factor was obtained and then applied to all OH exposure measurements. The decay of the relative hexane concentration is monitored by gas chromatography coupled to a flame ionization detector (FID) (Thermo Scientific Trace GC 2000).

On exiting the quartz tube, a 0.3 L min⁻¹ portion of the total flow was diverted to the scanning mobility particle sizer (SMPS) (TSI, model 3936) for particle characterization. The diverted sample passed through an ozone denuder to remove an excess O₃. On the same exit, another 0.05 L min⁻¹ sample of the total flow was passed through a packed potassium iodide tube to remove O₃ on its way to the GC-FID for hexane measurement.

The remaining portion of the flow was then passed through a PTFE (polytetrafluoroethylene) filter (Millipore FALP, 1.0 μm, diameter 47mm) to collect samples for offline GS-MS analysis. The collection was performed for different times depending on the constituents of the particle being analyzed, ranging from 1hr to 3hr.

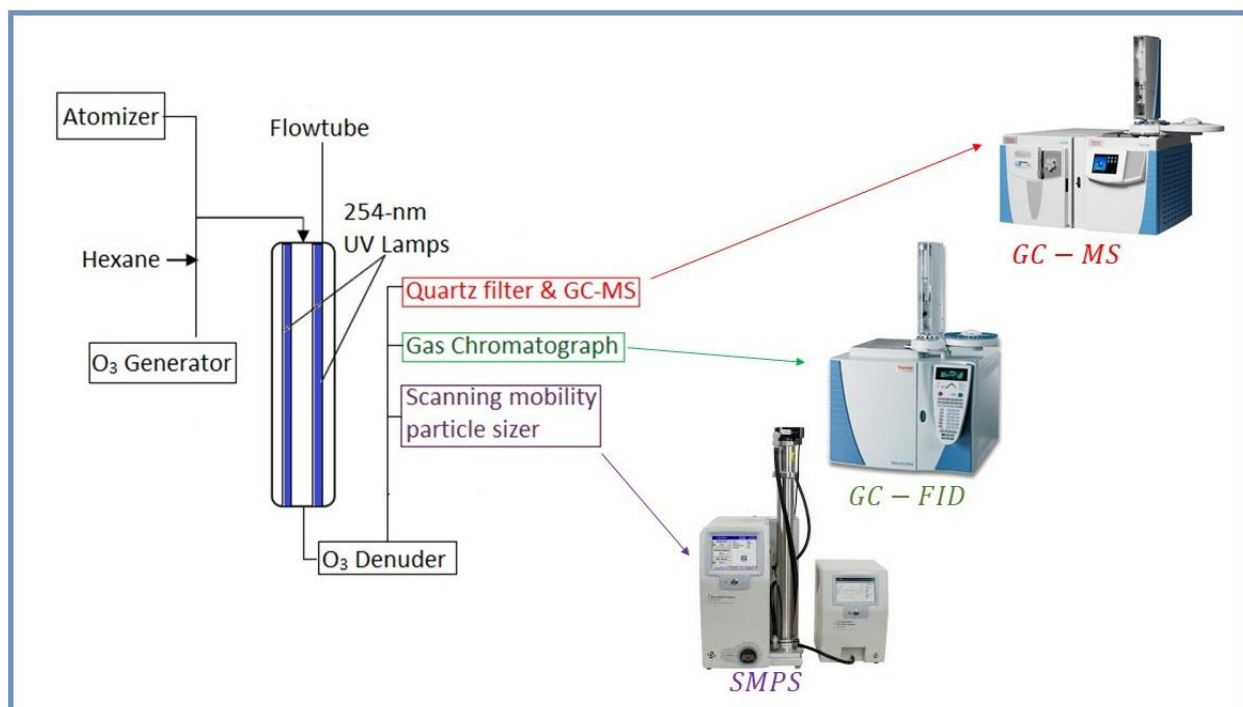


Figure 2.1 A depiction of the experimental setup used for the offline kinetics studies of the heterogeneous oxidation of aqueous organic aerosol particles.

2.1.1 Physical Particle Characterization: Scanning Mobility Particle Sizer

The physical characterization of aerosol particles generated for this study was done using the Scanning Mobility Particle Sizer (SMPS) (TSI Model 3936) system. The system constitutes of an Electrostatic Classifier (TSI Model 3080), which consists of a soft X-ray diffusion charger and a long Differential Mobility Analyzer (TSI 3081 long-DMA), and a Condensation Particle Counter (TSI Model 3775).

The electrostatic classifier is an instrument mostly used in aerosol research for both particle sizing and for generation of monodisperse aerosols. Most electrostatic classifier can perform the above-mentioned tasks over a particle size range 5nm to 10000 nm. An Electrostatic classifier operates on the physical principle that the velocity of a charged spherical particle in an electric field is directly related to the diameter of the particle.¹ Here a description of how the classifier

used for this study operated is given. When an aerosol flow is being introduced into the Electrostatic classifier it first passes through the impactor. The impactor removes particles larger than 1000 nm first. From the impactor the aerosol flow passes into the long Differential Mobility Analyzer (DMA), where the diffusion charger provides a known charge distribution on to the aerosols. Figure 2.2 shows a depiction of the components making up the electrostatic classifier. The polydisperse aerosol enters the top of the DMA through a 17.468-inch long tube. A sufficient portion of the flow is then sampled and the rest is discarded through the bypass outlet. Sheath air is flown in the same direction as the sample at a flowrate 10 times that of the sample flowrate. As the combined flow moves down the DMA positively charged particles stick to the outer electrodes and neutral particles are removed together with the excess air. Negatively charged particles with a narrow range of electrical mobility exit the DMA through the monodisperse aerosol outlet. The negatively charged particles are directed to this outlet by the two high-voltage positively charged rods at the center of the DMA. Electrical mobility, Z_p , is a ratio of particle charge to particle diameter and is calculated from the following equation:

$$Z_p = \frac{neC}{3\pi\mu D_p} \quad (2.1)$$

Where n is the number of elemental charge on the particle, e is the elementary charge (1.6×10^{-19} Colomb), C is the Cunningham slip correction, μ is gas viscosity and D_p is the particle diameter.

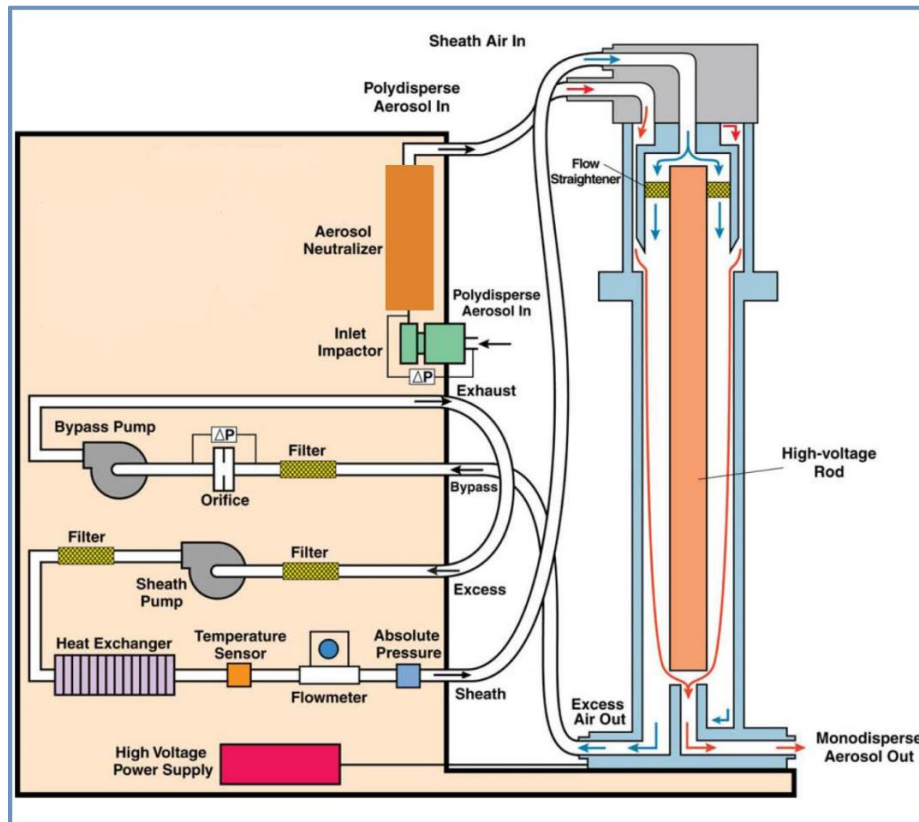


Figure 2.2 Schematic of the components making up the particle classifying system.²

A condensation particle counter (CPC) is a particle counter that is used to detect and count aerosol particles with high accuracy. The CPC used for this study made use of n-butanol as the working fluid. Particles leaving the classifier as a monodisperse enter the heated CPC saturator ($T=39^{\circ}\text{C}$) which contains butanol vapors. The butanol vapor together with the particle stream then flow into the condenser ($T=14^{\circ}\text{C}$). In the condenser large particles form as butanol vapors condense around the aerosol particles, which serve as condensation nucleation centers. The larger particles formed 1 to $10\mu\text{m}$ can be detected by light scattering.³

2.1.2 Particle Composition Characterization: GC-MS analysis

The composition of the aerosol particles was done offline using a GC-MS. The conditions and procedures used depended on the starting composition of the particles being analyzed. The analytical methods developed and used are full explained in chapter 3 along with the method validation.

2.1.3 Relative Rate Measurements in Gas-phase Reactions: GC-FID and Hexane

Measuring the concentration of OH radical remains a prevailing challenge due to the short life span of the radical. For this study the rate constant for the OH radical oxidation of various organic compounds was done using a mixed-phase relative rate approach. This approach eliminates the need to measure the concentration of the OH radicals and to establish absolute reaction times^{4,5}. For this study, the approach requires the use of a gas-phase reference compound that had a known reaction rate with OH radical, did not react with any of the other species under study and had no other significant sink hole apart from reaction with OH radical. Hexane was chosen as the gas-phase reference compound because well-established reaction rate with OH radical $5.2 \times 10^{-12} \text{ cm}^3 \text{ s}^{-1}$ (6) and it was found that more than 99% loss of hexane is due to the reaction with OH radicals.⁷ The time dependent decay of hexane due to the reaction with OH radicals is determined using the following equation:

$$\frac{d[Hex]}{dt} = -k_{hex} \cdot [OH] \cdot [Hex] \quad (2.2)$$

Where $[Hex]$ and $[OH]$ are the concentration of hexane and OH (molecules cm^{-3}) in the flow tube, respectively. t is the reaction time (s) and k_{hex} is the second-order rate constant ($\text{cm}^3 \text{ s}^{-1}$). The reference compound and the aqueous aerosols particles (containing organic reactants) are well mixed and subjected to the same amount of OH radical for equal periods. This can be expressed as the OH exposure. The OH exposure was obtained from the measured loss of the

gas-phase reference compound, Hexane, using the integrated rate law for its reaction with OH radical:

$$OH \text{ exposure} = -\frac{\ln\left(\frac{[Hex]_t}{[Hex]_0}\right)}{k_{hex}} = \int_0^t [OH] dt = \langle OH \rangle_{t.t} \quad (2.3)$$

Where $[Hex]_0$ is the initial concentration of hexane before any OH radical are introduced, and $[Hex]_t$ is the concentration of hexane after being exposed to OH radicals. $\langle OH \rangle_{t.t}$ is the time averaged concentration of OH, or the OH exposure. The loss of the gas-phase reference compound hexane, was determined using an online GC-FID system. The aerosol flow was sampled onto the capillary column (phase ZB-5, 30 m \times 0.32 mm I.D. and film thickness of 0.5 μ FT, phenomenex) using a six-port valve. Helium was used as carrier gas at a flow rate of 5.0 mL min⁻¹. The injection temperature and the FID detector temperature were 250°C and 300°C, respectively. The oven temperature was isothermally set at 50°C for the 5 min runs.

Using different OH exposure values calculated from the reference compound and the corresponding particle-bulk phase organic component(Org) losses, the k_{org} was be measured for each compound of interest. From the integration of the time dependent decay of organic component (Org)(synonymous with equation 2.2 for hexane), a relationship between particle losses of Org and OH exposure is established. The following equation shows the relationship

$$OH \text{ exposure} = -\frac{\ln\left(\frac{[Org]_t}{[Org]_0}\right)}{k_{org}} = \int_0^t [OH] dt = \langle OH \rangle_{t.t} \quad (2.4)$$

Where $[Org]_0$ is the initial concentration of Org before any OH radical are introduced, $[Org]_t$ is the concentration of Org after being exposed to OH radicals, and k_{org} is the second-order rate constant (cm³ molecule⁻¹ s⁻¹) for OH oxidation of organic compound (Org) in aerosol particles.

As the oxidation of the organic compound and the reference compound occurs simultaneously equation 2.3 can be substituted in equation 2.4 to give the following equation:

$$\ln \left(\frac{[Org]_t}{[Org]_0} \right) = k_{org} \left[\frac{\ln \left(\frac{[Hex]_t}{[Hex]_0} \right)}{k_{hex}} \right] \quad (2.5)$$

$$\left(\frac{[Org]_t}{[Org]_0} \right) = \exp (-k_{org} < OH >_t \cdot t) \quad (2.6)$$

The observed decay rate constant (k_{org}) for Org can be determine from an exponential fit by plotting $\frac{[Org]_t}{[Org]_0}$ versus $< OH >_t \cdot t$.

2.1.4 Reactive uptake measurement

The observed rate constant k_{org} described above can be used to describe the efficiency of the oxidation of particle-phase organic species. However, this value (k_{org}) is dependent on the experimental setup and the ambient conditions, therefore the obtained rate cannot be compared to other studies. A more useful term to describe the reaction efficiency in heterogeneous reaction is the reactive uptake coefficient, γ_{eff} . For this study the reactive uptake coefficient (γ_{eff}) was defined as a fraction of OH radical to particle collisions which successful cause the depletion of reactant molecule in the particle. The calculation for γ_{eff} done were all under the assumption that the particles that were reacted, were all spherical and well mixed. From the definition of γ_{eff} given above, the time dependent decay of particle phase organic species becomes:

$$\frac{d[Org]}{dt} = -\gamma_{eff} \cdot f \cdot J_{coll} \cdot C_p \cdot A \quad (2.7)$$

where f is the fraction of particle molecules remaining in the particle $\left(\frac{[Org]_t}{[Org]_0}\right)$ and depends on the extent of reaction. J_{coll} is the OH flux at the particle surface, C_p is the particle number density, and A is the particle surface. γ_{OH}^{Org} can be obtained by substituting $\frac{[Org]_t}{[Org]_0}$ for f , $-k_{org} \cdot [OH] \cdot [Org]$ for $\frac{d[Org]}{dt}$, and $\bar{c} \cdot \frac{[OH]}{4}$ for J_{coll} , to give:

$$\gamma_{OH}^{Org} = \frac{4 \cdot k_{org} \cdot [Org]_0}{\bar{c} \cdot A \cdot C_p} \quad (2.8)$$

Where \bar{c} is the mean speed of gas-phase OH, $[Org]_0$ is a spatially averaged concentration and can be expressed as:

$$[Org]_0 = \frac{C_p \cdot V \cdot \rho_0 \cdot N_A}{M} \quad (2.9)$$

Where V is the particle volume, M is the molar mass of particle species, N_A is the Avogadro's number, and ρ_0 is the initial particle-phase density. Given that $\frac{V}{A} = \frac{D_{surf}}{6}$ (D_{surf} is the mean surface weighted particle diameter of the aerosol distribution measured by the SMPS.), the final expression of γ_{OH}^{Org} is^{8,9}:

$$\gamma_{OH}^{Org} = \frac{4 \cdot k_{org} \cdot D_{surf} \cdot \rho_0 \cdot N_A}{6 \cdot \bar{c} \cdot M} \quad (2.10)$$

Interpretation of γ_{OH}^{Org} has been given in the introduction chapter, all values of γ_{OH}^{Org} were reported with an uncertainty $\delta\gamma_{OH}^{Org}$.

$$\frac{\delta\gamma_{OH}^{Org}}{|\gamma_{OH}^{Org}|} = \sqrt{\left(\frac{\delta k_{org}}{k_{org}}\right)^2 + \left(\frac{\delta D_{surf}}{D_{surf}}\right)^2} \quad (2.10b)$$

2.2 Molecular Dynamics Algorithms: (MD) Simulations setup

2.2.1 Periodic Boundary Conditions

Boundaries are set to contain fast diffusing molecules during simulation. The molecules should be contained in a set boundary to preserve thermodynamic properties such as temperature, pressure and density. Several types of boundary conditions can be applied.

Earlier simulation applied **vacuum** as a boundary conditions, however, the dynamics of the global system properties would fail to reproduce the condensed phase^{10,11}.

Fixed boundaries are by far the most simplistic approach to boundary conditions. Molecules making up the chemical system are encapsulated inside a box with a rigid, fixed wall that does not allow the passage of molecules. This wall is achieved by simply restraining some atoms in the simulation to form a closely packed layer of atoms that either completely reflect particles or interact with them through some potential energy function or force field. Another simpler way to setup such boundaries would be to ignore all boundary atoms and use a repulsive potential on the boundaries to make nearby atoms feel a strong but very short-range force in the direction of the center of the box. These potentials maybe in the form of the repulsive term of the Lennard-Jones potential. Such boundaries cause artifacts in the simulation as unwanted surface effects emerge when the components of the system react to the boundary condition.

Periodic boundary conditions are the most common way to avoid the unwanted surface effects that arise from fixed boundaries. In periodic boundary conditions each particle that reaches the edge of the simulation box reappears on the opposite side and continues to interact with nearby particles. It is as if the simulation box is surrounded by 26 (in three dimensions) translated copies of itself containing the same particles with identical properties compared to the original central system. Periodic boundary conditions thus yield a system with no surface molecules and

therefore no surface effects. For Periodic boundary conditions to work properly the system size needs to be large enough to avoid molecules interacting with their own image. The cutoff distance is not larger than half the distance of the shortest side of the periodic box, or otherwise an atom will interact with its image and cause erroneous simulations. On the downside periodic boundary conditions are a bottleneck for computer performance of molecular dynamics simulation programs, especially when system sizes become considerably larger. Periodic boundary conditions are also inappropriate for in-homogeneous or non-equilibrium systems.¹²

Adaptive boundary conditions are well suited to reduce the computational cost of simulations that utilize periodic boundary conditions. Adaptive boundary conditions make use of adaptive resolution to drive down computational cost, solvent molecules change resolution between atomistic and coarse-grained representations on the fly as they move between different regions in the simulation box. Three different spherical regions centered around the molecule of interest ranging from all atom resolution at the center to coarse-grained further away radially, are defined. A hybrid region lies in-between where the resolution smoothly transitions from atomistic to coarse-grained.^{13,14} Adaptive boundary models can achieve around a factor three speedup compared to atomistic simulations; however they remain computationally demanding because of the atomistic.

Stochastic boundary conditions have also been successfully used to avoid the PBC. In Stochastic boundary conditions a spherical system is divided radially into three different parts one termed the reaction region, the other buffer region, and the last being reservoir region. In the center reaction region, the present molecules submit to conventional molecular dynamics, while in the buffer region the molecules move according to Langevin dynamics and are thus subjected

to a thermal bath that serves as a thermal sink or source for the reaction region. In the outermost reservoir region molecules remain fixed.¹⁵⁻¹⁸

Other boundary models exist such as elastic boundary conditions¹⁹. For this study Periodic boundary conditions (PBC) were employed despite being more computationally expensive.

2.2.2 Thermostats and Barostats (Temperature and Pressure Control)

Temperature is kept constant in constant temperature simulation using a thermostats. The Langevin thermostat was used to keep the temperature constant in all simulations. The thermostat maintains the temperature around the target temperature by the addition of friction and random forces.²⁰⁻²²

To simulate the NPT ensemble, pressure was kept constant using the Nose-Hoover Langevin piston pressure control. This pressure control method couples well with the above stated temperature control method as both make use of Langevin dynamics. The Nose-Hoover Langevin piston is an amalgamation of the Nose-Hoover constant pressure method and the piston fluctuation control implemented using Langevin dynamics.^{23,24}

2.2.3 Ensembles

An ensemble can be defined as a collection of weighted microstates that have an identical macrostate. It can also be defined as a collection of different ideal states that the same system can be in, all considered at the sometime. Different types of ensemble exist in molecular dynamics simulation which include^{25,26};

1. Microcanonical Ensemble: total energy is conserved(E), the number of basic particles is conserved(N) and there is a boundary limit(V). The ensemble is also referred to as (NVE) ensemble.

2. Canonical Ensemble: system temperature is conserved (not absolutely constant); the number of basic particles is conserved and there is a boundary limit (V) or there is constant pressure(p). the ensemble is referred to as NVT or NPT ensemble.
3. Grand Canonical Ensemble: System temperature is conserved (not absolutely constant), The chemical potential of the particle reservoir is constant (μ), There is a boundary limit (V); or there is a constant pressure (P). The ensemble also called (GVT) ensemble or (GPT) ensemble

For the simulation done in this study all the forms of the conical ensemble was used, with NVT and NPT being applied at different stages of the simulation.

2.2.4 Langevin Dynamics

Langevin Dynamic was included in all simulations looked at in this study to enable the generation of ensembles at constant temperature, volume and/or pressure. The Langevin equation is a modified Newtonian equation with a friction term added:

$$m\ddot{r} = F(r) - m\gamma\dot{r} + \sqrt{\frac{2k_B T}{m}} R(t) \quad (2.11)$$

where m is the mass of a particle, \ddot{r} is the acceleration, $F(r)$ is the force, r is the position vector, γ is the friction coefficient, $v = \dot{r}$ is the velocity, k_B is the Boltzmann constant, T is the temperature, $R(t)$ is a univariate Gaussian random process.^{27,28} A friction coefficient of 1ps^{-1} was applied to all simulation in this study.

2.2.5 Initial Conditions

The initial coordinated and velocity of each atom in a simulation must be provided. For the studies presented here, the initial coordinates for atoms and structure of molecules was provided

from Protein Data Bank (PDB) files obtained from the Research Collaboratory for Structural Bioinformatics (RCSB) website. These structures are built based on information from various structural study experimental. The initial velocity for atoms was assigned randomly from the Maxwell-Boltzmann distribution:

$$P(v) = \sqrt{\left(\frac{m}{2\pi k_B T}\right)^3 4\pi} e^{-\frac{mv^2}{2k_B T}} \quad (2.12)$$

where m is the mass of the particle, v is the velocity, k_B is the Boltzmann constant, and T is the temperature.

2.2.6 Numerical Integration

Classical MD simulations are heavily dependent on the numerical integration of Newtons laws of motion. This makes the numerical integrator one of the most vital parts of MD simulations. Various integration algorithms have been designed to perform this task, each with its own advantages and disadvantages.^{29,30} For this study a variation of the Verlet algorithm, the r-RESPA method, was adopted and used. The method chosen is best for performing multiple timestep integration.^{31,32}

2.2.7 Integration Timestep

The timestep is a key element that affects the accuracy and convergence of MD simulations. The selection of timestep is literally a compromise between computational cost and accuracy. Small time steps increase accuracy while also simultaneously increasing the computational cost. On the other hand, large timesteps lead to increased sampling of the conformational space but causes system instability. The ideal timestep should be small enough to be comparable to the most rapid component of the motion.³³⁻³⁵ A time step of 1fs was used for all simulation done for this study.

2.2.8 Minimization

Minimization of MD simulation is done to remove any interactions (such as steric clashes between atoms) in the system that might lead to the numerical integrators becoming unstable when running dynamics. The NAMD default minimizer which makes use of the method of conjugate gradients was used for all simulations reported in this study. The conjugate gradient method has been shown to have better performance compared to other methods such as the velocity quenching method. Minimization was run until a convergence of the system and no bad contacts were found.

2.3 Inter-atomic Interactions and Force Fields

The potential energy surface of a system is described by a predefined potential function aided with parameters defined in parameter files. Potential functions are a system of equations used to approximate the interactions between the atoms, and the force acting on an atom is determined as the negative derivative of potential energy with respect to the position of the atom. The potential energy in a force field is decomposed into two parts, the bonded term and the non-bonded term. The bonded term consists of contributions coming from bonds, angles, dihedral angles and improper dihedral angles, while the non-bonded component describes contributions from van der Waals and electrostatic interactions. In cases where polarization has to be considered explicitly the force field expression is modified to include a polarization term.

2.3.1 Bonded Interaction

Atoms are considered for bonded interactions if the atoms are connected by 1 to 3 bonds. The bonds mechanics and angle bending are in most cases approximated by the harmonic functions with potential minimum at their reference bond length and angle

$$E_{b,ij} = \frac{1}{2}k_{b,ij}(r_{ij} - r_{ij,0})^2, E_{a,ijk} = \frac{1}{2}k_{a,ijk}(Q_{ijk} - Q_{ijk,0})^2 \quad (2.13)$$

In the event that the interaction of atoms participating in a bond need to be accounted for the Urey-Bradley potential function:

$$E_{UB,ijk} = \frac{1}{2}k_{UB,ijk}(r_{ik} - r_{ik,0})^2 \quad (2.14)$$

In the event of bond breaking down the anharmonicity is described by the Morse potential:

$$E_{Morse,ij} = D_{ij}[1 - \exp(-\beta_{ij}(r_{ij} - r_{ij,0}))]^2 \quad (2.15)$$

where the energy approaches D_{ij} as the distance r_{ij} becomes infinity. Dihedral angles which are periodic in character, determine the conformation of molecules. As part of the bonded interaction, they are described by the dihedral angle potential term which can be expressed as a sum of cosine functions

$$E_{d,ijkl} = \sum k_{d,ijkl} [1 + \cos(n\phi_{ijkl} - \phi_{ijkl,0})] \quad (2.16)$$

Or alternatively by the Fourier series. Improper dihedrals angles that arise from double bonds or aromatic rings are described by a harmonic potential function similar to bonds and angles.

$$E_{im,ijkl} = \frac{1}{2}k_{im,ijkl}(\varepsilon_{ijkl} - \varepsilon_{ijkl,0})^2 \quad (2.17)$$

2.3.2 Non-Bonded Interaction

In most standard simulations the total non-bonded potential is equivalent to the sum of each pairwise interaction. The non-bonded interaction potential between two atoms is a summation of the van der Waals and electrostatic terms. The electrostatic terms being modeled by the Coulomb potential between point charges, where the dipole, quadrupole and higher-order contributions are implicitly included in an average manner, since the effective pairwise potentials are parameterized to reproduce the experimental observations or the results from quantum chemical calculations. The van der Waals interaction being modeled by the Lennard-Jones potential:

$$E_{LJ,ij} = 4\varepsilon_{ij} \left[\left(\frac{\sigma_{ij}}{r_{ij}} \right)^{12} - \left(\frac{\sigma_{ij}}{r_{ij}} \right)^6 \right] \quad (2.18)$$

And the electrostatic interactions by the coulomb potential

$$E_{C,ij} = \frac{q_i q_j}{4\pi\varepsilon_0 r_{ij}} \quad (2.19)$$

Force field ignore the non-bonded interactions between atoms connected a single or double bond, as constraints and harmonic potential functions are considered fully capable of properly describing the bonds and angles. However, for atoms sharing a triple bond, the dihedral angle potential is usually coupled with a scaled 1-4 non-bonded interaction. This treatment is done to enhance the flexibility in the parameterization of the force field and the transferability of the optimized parameters.

Cutoffs are employed when evaluating non-bonded interactions to conform to the requirements of periodic boundary conditions and to reduce computational cost. The use of this cutoff then necessitates considering long-range corrections (LRC) for both Lennard-Jones and Coulomb potentials. Only the LRC to the second term ($-4\varepsilon\sigma^6/r^6$, dispersion term) needs to be evaluated for Lennard-Jones potentials.

$$\begin{aligned} E_{LJ,LRC} &= \frac{1}{2} N_\rho \int_{r_c}^{\infty} 4\pi r^2 \left(-\frac{4\varepsilon\sigma^6}{r^6} \right) dr \\ &= \frac{8\pi}{3} N_\rho \varepsilon \sigma^6 r_c^{-3} \quad (2.20) \end{aligned}$$

The proportionality of the coulombic potential to r_{ij}^{-1} make the evaluation of LRC interactions more difficult. The electrostatic interactions between the atoms in the simulation box and their translational periodic images must be considered explicitly to calculate the total Coulomb potential

$$E_{C,total} = \frac{1}{4\pi\epsilon_0} \frac{1}{2} \sum_n \sum_{ij^*} \frac{q_i q_j}{r_{ij,n}} \quad (2.21)$$

2.3.3 Polarization

Polarization and polarization effects are expected in any multiple-body interaction especially chemistry system loaded with different charge carrying atoms and molecules. The polarization effects are usually catered for in many force fields implicitly in the pair wise potentials.^{36,37} Such a treatment is what was adopted for all simulations in this study. For some cases this approach is inadequate, and the polarization effect must be considered explicitly.

2.3.4 Several Force Fields and Water Models

Several force fields are available and popular for use in MD simulations these include AMBER^{38,39}, CHARMM⁴⁰⁻⁴² and OPLS⁴³. These force fields adopt the same potential functions with minor variation. For instance, the CHARMM force field uses the Urey-Brandley term to account for the 1-3 interactions. AMBER force field have the 1-4 scaling factor set to 0.5 for the Lennard-Jones potential, and 0.8333 for the Coulomb potential, while the 1-4 scaling is not used in CHARMM (set to unity). The OPLS (optimized potentials for liquid simulations) force field uses empirically optimized partial atomic charges and electrically neutral subunits. In the OPLS force field, the 1-4 nonbonded scaling factor is 0.5 for both van der Waals and electrostatic interactions. For this study all simulations were done using the CHARMM force field.

Various models of the water molecule have been developed and used. The different model each correctly reproduce some experimental values of water properties, but non has managed to reproduce all properties. The three-site TIP3P water was used for all simulation as the water solvent.⁴⁴

2.4 Software Packages

2.4.1 MD Simulation Software

Nanoscale Molecular Dynamics (NAMD) was used to conduct all simulations presented in this study. NAMD was chosen because of its ability to run using multiple processors (high parallel efficiency), simulate large systems, and its versatility with regards to potential functions, parameters, and file formats.^{45,46} NAMD versions 2.12 and newer were accessed free and used.

Visual Molecular Dynamics (VMD) was used for simulation setup and for trajectory analysis. VMD was chosen because of its high compatibility with NAMD, extended library of plugins, ability to work with diverse structural data, ability to handle large data sets, and a friendly interface.⁴⁷

Packmol was used to create initial positions for molecules making up the different systems studied. Packmol was chosen for its ability to create various packing structures.⁴⁸

Lightweight Object-Oriented Structure Library (LOOS) was used for the analysis of molecular dynamics simulation. It offered a wide range of easy to use tools and already developed analysis procedures and codes, which made data analysis easier.⁴⁹

Reference

1. Kinney PD, Pui DYH, Mulholland GW, Bryner NP. Use of the electrostatic classification method to size 0.1 micrometer SRM particles - A feasibility study. *J Res Natl Inst Stand Technol.* 1991;96(2):147. doi:10.6028/jres.096.006
2. Sc-arm-tr- DOE. Scanning Mobility Particle Spectrometer Instrument Handbook. 2016;(February).
3. TSI. Series 3080 Electrostatic Classifiers: Operation and Service Manual. *TSI Inc.* 2009;Revision J(March):107.
4. Hearn JD, Smith GD. A mixed-phase relative rates technique for measuring aerosol reaction kinetics. *Geophys Res Lett.* 2006;33(17):3-7. doi:10.1029/2006GL026963
5. Liu C, Zhang P, Yang B, Wang Y, Shu J. Kinetic studies of heterogeneous reactions of polycyclic aromatic hydrocarbon aerosols with NO₃ radicals. *Environ Sci Technol.* 2012;46(14):7575-7580. doi:10.1021/es301403d
6. Atkinson R. and Physics Kinetics of the gas-phase reactions of OH radicals with alkanes and cycloalkanes. Published online 2003:2233-2307.
7. Atkinson R, Baulch DL, Cox RA, et al. and Physics Evaluated kinetic and photochemical data for atmospheric chemistry : Volume I – gas phase reactions of O_x , HO_x , NO_x and SO_x species. 2004;l:1461-1738.
8. Smith JD, Kroll JH, Cappa CD, et al. The heterogeneous reaction of hydroxyl radicals with sub-micron squalane particles: A model system for understanding the oxidative aging of

- ambient aerosols. *Atmos Chem Phys*. 2009;9(9):3209-3222. doi:10.5194/acp-9-3209-2009
9. Li M, Su H, Li G, Ma N, Pöschl U, Cheng Y. Relative importance of gas uptake on aerosol and ground surfaces characterized by equivalent uptake coefficients. *Atmos Chem Phys*. 2019;19(16):10981-11011. doi:10.5194/acp-19-10981-2019
 10. van Gunsteren WF, Hünenberger PH, Mark AE, Smith PE, Tironi IG. Computer simulation of protein motion. *Comput Phys Commun*. 1995;91:305-319.
 11. Levitt M, Warshel A. Computer simulation of protein folding. *Nature*. 1975;253(5494):694-698. doi:10.1038/253694a0
 12. Barclay PL, Zhang DZ. Periodic boundary conditions for arbitrary deformations in molecular dynamics simulations. *J Comput Phys*. 2021;435:110238. doi:<https://doi.org/10.1016/j.jcp.2021.110238>
 13. Fritsch S, Junghans C, Kremer K. Structure formation of toluene around C60: Implementation of the adaptive resolution scheme (AdResS) into GROMACS. *J Chem Theory Comput*. 2012;8(2):398-403. doi:10.1021/ct200706f
 14. Praprotnik M, Delle Site L, Kremer K. Adaptive resolution molecular-dynamics simulation: changing the degrees of freedom on the fly. *J Chem Phys*. 2005;123(22):224106. doi:10.1063/1.2132286
 15. Berkowitz M, McCammon JA. Molecular dynamics with stochastic boundary conditions. *Chem Phys Lett*. 1982;90(3):215-217. doi:[https://doi.org/10.1016/0009-2614\(82\)80028-6](https://doi.org/10.1016/0009-2614(82)80028-6)

16. Nelson MT, Humphrey W, Gurov A, et al. NAMD: a Parallel, Object-Oriented Molecular Dynamics Program. *Int J Supercomput Appl High Perform Comput*. 1996;10(4):251-268. doi:10.1177/109434209601000401
17. Brunger AT, Brooks CL, Karplus M. Stochastic boundary conditions for molecular dynamics simulations of ST2 water. *Chem Phys Lett*. 1984;105:495-500.
18. Prusty M, Leaw JN, Chong SS, Cheong SA. Stochastic boundary conditions for grand-canonical-like molecular dynamics simulations of open systems. *Comput Phys Commun*. 2012;183(3):486-496. doi:10.1016/j.cpc.2011.11.004
19. Li Y, Krilov G, Berne BJ. Elastic bag model for molecular dynamics simulations of solvated systems: Application to liquid water and solvated peptides. *J Phys Chem B*. 2006;110(26):13256-13263. doi:10.1021/jp057532s
20. Farago O. Langevin thermostat for robust configurational and kinetic sampling. *Phys A Stat Mech its Appl*. 2019;534:122210. doi:https://doi.org/10.1016/j.physa.2019.122210
21. Leimkuhler B, Noorizadeh E, Theil F. A Gentle Stochastic Thermostat for Molecular Dynamics. *J Stat Phys*. 2009;135(2):261-277. doi:10.1007/s10955-009-9734-0
22. Davidchack RL, Handel R, Tretyakov M V. Langevin thermostat for rigid body dynamics. *J Chem Phys*. 2009;130(23). doi:10.1063/1.3149788
23. Feller SE, Zhang Y, Pastor RW, Brooks BR. Constant pressure molecular dynamics simulation: The Langevin piston method. *J Chem Phys*. 1995;103(11):4613-4621. doi:10.1063/1.470648

24. Martyna GJ, Tobias DJ, Klein ML. Constant pressure molecular dynamics algorithms. *J Chem Phys.* 1994;101(5):4177-4189. doi:10.1063/1.467468

25. Shell 1978- MS (Michael S. *Thermodynamics and Statistical Mechanics : An Integrated Approach LK* - <https://libwvu.on.worldcat.org/oclc/879627747>. Cambridge University Press; 2015.

26. Silakari O, Singh PK. Chapter 7 - Molecular dynamic simulations: Technique to analyze real-time interactions of drug-receptor complexes. In: Silakari O, Singh PKBTC and EP of M and I in DD, eds. Academic Press; 2021:157-178. doi:<https://doi.org/10.1016/B978-0-12-820546-4.00007-6>

27. Loncharich RJ, Brooks BR, Pastor RW. Langevin dynamics of peptides: The frictional dependence of isomerization rates of N-acetylalanine-N'-methylamide. *Biopolymers.* 1992;32(5):523-535. doi:<https://doi.org/10.1002/bip.360320508>

28. Izaguirre JA, Catarella DP, Wozniak JM, Skeel RD. Langevin stabilization of molecular dynamics. *J Chem Phys.* 2001;114(5):2090-2098. doi:10.1063/1.1332996

29. Frenkel D, Smit B. Understanding molecular simulation. From algorithms to applications (2002, Academic Press). Published online 2002:658.
[https://www.eng.uc.edu/~beaucag/Classes/AdvancedMaterialsThermodynamics/Books/%5BComputational science \(San Diego, Calif.\)%5D Daan Frenkel_ Berend Smit - Understanding molecular simulation _ from algorithms to applications \(2002, Academic Press \) - libgen](https://www.eng.uc.edu/~beaucag/Classes/AdvancedMaterialsThermodynamics/Books/%5BComputational%20science%20(San%20Diego,%20Calif.)%5D%20Daan%20Frenkel%20Berend%20Smit%20Understanding%20molecular%20simulation%20from%20algorithms%20to%20applications%20(2002,%20Academic%20Press)%20libgen)

30. Leimkuhler BJ, Reich S, Skeel RD. Integration Methods for Molecular Dynamics BT - Mathematical Approaches to Biomolecular Structure and Dynamics. In: Mesirov JP, Schulten K, Sumners DW, eds. Springer New York; 1996:161-185. doi:10.1007/978-1-4612-4066-2_10
31. Masella M. The multiple time step r-RESPA procedure and polarizable potentials based on induced dipole moments. *Mol Phys*. 2006;104(3):415-428. doi:10.1080/00268970500404414
32. Izaguirre JA, Ma Q, Matthey T, et al. Overcoming Instabilities in Verlet-l/r-RESPA with the Mollified Impulse Method BT - Computational Methods for Macromolecules: Challenges and Applications. In: Schlick T, Gan HH, eds. Springer Berlin Heidelberg; 2002:146-174.
33. Schlick T, Barth E, Mandziuk M. Biomolecular dynamics at long timesteps: Bridging the timescale gap between simulation and experimentation. *Annu Rev Biophys Biomol Struct*. 1997;26:181-222. doi:10.1146/annurev.biophys.26.1.181
34. Kim S. Issues on the choice of a proper time step in molecular dynamics. *Phys Procedia*. 2014;53:60-62. doi:10.1016/j.phpro.2014.06.027
35. Shuaib F, Kimbrough D, Roofe M, McGwin Jr G, Jolly P. 基因的改变 NIH Public Access. *Bone*. 2008;23(1):1-7. doi:10.1021/ct400331r.Long
36. Klesse G, Klesse G, Rao S, Tucker SJ, Tucker SJ, Sansom MSP. Induced Polarization in Molecular Dynamics Simulations of the 5-HT₃ Receptor Channel. *J Am Chem Soc*. 2020;142(20):9415-9427. doi:10.1021/jacs.0c02394

37. Lemkul JA. Pairwise-additive and polarizable atomistic force fields for molecular dynamics simulations of proteins. *Prog Mol Biol Transl Sci.* 2020;170:1-71.
doi:10.1016/bs.pmbts.2019.12.009
38. Darian E, Gannett PM. Application of molecular dynamics simulations to spin-labeled oligonucleotides. *J Biomol Struct Dyn.* 2005;22(5):579-593.
doi:10.1080/07391102.2005.10507028
39. Duan Y, Wu C, Chowdhury S, et al. A point-charge force field for molecular mechanics simulations of proteins based on condensed-phase quantum mechanical calculations. *J Comput Chem.* 2003;24(16):1999-2012. doi:<https://doi.org/10.1002/jcc.10349>
40. MacKerell AD, Bashford D, Bellott M, et al. All-atom empirical potential for molecular modeling and dynamics studies of proteins. *J Phys Chem B.* 1998;102(18):3586-3616.
doi:10.1021/jp973084f
41. MacKerell ADJ, Banavali N, Foloppe N. Development and current status of the CHARMM force field for nucleic acids. *Biopolymers.* 56(4):257-265. doi:10.1002/1097-0282(2000)56:4<257::AID-BIP10029>3.0.CO;2-W
42. Pastor RW, MacKerell AD. Development of the CHARMM force field for lipids. *J Phys Chem Lett.* 2011;2(13):1526-1532. doi:10.1021/jz200167q
43. Jorgensen WL, Maxwell DS, Tirado-Rives J. Development and testing of the OPLS all-atom force field on conformational energetics and properties of organic liquids. *J Am Chem Soc.* 1996;118(45):11225-11236. doi:10.1021/ja9621760

44. Mark P, Nilsson L. Structure and dynamics of the TIP3P, SPC, and SPC/E water models at 298 K. *J Phys Chem A*. 2001;105(43):9954-9960. doi:10.1021/jp003020w
45. Phillips JC, Braun R, Wang W, et al. Scalable molecular dynamics with NAMD. *J Comput Chem*. 2005;26(16):1781-1802. doi:10.1002/jcc.20289
46. Phillips JC, Hardy DJ, Maia JDC, et al. Scalable molecular dynamics on CPU and GPU architectures with NAMD. *J Chem Phys*. 2020;153(4). doi:10.1063/5.0014475
47. Humphrey W, Dalke A, Schulten K. Sartorius products. *J Mol Graph*. 1996;14(October 1995):33-38. <https://www.tapbiosystems.com/tap/products/index.htm>
48. Martínez L, Andrade R, Birgin EG, Martínez JM. Software News and Update Packmol : A Package for Building Initial Configurations. Published online 2009. doi:10.1002/jcc
49. Tod D. Romo, Nicholas Leioatts AG. building Tools to Analyze Molecular Dynamics Simulations. *J Comput Chem*. 2014;35(32):2305-2318. doi:10.1002/jcc.23753.Lightweight

3 A molecular dynamic study of the effects of partitioning on the OH radical interactions with solutes in multicomponent aqueous aerosols

3.1 Introduction

Aqueous aerosols are known to control cloud nucleation¹⁻⁴ and to affect the climate, air quality, and human health.⁵⁻⁸ A complete understanding of their role in atmospheric phenomena remains challenging as the properties of nanometric aqueous particles differ greatly from those of a bulk solution.⁹⁻¹³ The chemical evolution of atmospheric aerosols as well as their ability to initiate cloud formation is mostly controlled by the properties of the gas–water interface.^{2,14} Phenomena such as micro-confinement,¹¹ high surface electric field,¹⁵ preferred molecular orientation,^{12,14,16,17} and lower water densities at the interface^{18,19} affect reaction rates^{10,20} and photochemical processes,¹² thus enhancing certain reaction channels, while suppressing others.²¹⁻²⁴ Because atmospheric aerosols contain a wide range of solutes, it has become important to improve our understanding of how chemical composition changes surface reactivity.²⁵

The presence of several organic compounds in aqueous aerosols results in the formation of coexisting liquid phases within the same aerosol.²⁶⁻³⁰ In the case of water-miscible organic solutes, the core of the liquid particle, hereafter referred to as the particle bulk, acts as an infinite chemical reservoir for the outer phase. When diffusion is not the rate limiting step, thermodynamic equilibrium is reached and the composition of the air–water interface is governed by the surface–bulk partitioning properties of the solutes.^{13,31,32} Surfactants with long alkyl chains have been detected in atmospheric aerosols and are known to accumulate at the surface.^{3,33,34} Smaller, more hydrophilic molecules also display surface–bulk partitioning leading to a solute concentration gradient close to the air–water interface.¹³ Surface active molecule moves to the interface, decreasing the surface tension,^{35,36} while surface inactive molecules are excluded from it, leading to an increase of the surface tension.³² Surface tension changes in atmospheric aerosols affect natural processes, especially cloud nucleation.^{37,38} A molecular-level understanding of the

properties of the interface is required to fully understand the fundamental processes governing the chemical evolution of aerosols.

Surfactants at the air–water interface orient themselves with the hydrophobic chain toward the gas-phase, thus forming an outer molecular layer at high concentrations.³⁶ Preferred molecular orientation near the air–water interface is also observed using surface-specific electronic sum frequency scattering (SFS) for smaller organic solutes such as alcohols,³⁹ hexafluoro-2-propanol,⁴⁰ and more recently for malachite green and propionic acid.^{16,41} Molecular orientation is known to have an effect on photochemical activity^{42,43} and is also likely to affect reactivity by making certain organic functional groups more or less available to surface reactive species. Although the orientation of molecules at the air–water surface may appear to be intuitive, the extent of the molecular alignment, the size of the interfacial area, and its effect on reactivity remains mostly unquantified.

Solvation is also known to affect and modulate reactivity of organic solutes and radicals.⁴⁴⁻⁴⁷ For example, the photodissociation of phenol in water has been shown to be 10^4 faster at the water surface than in the bulk.¹⁸ Recent MD simulations coupled to quantum calculations showed that the interfacial process is accelerated due to a lower dissociation barrier from incomplete hydrogen bonding to phenol at the air–water interface.¹⁹ Water is also shown to stabilize the transition state for abstraction of a hydrogen atom from a solute leading to faster reaction compared to non-polar solvents.⁴⁶ Interfacial solvation and molecular orientations are difficult to probe experimentally, especially because SFS techniques remain insensitive to molecules with lower surface density and higher orientational disorder.³⁹ Classical and ab initio molecular dynamics (MD) methods are therefore vital to gain the required molecular-level understanding of the surface properties.

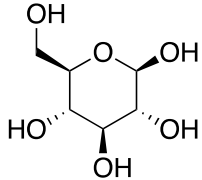
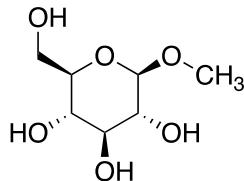
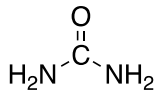
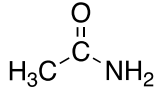
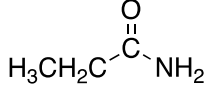
MD studies have shown that surface-adsorbed brominated halomethane are preferentially oriented with the carbon atom adsorbed on the water surface.⁴⁸ For halocarbons with longer nonpolar hydrocarbon chains such as butyl and pentyl chloride/bromide, the alkyl chain is predicted to be pointing toward the gas phase.⁴⁹ More recently, ab initio quantum-mechanical molecular dynamic simulations (QM/MM) have been performed to probe molecules at the air–water interface of aerosols.^{12,14} Martins-Costa et al.¹² investigated the electronic states and intersystem crossing processes of the photosensitizer imidazole-2-carboxaldehyde. The molecules are found to orient at the water surface and to have different absorption cross sections and spin orbit constants within the interface than in the bulk. Such studies highlight the strength of MD simulations for investigating interfaces as well as for explaining observed aerosol-specific chemical reactivity.¹⁴ In the atmosphere, the OH radical is one of the most abundant oxidizer.⁵⁰ MD simulations have shown that the radical adsorbs at the water surface and partitions between the bulk and the surface with an enhanced surface concentration.⁵¹⁻⁵⁶ The preference of the OH radical for the air–water interface can be compared to the radical predicted diffusion–reaction length ($\sim 1\text{--}2\text{ nm}$)⁵⁷⁻⁶⁰ under reactive conditions. Both suggest that the initiation step of the heterogeneous oxidation predominantly takes place within the interface. Several studies have also looked at the solvation of the OH radical.^{46,47,61-67} A different solvation of the radical and solute near the interface could explain enhanced surface rate coefficients²⁴ and changes in oxidative chemical scheme. Overall, the reaction within the air–water interface will be governed by an interplay of the solute concentration gradients, the reactant solvation, and the molecular orientations. For all these reasons, surface active molecules are more likely to react with the OH radical while surface inactive molecules may be shielded from oxidation. A better understanding of the chemical

evolution of multicomponent aqueous aerosols under atmospheric conditions therefore requires a systematic study of the behavior of a wide range of molecules within the air–water interface.

Atmospheric aerosols contain a wide range of solutes with different organic functional groups. In multicomponent particles, even though the solutes are dilute enough to neglect intermolecular interactions, concentration gradients near the surface lead to solute reactive uptake coefficients that are different from those observed in a single component particle.³¹ A better understanding of the effect of composition on the chemical fate of aerosols under oxidative conditions therefore requires a systematic investigation of the effect of the organic functional groups on heterogeneous reactivity. Amides and saccharides are good archetypal molecules for investigating such effects as they display a very wide range of partitioning properties. Table 3.1 displays the chemical structure of a series of amides and saccharides. When available, it also displays the partition coefficient K_p .^{13,32} A value lower than unity is characteristic of a surface inactive molecule with a preference for the water bulk. The concentration of the solute near the water surface is quasi-null for K_p close to 0,^{13,32} and increases as K_p increases. Glucose, Methyl β -D-glucopyranoside (MGP), and urea are considered as surface inactive, while acetamide and propionamide are surface active. The solvation of amides has been extensively studied both experimentally by means of various spectroscopic techniques^{8,68-82} and theoretically by Monte Carlo simulations^{83,84} and MD methods.⁸⁵⁻⁹³ The hydrophobic and hydrophilic nature of amides influences the amide–water interaction and the properties of the water solvation shells around the molecule. Similarly, there is a large number of studies on the solvation of saccharides showing their preference for the water phase.⁹⁴⁻¹⁰⁰ Although sugars are not expected partition toward the surface, they are found to have an enhanced reactivity toward phosphorylation at the air–water

interface of microdroplets.¹⁷ A more systematic investigation of organic solute surface partitioning is therefore required.

Table 3.1 Name, structure, and partition coefficient for the organic solutes used in the MD studies

Molecule	Chemical structure	K_p^{32}
b-D-glucose		0.2
Methyl b-D-glucopyranoside		
Urea		0.8
Acetamide		3.7
Propionamide		

In this study, classical MD is used to investigate the effect of the structure of small organic solutes (see Table 3.1) on surface concentration gradients, molecular orientation, and solvation, as well as their effect on the OH–solute interaction near the surface. The interface of aqueous particles is simulated using a 80-Å cubic water box surrounded by OH radicals in the gas phase. Although the model is oversimplistic and does not include reactive interactions it still provides molecular-level information about the solutes’ surface properties and radical–solute interactions. The size of the simulation box allows for the comparison of the solute behaviors between the bulk and the interface as well as the sizing of the interfacial region. Surface active molecules are found to migrate to the interface and to systematically orient with the alkyl group pointing

toward the water surface. The molecules regain full rotational freedom 2 nm away from the surface. The structure of the solvation sphere is also found to change considerably at the interface. Glucose and urea are confined to the bulk with no preferred orientation. MGP is found to be amphipathic with low surface concentration but still adopting a preferred orientation near the surface. The concentration gradient, the molecular orientation, and the reduced solvation near the surface all suggest an enhanced reactivity of surface-active molecules. The computational study establishes trends to better understand the different reactivity observed in multicomponent aqueous particles. The results are used to discuss the OH-initiated oxidation of particles containing several solutes with different partitioning properties.

3.2 Methods

3.2.1 Molecular dynamic

The air–particle interface was modeled using a $80 \times 80 \times 80 \text{ \AA}^3$ simulation box filled with 13,000 water molecules and 240 organic molecules. The water box was surrounded on both sides along the z -axis by 80-\AA vacuum boxes filled with a total of 40 OH radicals (see Figure 3.1), resulting in an overall $80 \times 80 \times 240 \text{ \AA}^3$ system.^{101,102} Vacuum was used instead of air as the number of nitrogen and oxygen molecules would be negligible within the considered volume.¹⁰¹ This volume is hereafter referred to as air. The 240 organic molecules in the water box were either made-up of urea, glucose, methyl β -D-glucopyranoside (MGP), propionamide, or acetamide. Solute mixtures were also investigated using an equal number of either, urea and MGP, propionamide and acetamide, or acetamide and MGP. Water was modeled with the rigid three-charge three-site TIP3P model including Lennard-Jones interaction on all atoms.^{103,104} The OH radical model was based on previous models available in the literature.⁵¹ The OH radical permanent dipole was modeled using a $-0.32e$ partial charge on the oxygen atom and a $+0.32e$

partial charge on the hydrogen, with e the elementary charge. The O–H bond length was set to 0.97 Å and the bond energy to 545 kcal mol⁻¹ Å⁻². The Lennard-jones parameters on the atoms were adopted from the hydroxide ion model.^{51,105} The urea, propionamide, and acetamide geometry and interaction parameters were taken from the CHARMM 36 force field. In the case of MGP these parameters were adopted from D-glucose with methyl patch parameters from the CHARMM 36 force field.^{106,107} Nonbonding forces used a cutoff of 12 Å, and electrostatic interactions were modeled using the Particle Mesh Ewald method.^{108,109} All simulations were performed using the NAMD 2 package v. 2.14.¹¹⁰

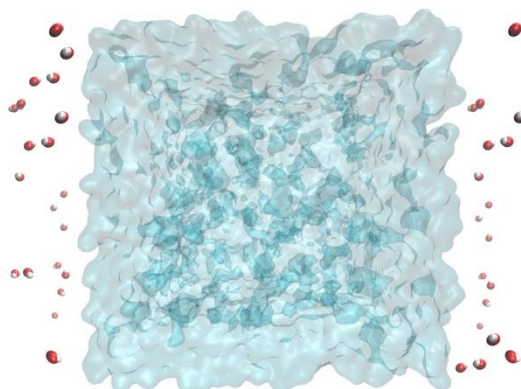


Figure 3.1 Initial water-box configuration of the constant NVT simulation cell.

The organic molecules were randomly placed in the simulation box using PACKMOL¹¹¹ followed by the OH radicals on either side of the box periodic boundary conditions. The water molecules were added last to the simulation box using the VMD program solvation plugin.¹¹² The concentration of each organic molecule in the water solvent is 0.111 mol L⁻¹. A constant NPT (constant number of particles, pressure, and temperature) preliminary run with 5,000 minimization steps was run first with a 1-fs time step. The pressure and temperature were kept constant at 1 atm and 298 K, respectively using a Langevin barostat and thermostat with the damping coefficient set to 1/ps.¹¹³

During this initial simulation, the hydroxide radicals were held in fixed positions using fixed atom parameters.

The initial production run outcome from the NPT ensemble was used as the starting point for the final NVT ensemble (constant number of particles, volume, and temperature). A constant-NVT equilibration run was performed for 5 ns, followed by a 110 ns constant-NVT production run, all with a time step of 1 fs. The constraints on the OH radicals from the initial production run were removed, and lateral pressure calculation parameters added to enable the calculation of surface tension.^{101,114} Five independent production runs with different organic molecule initial coordinates were performed to account for the effect of starting conformations on the final simulation results. The data displayed below are from a single production run and are representative of the outcomes of all 5 independent runs.

3.2.2 Data analysis

Density profiles ρ of a species along the z -axis were determined using the density profile tool in the VMD program.¹¹⁵ The modeled volume was divided into equally sized slabs along the z axis of thickness Dz . The density profile of a property p_i for an atom indexed i was calculated using Eq. 3.1:

$$\rho_n = (L_x L_y \Delta z)^{-1} \sum_{atom\ i} \delta_n(z_i) p_i \quad \text{Eq. (3.1)}$$

where n is the slab integer, L_x and L_y are the sides of the periodic cell, and $\delta_n(z_i)$ is the indicator function which is unity if the coordinate z_i is within the slab volume and zero otherwise.¹¹⁵

Radial pair distribution functions (RDF) $g(r)$ were calculated using the RDF tool in VMD.

The tool calculates the spherical atomic radial distribution function $g(r)$ between the coordinates of two selected atoms over a given trajectory. The RDF calculations are performed within the

full simulation box as well as within the liquid bulk center and the interfacial regions.¹¹⁶ RDFs for each atom and molecule pair are histogrammed into 240 bins from a distance 0 Å to 24 Å (twice the maximum force cut off distance). The RDFs between different atom pairs and molecule pairs give a depiction of molecular arrangements and microstructure in the different regions of our simulation.

Surface tension values γ were calculated using the mechanical definition of the atomic pressure. Surface tension is defined in terms of the difference between the normal (z -direction) and lateral components of the pressure tensor. For this study in which a simulation cell of length $L_Z (=3L)$ contains two surfaces, γ can be expressed using Eq. 3.2:

$$\gamma = \frac{1}{2} \int_0^{L_Z} [P_{ZZ} - 0.5(P_{XX} + P_{YY})] dz \quad \text{Eq. (3.2)}$$

where P_{XX} , P_{YY} , and P_{ZZ} are the three diagonal components of the pressure tensor along the x -, y -, and z -direction, respectively.¹⁰¹

3.3 Model validation

The validity of the model to predict the behavior of organic molecules at the air–water interface was verified by calculating self-diffusion coefficients and bulk water density, examining water and OH radial density functions, as well as by examining trends in calculated surface tensions.

The self-diffusion coefficient D of water and glucose were estimated from mean square displacement (MSD) using the Einstein's relation:¹¹⁷

$$D = \lim_{t \rightarrow \infty} \frac{\langle [r(t) - r(0)]^2 \rangle}{6t} \quad \text{Eq. (3.3)}$$

where t is time, and $[r(t) - r(0)]^2$ is the mean square displacement.¹¹⁸ The bulk density ρ of water is calculated using the following relation:

$$\langle \rho \rangle = \frac{M n_{res}}{N_{avo} \langle V \rangle} \quad Eq. (3.4)$$

were M is molar mass of water, N_{avo} is the Avogadro number, n_{res} is number of water residue in the box of interest, and $\langle V \rangle$ is the average simulation box volume.¹¹⁹

Table 3.2 displays calculated and measured diffusion coefficient and water densities from the present study and previous studies on aqueous systems. The self-diffusion coefficient and water density from the present study compares well to literature values from TIP3P water model.

Table 3. 2 Comparison of different water properties determined experimentally and theoretically using the TIP3 water model.

Model	T (K)	D($10^{-9} \text{ m}^2 \text{ s}^{-1}$)	ρ (g cm^{-3})	N ^b
TIP3P ^a	298	4.91(0.21)	0.998	13676
TIP3P ¹²⁰	301(4.4)	5.40(0.14)	1.001	820
TIP3P ¹²¹	297.0(0.9)	5.60(0.08)	0.998	901
TIP3P ¹²²	298.15	5.19(0.08)	0.993	267
TIP3P ¹²³	298.16	5.30	0.986	216
TIP3P ¹²⁴	298	5.51		360
TIP3P ¹²⁵	298	2.98		624
TIP3P ¹²⁶	298.15	6.10	0.9986	2048
TIP3P ¹²⁷	298.15	5.06		256
TIP3P ¹²⁸	298.15	6.14	1.008	2100
TIP3P ¹²⁹	298.15	5.50	0.98	
Exp		2.30 ¹³⁰	0.997 ¹³¹	

^apresent study

^bnumber of water molecules used in simulation N

The water distribution functions, $g_{OO}(r)$, $g_{OH}(r)$, and $g_{HH}(r)$ were calculated and compared to literature data on similar systems (Table 3.3). The results from this study compare reasonably well to other simulations and experimental results. The RDF between oxygen–oxygen pairs of two water molecules (Figure A1) is similar to literature profiles¹⁰¹ and shows a sharp peak at 2.75 Å (Table 3.3) for all three simulation setups. This value is close to the expected average hydrogen bond length in water, 2.8 Å.¹³² In addition, all RDFs between two identical species (not

showed) are found to be independent on the particle composition as expected for such dilute systems.

Table 3.3 Comparison of Oxygen-Oxygen and Oxygen-Hydrogen pair distribution functional determined experimentally and theoretical using the TIP3P water model.

	First max position		Second max position		Third max position	
	Å	g _{oo}	Å	g _{oo}	Å	g _{oo}
Oxygen-Oxygen						
TIP3P ^a	2.75	2.68	4.55	1.00	6.85	1.02
TIP3P ¹²¹	2.77	2.67	4.50	0.99	6.84	1.02
Exp ¹³³	2.88	3.09	4.50	1.14	6.73	1.07
Oxygen-Hydrogen						
TIP3P ^a	1.85	1.27	3.25	1.44		
TIP3P ¹²¹	1.83	1.24	3.22	1.44		
Exp ¹³³	1.85	1.38	3.30	1.60		

^apresent study

The RDFs of water atoms around the OH radical in the system were calculated and compared to literature profiles. Table 3.4 displays the main peak positions for the different atoms. The present simulations are in good agreement with Campo and Grigera¹³⁴.

Table 3.4 First and second peak position of water-OH DRFs.

RDF	First peak		Second peak	
	Present study	Campo and Grigera ¹³⁴	Present study	Campo and Grigera ¹³⁴
H*H	2.45	2.4	4.45	4.30
H*O	1.75	1.75	3.75	3.75
O*H	2.05	1.97	3.35	3.35
O*O	2.85	2.85	-	6.90

The surface tension of pure water is calculated to be 75.3 mN/m, 5% higher than the experimental value.¹⁰¹ Although MD has been extensively used to model the air–water interface,¹⁰¹ calculated surface-tension values varies considerably even for studies using the same water model. The discrepancy is due to different simulation parameters and even simulation times.¹⁰¹ The goal of the surface tension calculations performed here is to examine the relative

change in value due to the addition of solutes. Table 3.5 shows the simulated values of surface tension obtained for different solutes and solute mixtures. As solutes are added to the water system the calculated surface tension decreases. Amides are known to greatly reduce the air–water surface tension^{32,135} with an expected increasing effect as the alkyl chain length increases. Urea has been measured to increase the water surface tension, although the effect is expected to be negligible at the solute concentrations used in the simulations.^{32,136} The very small decrease of surface tension after addition of urea observed in Table 3.5 compared to pure water is likely to be an artefact of the modeling. Similarly, the addition of sugars to water, at low solute concentrations, is expected to lead to a negligible change.¹³⁷ The presence of a methyl group in MGP however, is likely to reduce its hydrophilicity compared to glucose and to induce a measurable decrease of the surface tension. Overall, as seen in Table 3.5, the addition of an alkyl group to the solute consistently decreases the air–water surface tension.

Table 3. 5 Simulated surface tension values

Solutes	Surface Tension (mN/m)	Solutes^(a)	Surface Tension (mN/m)
Urea	71.5	MGP and urea	66.5
MGP	67.9	MGP and acetamide	63.4
Acetamide	67.5	Propionamide and acetamide	56.6
Propionamide	58.5		

(a)Including OH radicals

Figure 3.2 displays the OH radical profiles for the 3 different mixtures. The origin of the z -axis is located 40 Å before the center of mass of the water box and is defined as the water surface. For all simulations, OH radicals maintain similar density distributions regardless of the combination of molecules making up the multi-component system. The OH density profiles show an increase in density from a constant value in the gas phase (with less than 5% fluctuation) to maxima near

the water surface, followed by a sharp drop and a constant value within the water bulk. The density profile is characteristic of the radical preference for the air-water interface. During the last 50 ns of the simulation, one OH radical spends an average of 45% of the simulation time within the first 10 Å below the surface, 24% in the gas phase, and the remaining 31% in the bulk. Hydroxyl radicals being predominantly located at the interfacial regions agrees with the findings of Roeselová et al.⁵¹ as well as with the potentials of mean force (PMF) calculations by Vácha and Slavíček⁵² showing active uptake of OH radicals at the interface.

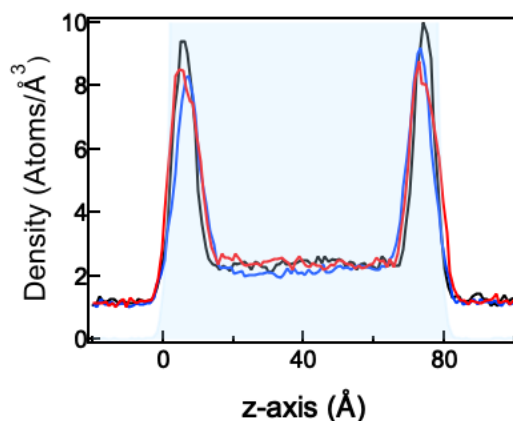


Figure 3.2 OH radical density profiles for a MGP–urea mixture (black line), (b) acetamide–propionamide (blue line), and (c) acetamide–MGP (red line) across the water-box (blue shaded area).

Figure 3.3 displays the scattering plot of one OH radical (black dots) within the last 7 ns of the simulation. It shows occurrences of adsorption (green), desorption (red), absorption (purple) and transfer from the bulk to the interface (dark blue). In the absence of reactions, the radicals are at a dynamic equilibrium between the different phases of the system. These results are consistent with previous MD simulations of OH interaction at the air–water interface,^{51,138} although performed here over a much longer simulation time.

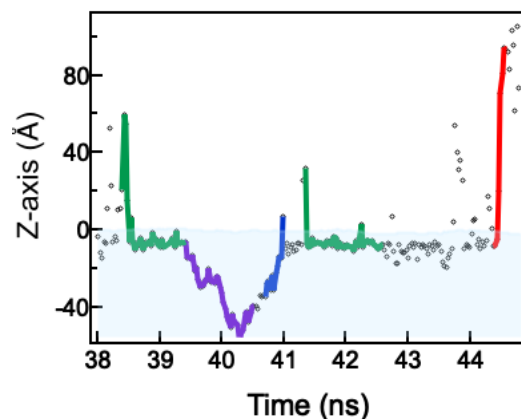


Figure 3.3 Scattering plot of one OH radical (black dots) within the last 7 ns of the simulation. Different trajectories of the radical are highlighted, gas-surface adsorption (green), desorption (red), absorption (purple), and bulk-to-interface transfer (dark blue). The blue shaded area is the water box.

3.4 Results and Discussion

3.4.1 Organic solute density profiles

Figure 3.4 displays density profiles of (a) MGP and urea, (b) acetamide and propionamide, and (c) MGP and acetamide along the z -axis of the simulation box. The water box is represented by the blue shaded area. The quasi-null water-molecule density outside the 0–80 Å range indicates negligible evaporation and therefore the stability of the simulation water box. All organic molecules are found to be confined to the water box. The air–water interface (purple region) extends 10 Å into the water box and 10 Å into the gas phase. The interface may also be defined as the region where the water density is between 10% and 90% of its bulk value.¹³⁸ Because no molecules were found in the gas phase, the two definitions lead to similar results. In Figure 3.4a, the density profiles of the two organic species (urea and MGP) show an increase from zero at the liquid surface to respective maxima within the water bulk or within the air–water interface. In the bulk phase, the density fluctuations are less than 20% from the maximum value. In the case of urea, the lack of a maxima within the interface area and near-flat density profile in the bulk

indicate that the organic species has a higher preference for the liquid bulk. The MGP density profiles (Figure 3.4a and Figure 3.4c) display a sharper density rise than that of urea in the interfacial area, although most of the molecules remain located within the bulk. The affinity of an organic molecule for a given region may be quantified by integrating the density profile over the corresponding z -range. For reference, the water volume within the interface represents 25% of the total water box. The integrated profile values are given in Table 3.6. With a relative bulk value of 89% for urea and 84% for MGP, MGP has a slightly higher affinity for the interface than urea.

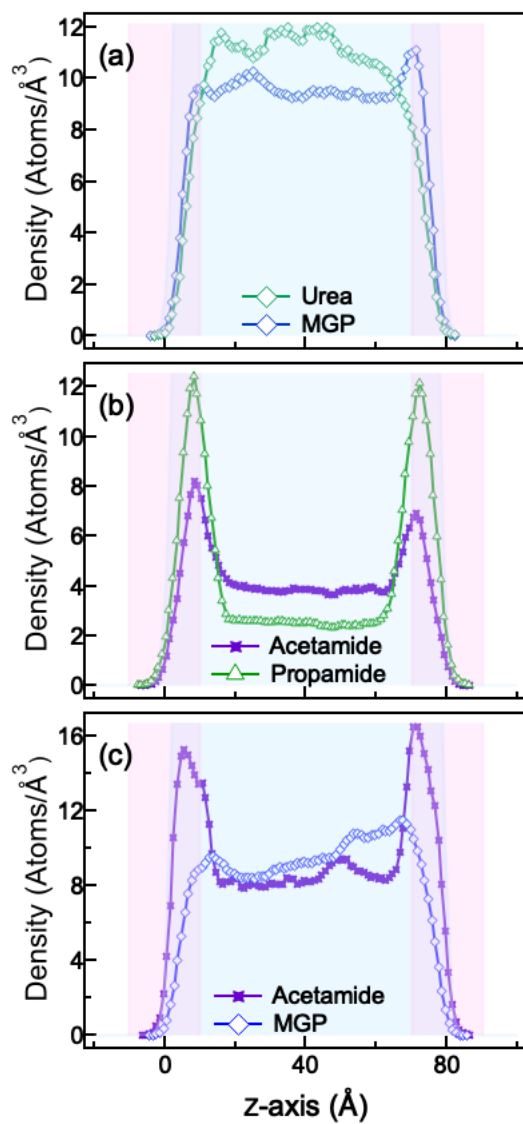


Figure 3.4 Density profiles of (a) MGP (blue open diamonds) and urea (green filled diamonds), (b) acetamide (purple stars) and propionamide (open green triangles), and (c) acetamide (purple stars) and MGP (blue open diamonds) across the water-bulk (blue shaded area), air-water interface (purple shaded area), and air (unshaded area).

Table 3.6 Normalized integrated density profiles (% of total area)

Molecules	Interface ^a	Bulk area
MGP	16	84
Urea	11	89
Acetamide	28	72
Propionamide	45	55
MGP	17	83
Acetamide	33	67

^aLeft and right

In Figure 3.4b, the density profiles of propionamide and acetamide show a sharp increase with maxima within the interface. The bulk density is found to be much lower than that of urea and MGP (Figure 3.4a). The propionamide density profile displays a sharper density rise within the interfacial region compared to that of acetamide, resulting in 45% of the propionamide molecules within the interface compared to 28% for acetamide (see Table 3.6). The trends described in Figures 3.4a and b for MGP and acetamide are also observed in Figure 3.4c for a mixture of MGP and acetamide. In all cases, in Figure 3.4, within the fluctuations of the models, the density profile of a given molecule is found to be independent of the chemical composition.

The shape of the profiles observed for urea and MGP in Figure 3.4 is likely due to the amphipathic properties of MGP and the strictly hydrophilic nature of urea. Urea possesses only polar functional groups, two NH₂ groups and one carbonyl group, all contributing to its hydrophilicity and overall bulk preference. MGP possesses polar functional groups (hydroxyl group) and one non-polar functional group (methyl). The polar functional groups contribute to its hydrophilic tendency resulting in bulk preference, but the presence of one methyl group in MGP induces a change that reduces the molecule's hydrophilicity. The effect of the methyl group is apparent when comparing the density profiles of MGP and D-glucose (Figure A3). In the case of

acetamide and propionamide the hydrophobicity of the alkyl functional group increases with increasing chain length,¹³⁹⁻¹⁴² leading to a distinct propionamide preference for the interface. These results highlight the effects that functional groups have on the behavior of molecules near the water surface.

For all the investigated solutes, the bulk concentration is achieved within 2-nm from the water surface. For surface-active molecules it results in a thin layer with concentrations higher than that of the bulk. Similar surface-enhanced concentrations have been observed for aqueous particles containing ionic solutes.^{143,144} In this case the thickness of the surface excess charge layer ranges from 1.4 to 2 nm depending on the ion structure and is independent of the particle size. The similarities between the two systems suggest that the thickness of the partitioning layer is a property of the solvent and may be independent of the solute. Although not investigated here, the thickness of the partitioning layer is likely to also be independent of the particle size. For larger particles (>1 μm), any interfacial phenomena would therefore also occur within a similar 2-nm layer. Even though the fraction of the interface volume to that of the particle decreases with increasing particle radius, the properties of this layer are sufficient to considerably enhanced chemical mechanisms in microdroplets.^{15,17}

3.4.2 Molecular orientation

Equations 1 and 2 were also used to plot the density profiles for individual functional groups of the solutes. Figure 3.5 displays the atom density profile for (a) MGP, (b) acetamide, and (c) propionamide along the z -axis. The MGP carbon labeling is displayed in Figure A4. For all 3 molecules, the density profiles of the methyl group (black lines) are shifted toward the surface compared to those of the other functional groups. In the water bulk, all profiles are indistinguishable. The methyl density distribution profiles suggest that the molecules loose

rotational freedom near the surface and adopt a preferred orientation with the most hydrophobic group pointing toward the water surface. Molecules recover full rotational freedom 2 nm away from the surface. Urea and glucose show no preferred orientation when found at the interface (see atom density profiles in Figure A5). The preferred orientation of the molecules at the interface is consistent with previous findings for alkanes.¹⁴¹ Preferred molecular orientations at interfaces was suggested by Zare and co-workers¹⁷ to explain the production of sugar phosphates in charged microdroplets. The orientation adopted by the acetamide, propionamide, and MGP are attributed to nonpolar hydrophobic nature of the methyl functional group.^{145,146} Figure 3.6 is a snapshot of the interface showing the MGP preferred orientation with the methyl group pointing toward the surface.

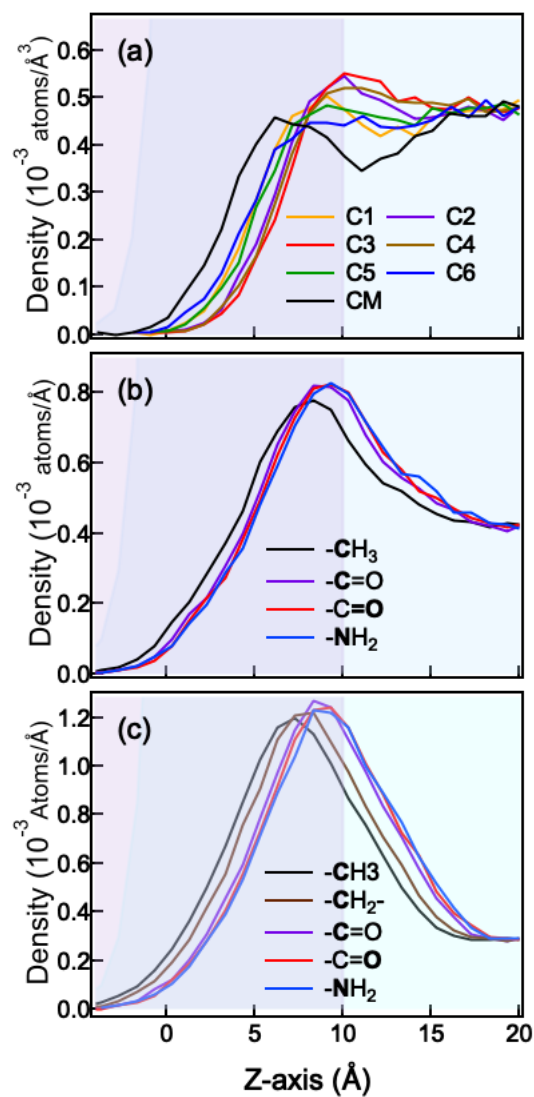


Figure 3.5 Atom density profiles for (a) MGP, (b) acetamide, and (c) propionamide across the water-bulk (turquoise blue), air-water interface (purple) interface).

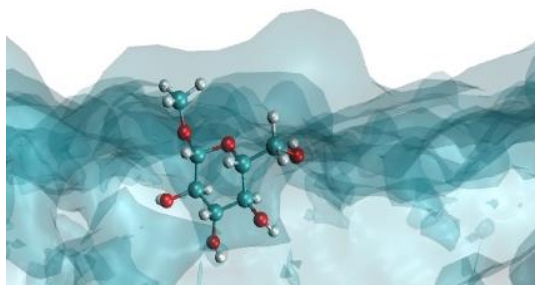


Figure 3.6 Snapshot of the air–water interface showing an oriented methyl β-D-glucopyranoside molecules.

3.4.3 Interfacial solvation and OH-solute interactions

The structures of the solute solvation shells were obtained by probing the instantaneous configurations of each solute at every time step (100 frames) of the MD trajectories. The water molecules included in the solvation sphere were determined based on the distance between the water oxygen atom to any of the carbon atoms of the solute. The cutoff distance corresponds to the first local minima of the oxygen–solute radical distribution functions.^{147,148} Similar instantaneous configurations of OH radical–solute positions were also sampled. The number of OH radicals around the solutes were determined based on the distance of the radical oxygen atom to any one of the carbon atoms of the solutes.

Table 3.7 Number of molecules around solutes. The number in parenthesis indicates the cutoff distance for determination of the solvation sphere.

	Bulk		Interface	
	H ₂ O	OH·	H ₂ O	OH·
OH radical (4.25 Å)	15.3	--	4.5	--
OH radical (2.45 Å)	3.3	--	1.5	--
Acetamide (4.25 Å)	27.4	0	15.4	0.3
Urea (4.30 Å)	23.7	0	15.2	0.1
Glucose (4.30 Å)	35.3	0	29.8	0.1
MGP (4.30 Å)	38.4	0	30.6	0.1

Table 3.7 displays the number of water or OH molecules around the different solutes in the bulk or within the interface. The values displayed in Table 3.7 for the OH are without any other solutes. The solvation shell of the OH radical is found to vary by up to 10% (not shown) depending on the solutes present in the water box. The change in functional group in the solute does not have large effects on the solvation sphere as observed for other systems.¹⁴⁸⁻¹⁵⁰ The hydration shell for surface active solutes and the OH radical, are found to decrease considerably at the interface. Similar “half-hydration” have been observed for molecules such as coumarin 110.⁹² The change is less significant for glucose and MGP, although in the case of methyl

substituted sugar, the lower hydration shell is consistent with the alignment of the methyl group toward the surface.

According to the mobility mechanism of the OH radical in solution⁴⁷ and because of the lower solvation sphere, the encounter of the solute with the radical will take less steps at the interface than in the bulk. This is evidenced in Table 3.7 by the higher number of OH radical penetrating the solute solvation shell within the interface compared to the bulk. A higher collision rate of the reactant within the interface could lead to enhanced reactivity. Other solvation effects, such as stabilization of the transition states and intermediates needs to be investigated to fully understand how the interfacial solvation may affect the reactivity.

Radial pair distribution functions (RDFs) $g(r)$ were plotted to quantify the interaction between the OH radical and the different functional groups of the organic solutes in both the interface and the bulk regions. Figure 3.7 displays the RDFs of the OH radical H atom with the carbonyl oxygen atom of (a) urea, (b) acetamide, and (c) propionamide in the bulk (red lines) and at the air–water interface (blue lines). RDFs for the interaction of the OH radical with the other atoms are displayed in Figure A6. In Figure 3.7 the RDFs displays two maxima, one for distances below 3 Å and one for longer distances. The sharp peak at short distances is characteristic of hydrogen bonding interactions between the radical H atom and the carbonyl oxygen. For all three molecules, within the interface, this peak is more intense than the second broader peak. Its intensity decreases within the bulk, and in the case of propionamide, becomes very small compared to that of the broader peak. A similar difference between RDFs in the bulk and interface is observed for the carbonyl carbon (Figure A6). Radical distribution functions in the interface also appear to decay faster with r than those in the bulk. This suggests a tighter interaction between the OH radical and the organic solute within the interface. This is likely due

to the different molecular packing and solvation at the interface relatively to the bulk. Although such interactions may not be representative of the reactive potential between the radical and the molecule, they provide valuable information to understand surface phenomena in aqueous aerosols.

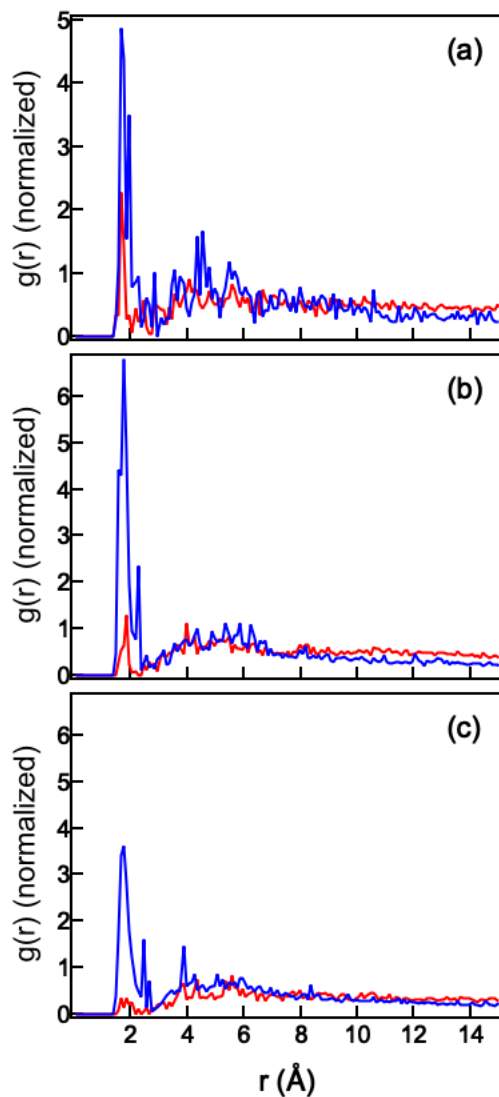


Figure 3.7 Radial pair distribution functions of the OH radical H atom with the carbonyl oxygen atom for (a) urea, (b) acetamide, and (c) propionamide in the bulk (red lines) and at the air-water interface (blue lines). The profiles are normalized by the area under the curve.

3.5 Conclusion and implications for atmospheric heterogeneous chemistry

The MD simulations described above provide a molecular level snapshot of the air–water interface as found in atmospheric multicomponent aqueous droplets. Analysis of the density profiles and radial distribution functions provides quantitative information about the dimension and composition of the interface and shows how molecular structure governs the behavior of the solutes near the water surface. Although it does not model the whole droplet, the simulations show that:

- (1) Bulk properties are reached within the first 2 nm of the surface. Surface active molecules are found to accumulate within the top 2 nm of the droplet while surface inactive molecules form a depletion zone at the surface. For a particle containing a mixture of urea and acetamide, the properties of the outer phase are solely defined by acetamide, while those of the inner phase are mostly defined by urea. The MD simulations also show that the OH radicals preferentially accumulate within the 2-nm interfacial region. The dimension of the interface is comparable to the diffusion–reaction length ($\sim 1\text{--}2\text{ nm}$)⁵⁷⁻⁶⁰ of the radical under reactive conditions. This overlap is likely to lead to interface-specific reaction mechanisms and kinetics. For aqueous aerosol for which diffusion of the reactants to the surface is not the rate limiting step, surface active molecules are rapidly consumed while surface inactive molecules are shielded from direct reaction with the oxidant.¹³
- (2) Surface active solutes lose rotational freedom and orient themselves with the hydrophobic group pointing toward the water surface. Methyl-substituted glucose is mostly surface inactive with low surface concentrations but still displays a preferred surface orientation due to the presence of a methyl group. Hydrophobic organic groups will become more accessible for reaction, changing the likely reaction mechanism compared to that of the

bulk. Such behavior is expected for surfactant with large alkyl chains and is shown to happen here for smaller molecules.

- (3) Reduced OH radical and solute solvation at the interface leads to an increased number of OH radicals coming into contact with surface active solutes. The number of water molecules in the radical and solutes solvation spheres is found to decrease considerably within the interface. The extend of this decrease depends on the molecular structure. This is also confirmed by a tighter interaction between the OH radical and the organic solute within the interface as observed in the radial pair distribution functions. The effects will contribute to a change in reaction rate coefficients within the interface compared to the bulk.

The increased surface concentration, molecular orientation, and tighter OH–solute interaction all suggests an enhanced reactivity of surface-active molecule within the air–water interface. No such enhancement is expected for surface inactive solutes. These findings have major implications for the chemical transformation of aqueous aerosols where the interface is a gateway for atmospheric oxidizers. The different surface behavior of the organic solutes can explain heterogeneous atmospheric phenomena that are inconsistent with known bulk liquid or gas phase chemistry.^{19,151}

Amides and urea have been detected in atmospheric aerosols¹⁵² and are known to be oxidized by the OH radical.¹⁵³ In mixed particles, urea will be shielded from reaction with OH radicals by surrounding surface active compounds. In the gas phase, amides react with the OH radical through abstraction of a hydrogen atom from the alkyl group, with negligible abstraction from the NH₂ group.¹⁵⁴ Although the overall gas phase rate coefficients are relatively low ($<2 \times 10^{-12} \text{ cm}^3 \text{ s}^{-1}$) for gas phase reactions, reaction with OH remains the main amide sink in the atmosphere.¹⁵⁴ In the

aqueous aerosol phase, abstraction of an alkyl hydrogen atom is likely to remain the dominant initial reaction pathway for reaction of OH with amines. The loss of rotational freedom observed at the interface and the exposure of the alkyl group toward the particle surface may enhance the accessibility of alkyl hydrogens for abstraction by the OH radicals. Under such conditions, the interface reaction is likely to be faster than that occurring in the bulk. Saccharide molecules have also been detected in aerosols,¹⁵⁵ and the effect of surface partitioning on their heterogeneous oxidation has been discussed.¹³ Alkyl substituted saccharides however, may have drastically different behavior as they are more likely to be found at the interface and to lose their rotational freedom.

These findings are likely to apply to more abundant atmospheric compounds such as dicarboxylic acids. The OH radical reacts with dicarboxylic acids by abstraction of a hydrogen atom from the carbon chain. Upon addition of molecular oxygen, the reaction proceeds through Russell disproportionation or Bennett–Summers elimination as observed in the gas phase.¹⁵⁶ The final products are a mixture of alcohols and ketones. Scission of the carbon chain may lead to the formation of small volatile fragments. The final composition of the particle will be greatly dependent on the structure of the reacting acid. In the case of a multicomponent particle, molecules at the particle surface will be more likely to react with the OH radical, making the overall chemical scheme very different from that of a system where the OH radical can react with all the solutes. Model trying to reproduce the chemical evolution of atmospheric aerosols must take such phenomena into account to accurately reproduce the heterogeneous chemistry.

References

- (1) Vepsäläinen, S.; Calderon, S. M.; Malila, J.; Prisle, N. L. Comparison of six approaches to predicting droplet activation of surface active aerosol - Part 1: moderately surface active organics. *Atmos. Chem. Phys.* **2022**, *22* (4), 2669-2687.
- (2) Lowe, S. J.; Partridge, D. G.; Davies, J. F.; Wilson, K. R.; Topping, D.; Riipinen, I. Key drivers of cloud response to surface-active organics. *Nat. Commun.* **2019**, *10*, 5214:1-12.
- (3) Nozière, B.; Baduel, C.; Jaffrezo, J. L. The dynamic surface tension of atmospheric aerosol surfactants reveals new aspects of cloud activation. *Nat. Commun.* **2014**, *5*, 3335:1-7.
- (4) Ruehl, C. R.; Davies, J. F.; Wilson, K. R. An interfacial mechanism for cloud droplet formation on organic aerosols. *Science* **2016**, *351* (6280), 1447-1450.
- (5) Bianchi, F.; Tröstl, J.; Junninen, H.; Frege, C.; Henne, S.; Hoyle, C. R.; Molteni, U.; Herrmann, E.; Adamov, A.; Bukowiecki, N.; et al. New particle formation in the free troposphere: A question of chemistry and timing. *Science* **2016**, *352*, 1109-1112.
- (6) Lehtipalo, K.; Dada, L.; Bianchi, F.; Xiao, M.; Wagner, R.; Stolzenburg, D.; Ahonen, L.; Amorim, A.; Baccarini, A.; Lehtipalo, K.; et al. Multicomponent new particle formation from sulfuric acid , ammonia , and biogenic vapors To cite this version : HAL Id : hal-01975898 Multicomponent new particle formation from sulfuric acid , ammonia , and biogenic vapors. *Science Advances* **2021**, *4* (12), eaau536:1-9.
- (7) Zhang, R.; Khalizov, A.; Wang, L.; Hu, M.; Xu, W. Nucleation and growth of nanoparticles in the atmosphere. *Chemical Reviews* **2012**, *112*, 1957-2011.
- (8) Zhao, Z.; Kong, K.; Wang, S.; Zhou, Y.; Cheng, D.; Wang, W.; Zeng, X. C.; Li, H. Understanding Hygroscopic Nucleation of Sulfate Aerosols: Combination of Molecular Dynamics Simulation with Classical Nucleation Theory. *J. Phys. Chem. Lett.* **2019**, *10*, 1126-1132.

- (9) Zeng, M. R.; Liu, C. L.; Wilson, K. R. Catalytic Coupling of Free Radical Oxidation and Electrophilic Chlorine Addition by Phase-Transfer Intermediates in Liquid Aerosols. *J. Phys. Chem. A* **2022**, *126* (19), 2959-2965.
- (10) Zeng, M. R.; Wilson, K. R. Experimental evidence that halogen bonding catalyzes the heterogeneous chlorination of alkenes in submicron liquid droplets. *Chem. Sci.* **2021**, *12* (31), 10455-10466.
- (11) Wilson, K. R.; Prophet, A. M.; Rovelli, G.; Willis, M. D.; Rapf, R. J.; Jacobs, M. I. A kinetic description of how interfaces accelerate reactions in micro-compartments. *Chem. Sci.* **2020**, *11* (32), 8533-8545.
- (12) Martins-Costa, M. T. C.; Anglada, J. M.; Francisco, J. S.; Ruiz-Lopez, M. F. Photosensitization mechanisms at the air-water interface of aqueous aerosols. *Chem. Sci.* **2022**, *13* (9), 2624-2631.
- (13) Fan, H.; Wenyika Masaya, T.; Goulay, F. Effect of surface-bulk partitioning on the heterogeneous oxidation of aqueous saccharide aerosols. *Phys. Chem. Chem. Phys.* **2019**, *21*, 2992-3001.
- (14) Ruiz-Lopez, M. F.; Francisco, J. S.; Martins-Costa, M. T. C.; Anglada, J. M. Molecular reactions at aqueous interfaces. *Nat. Rev. Chem.* **2020**, *4* (9), 459-475.
- (15) Lee, J. K.; Walker, K. L.; Han, H. S.; Kang, J.; Prinz, F. B.; Waymouth, R. M.; Nam, H. G.; Zare, R. N. Spontaneous generation of hydrogen peroxide from aqueous microdroplets. *Proc. Natl. Acad. Sci. U.S.A* **2019**, *116* (39), 19294-19298.
- (16) Qian, Y. Q.; Brown, J. B.; Huang-Fu, Z. C.; Zhang, T.; Wang, H.; Wang, S. Y.; Dadap, J. I.; Rao, Y. In situ analysis of the bulk and surface chemical compositions of organic aerosol particles. *Comm. Chem.* **2022**, *5* (1), 58:1-7.

- (17) Nam, I.; Lee, J. K.; Nam, H. G.; Zare, R. N. Abiotic production of sugar phosphates and uridine ribonucleoside in aqueous microdroplets. *Proc. Natl. Acad. Sci. U.S.A* **2017**, *114* (47), 12396-12400.
- (18) Kusaka, R.; Nihonyanagi, S.; Tahara, T. The photochemical reaction of phenol becomes ultrafast at the air-water interface. *Nature chemistry* **2021**, *13*, 306-311.
- (19) Ishiyama, T.; Tahara, T.; Morita, A. Why the Photochemical Reaction of Phenol Becomes Ultrafast at the Air–Water Interface: The Effect of Surface Hydration. *J. Am. Chem. Soc.* **2022**, *144*, 6321-6325.
- (20) Zhu, C. Q.; Zeng, X. C.; Francisco, J. S.; Gladich, I. Hydration, Solvation, and Isomerization of Methylglyoxal at the Air/Water Interface: New Mechanistic Pathways. *J. Am. Chem. Soc.* **2020**, *142* (12), 5574-5582.
- (21) Donaldson, D. J.; Valsaraj, K. T. Adsorption and Reaction of Trace Gas-Phase Organic Compounds on Atmospheric Water Film Surfaces: A Critical Review. *Environ. Sci. Technol.* **2010**, *44* (3), 865-873.
- (22) Nissenon, P.; Knox, C. J. H.; Finlayson-Pitts, B. J.; Phillips, L. F.; Dabdub, D. Enhanced photolysis in aerosols: evidence for important surface effects. *Phys. Chem. Chem. Phys.* **2006**, *8* (40), 4700-4710.
- (23) Wingen, L. M.; Moskun, A. C.; Johnson, S. N.; Thomas, J. L.; Roeselova, M.; Tobias, D. J.; Kleinman, M. T.; Finlayson-Pitts, B. J. Enhanced surface photochemistry in chloride-nitrate ion mixtures. *Phys. Chem. Chem. Phys.* **2008**, *10* (37), 5668-5677.
- (24) Valsaraj, K. T. A Review of the Aqueous Aerosol Surface Chemistry in the Atmospheric Context. *Open Journal of Physical Chemistry* **2012**, *2012*, 58-66.

- (25) Shantz, N. C.; Leitch, W. R.; Caffrey, P. F. Effects of organics of low solubility on the growth rate of cloud droplets. *J. Geophys. Res.-Atmos.* **2003**, *108*, 1-9.
- (26) Asa-Awuku, A.; Miracolo, M. A.; Kroll, J. H.; Robinson, A. L.; Donahue, N. M. Mixing and phase partitioning of primary and secondary organic aerosols. *Geophys. Res. Lett.* **2009**, *36*, 1-5.
- (27) Huang, Y.; Mahrt, F.; Xu, S.; Shiraiwa, M.; Zuend, A.; Bertram, A. K. Coexistence of three liquid phases in individual atmospheric aerosol particles. *Proc. Natl. Acad. Sci. U.S.A* **2021**, *118*, e2102512118: 1-9.
- (28) Karadima, K. S.; Mavrantzas, V. G.; Pandis, S. N. Insights into the morphology of multicomponent organic and inorganic aerosols from molecular dynamics simulations. *Atmos. Chem. Phys.* **2019**, *19*, 5571-5587.
- (29) Kucinski, T. M.; Dawson, J. N.; Freedman, M. A. Size-Dependent Liquid-Liquid Phase Separation in Atmospherically Relevant Complex Systems. *J. Phys. Chem. Lett.* **2019**, *10*, 6915-6920.
- (30) Vaden, T. D.; Song, C.; Zaveri, R. A.; Imre, D.; Zelenyuk, A. Morphology of mixed primary and secondary organic particles and the adsorption of spectator organic gases during aerosol formation. *Proc. Natl. Acad. Sci. U.S.A* **2010**, *107*, 6658-6663.
- (31) Fan, H. Y.; Goulay, F. Effect of Bulk Composition on the Heterogeneous Oxidation of Semi-Solid Atmospheric Aerosols. *Atmosphere* **2019**, *10* (12), 791:1-17.
- (32) Pegram, L. M.; Record, M. T. Using surface tension data to predict differences in surface and bulk concentrations of nonelectrolytes in water. *J. Phys. Chem. C* **2009**, *113*, 2171-2174.
- (33) Gerard, V.; Noziere, B.; Baduel, C.; Fine, L.; Frossard, A. A.; Cohen, R. C. Anionic, Cationic, and Nonionic Surfactants in Atmospheric Aerosols from the Baltic Coast at Asko, Sweden: Implications for Cloud Droplet Activation. *Environ. Sci. Technol.* **2016**, *50* (6), 2974-2982.

- (34) Petters, S. S.; Petters, M. D. Surfactant effect on cloud condensation nuclei for two-component internally mixed aerosols. *J. Geophys. Res.-Atmos.* **2016**, *121* (4), 1878-1895.
- (35) Frka, S.; Dautović, J.; Kozarac, Z.; Čosović, B.; Hoffer, A.; Kiss, G. Surface-active substances in atmospheric aerosol: An electrochemical approach. *Tellus B Chem. Phys. Meteorol.* **2012**, *64*.
- (36) Bzdek, B. R.; Reid, J. P.; Malila, J.; Prisle, N. L. The surface tension of surfactant-containing, finite volume droplets. *Proc. Natl. Acad. Sci. U.S.A* **2020**, *117*, 8335-8343.
- (37) Facchini, M. C.; Decesari, S.; Mircea, M.; Fuzzi, S.; Loglio, G. Surface tension of atmospheric wet aerosol and cloud/fog droplets in relation to their organic carbon content and chemical composition. *Atmos. Environ.* **2000**, *34*, 4853-4857.
- (38) Sorjamaa, R.; Svenningsson, B.; Raatikainen, T.; Henning, S.; Bilde, M.; Laaksonen, A. The role of surfactants in Köhler theory reconsidered. *Atmos. Chem. Phys.* **2004**, *4*, 2107-2117.
- (39) Harper, K.; Minofar, B.; Sierra-Hernandez, M. R.; Casillas-Ituarte, N. N.; Roeselova, M.; Allen, H. C. Surface Residence and Uptake of Methyl Chloride and Methyl Alcohol at the Air/Water Interface Studied by Vibrational Sum Frequency Spectroscopy and Molecular Dynamics. *J. Phys. Chem. A* **2009**, *113*, 2015-2024.
- (40) Roy, S.; Biswas, B.; Mondal, J. A.; Singh, P. C. Heterodyne-Detected Vibrational Sum Frequency Generation Study of Air-Water-Fluoroalcohol Interface: Fluorocarbon Group-Induced Structural and Orientational Change of Interfacial Water. *J. Phys. Chem. C* **2018**, *122*, 26928-26933.
- (41) Qian, Y. Q.; Deng, G. H.; Rao, Y. In Situ Spectroscopic Probing of Polarity and Molecular Configuration at Aerosol Particle Surfaces. *J. Phys. Chem. Lett.* **2020**, *11* (16), 6763-6771.
- (42) Berger, R.; Lilach, Y.; Ayoub, Y.; Asscher, M. Photochemistry of molecules at confined environment: CD₃Br/O/Ru(001) and CO₂ @ Ice. *Isr. J. Chem.* **2005**, *45* (1-2), 97-109.

- (43) Harrison, I.; Polanyi, J. C.; Young, P. A. Photochemistry of absorbed molecules .3. Photodissociation and photodesorption of CH₃Br adsorbed on LiF(001). *J. Chem. Phys.* **1988**, *89* (3), 1475-1497.
- (44) Klijn, J. E.; Engberts, J. Organic chemistry - Fast reactions 'on water'. *Nature* **2005**, *435* (7043), 746-747.
- (45) Litwinienko, G.; Ingold, K. U. Solvent effects on the rates and mechanisms of reaction of phenols with free radicals. *Acc. Chem. Res.* **2007**, *40*, 222-230.
- (46) Mitroka, S.; Zimmeck, S.; Troya, D.; Tanko, J. M. How solvent modulates hydroxyl radical reactivity in hydrogen atom abstractions. *J. Am. Chem. Soc.* **2010**, *132*, 2907-2913.
- (47) Codorniu-Hernández, E.; Kusalik, P. G. Mobility mechanism of hydroxyl radicals in aqueous solution via hydrogen transfer. *J. Am. Chem. Soc.* **2012**, *134*, 532-538.
- (48) Habartová, A.; Valsaraj, K. T.; Roeselová, M. Molecular dynamics simulations of small halogenated organics at the air-water interface: Implications in water treatment and atmospheric chemistry. *J. Phys. Chem. A* **2013**, *117*, 9205-9215.
- (49) Pašalić, H.; Roeselová, M.; Lischka, H. Methyl and pentyl chloride in a microhydrated environment and at the liquid water-vapor interface: A theoretical study. *J. Phys. Chem. B* **2011**, *115*, 1807-1816.
- (50) Burkholder, J. B.; Abbatt, J. P. D.; Barnes, I.; Roberts, J. M.; Melamed, M. L.; Ammann, M.; Bertram, A. K.; Cappa, C. D.; Carlton, A. G.; Carpenter, L. J.; et al. The Essential Role for Laboratory Studies in Atmospheric Chemistry. *Environ. Sci. Technol.* **2017**, *51*, 2519-2528.
- (51) Roeselová, M.; Vieceli, J.; Dang, L. X.; Garrett, B. C.; Tobias, D. J. Hydroxyl radical at the air-water interface. *J. Am. Chem. Soc.* **2004**, *126*, 16308-16309.

- (52) Vácha, R.; Slavíček, P. Adsorption of Atmospherically Relevant Gases at the Air / Water Interface : Free Energy Profiles of Aqueous Solvation of N₂, O₂, O₃, OH, H₂O, HO₂, and H₂O₂. *J. Phys. Chem. A* **2004**, *108*, 11573-11579.
- (53) Du, S.; Francisco, J. S. Interaction between OH radical and the water interface. *J. Phys. Chem. A* **2008**, *112* (21), 4826-4835.
- (54) Martins-Costa, M. T. C.; Anglada, J. M.; Francisco, J. S.; Ruiz-Lopez, M. F. Reactivity of atmospherically relevant small radicals at the air-water interface. *Angewandte Chemie - International Edition* **2012**, *51*, 5413-5417.
- (55) Apostolidou, C. OH radical in water from ab initio molecular dynamics simulation employing hybrid functionals. *J. Chem. Phys.* **2019**, *151* (6).
- (56) Apostolidou, C. Vibrational Spectra of the OH Radical in Water: Ab Initio Molecular Dynamics Simulations and Quantum Chemical Calculations Using Hybrid Functionals. *Advanced Theory and Simulations* **2020**, *3* (12).
- (57) Houle, F. A.; Wiegel, A. A.; Wilson, K. R. Changes in Reactivity as Chemistry Becomes Confined to an Interface. The Case of Free Radical Oxidation of C₃₀H₆₂ Alkane by OH. *J. Phys. Chem. Lett.* **2018**, *9* (5), 1053-1057.
- (58) Wiegel, A. A.; Wilson, K. R.; Hinsberg, W. D.; Houle, F. A. Stochastic methods for aerosol chemistry: a compact molecular description of functionalization and fragmentation in the heterogeneous oxidation of squalane aerosol by OH radicals. *Phys. Chem. Chem. Phys.* **2015**, *17* (6), 4398-4411.
- (59) Fan, H. Y.; Tinsley, M. R.; Goulay, F. Effect of Relative Humidity on the OH-Initiated Heterogeneous Oxidation of Monosaccharide Nanoparticles. *J. Phys. Chem. A* **2015**, *119* (45), 11182-11190.

- (60) Collins, D. B.; Grassian, V. H. Chapter 10: Gase-Liquid Interfaces in the Atmosphere: Impacts, Complexity, and Challenges. In *Physical Chemistry of GaseLiquid Interfaces*, Faust, J., House, J. E. Eds.; Elsevier, 2018; pp 271-313.
- (61) Hadizadeh, M. H.; Yang, L.; Fang, G.; Qiu, Z.; Li, Z. The mobility and solvation structure of a hydroxyl radical in a water nanodroplet: a Born–Oppenheimer molecular dynamics study. *Phys. Chem. Chem. Phys.* **2021**, *23*, 14628-14635.
- (62) Vassilev, P.; Louwerse, M. J.; Baerends, E. J. Ab initio molecular dynamics simulation of the OH center dot radical in liquid water. *Chemical Physics Letters* **2004**, *398* (1-3), 212-216.
- (63) VandeVondele, J.; Sprik, M. A molecular dynamics study of the hydroxyl radical in solution applying self-interaction-corrected density functional methods. *Phys. Chem. Chem. Phys.* **2005**, *7* (7), 1363-1367.
- (64) Codorniu-Hernandez, E.; Kusalik, P. G. Insights into the Solvation and Mobility of the Hydroxyl Radical in Aqueous Solution. *J. Chem. Theory Comput.* **2011**, *7* (11), 3725-3732.
- (65) Rana, B.; Herbert, J. M. Hidden Hemibonding in the Aqueous Hydroxyl Radical. *J. Phys. Chem. Lett.* **2021**, *12* (33), 8053-8060.
- (66) Campo, M. G.; Grigera, J. R. Classical molecular-dynamics simulation of the hydroxyl radical in water. *J. Chem. Phys.* **2005**, *123*.
- (67) Swiatla-Wojcik, D.; Szala-Bilnik, J. Mechanism of OH radical hydration: A comparative computational study of liquid and supercritical solvent. *J. Chem. Phys.* **2012**, *136* (6).
- (68) Nelson, W.; Manoharan, R.; Sperry, J. UV Resonance Raman Studies of Acetone.pdf. *Journal* 1992, (Issue).

- (69) Knudsen, R.; Sala, O.; Hase, Y. A low temperature matrix isolation infrared study of acetamides. I. Acetamide and some deuterated derivatives. *Journal of Molecular Structure* **1994**, *321*, 187-195.
- (70) Chen, X. G.; Schweitzer-Stenner, R.; Asher, S. A.; Mirkin, N. G.; Krimm, S. Vibrational assignments of trans-N-methylacetamide and some of its deuterated isotopomers from band decomposition of IR, visible, and resonance Raman spectra *The Journal of Physical Chemistry* **1995**, *99*, 3074-3083.
- (71) Schweitzer-Stenner, R.; Sieler, G.; Mirkin, N. G.; Krimm, S. Intermolecular coupling in liquid and crystalline states of trans-N-methylacetamide investigated by polarized raman and FT-IR spectroscopies. *J. Phys. Chem. A* **1998**, *102*, 118-127.
- (72) Woutersen, S.; Mu, Y.; Stock, G.; Hamm, P. Hydrogen-bond lifetime measured by time-resolved 2D-IR spectroscopy: N-methylacetamide in methanol. *Chemical Physics* **2001**, *266*, 137-147.
- (73) Barthel, J.; Buchner, R.; Wurm, B. The dynamics of liquid formamide, N-methylformamide, N,N-dimethylformamide, and N,N-dimethylacetamide. A dielectric relaxation study. *Journal of Molecular Liquids* **2002**, *98-99*, 51-69.
- (74) Xu, Z.; Li, H.; Wang, C.; Wu, T.; Han, S. Is the blue shift of C-H vibration in DMF-water mixture mainly caused by C-H...O interaction? *Chemical Physics Letters* **2004**, *394*, 405-409.
- (75) Zhang, R.; Li, H.; Lei, Y.; Han, S. Structures and interactions in N-methylacetamide-water mixtures studied by IR spectra and density functional theory. *Journal of Molecular Structure* **2004**, *693*, 17-25.

- (76) Zhang, R.; Li, H.; Lei, Y.; Han, S. All-atom molecular dynamic simulations and relative NMR spectra study of weak C-H...O contacts in amide-water systems. *The journal of physical chemistry. B* **2005**, *109*, 7482-7487.
- (77) DeCamp, M. F.; DeFlores, L.; McCracken, J. M.; Tokmakoff, A.; Kwac, K.; Cho, M. Amide I vibrational dynamics of N-methylacetamide in polar solvents: The role of electrostatic interactions. *J. Phys. Chem. B* **2005**, *109*, 11016-11026.
- (78) Fujitake, M.; Kubota, Y.; Ohashi, N. Fourier transform microwave spectroscopy of N,N-dimethylacetamide. *Journal of Molecular Spectroscopy* **2006**, *236*, 97-109.
- (79) Albrecht, M.; Rice, C. A.; Suhm, M. A. Elementary peptide motifs in the gas phase: FTIR aggregation study of formamide, acetamide, N-methylformamide, and N-methylacetamide. *J. Phys. Chem. A* **2008**, *112*, 7530-7542.
- (80) Zhou, Y.; Deng, G.; Zheng, Y. Z.; Xu, J.; Ashraf, H.; Yu, Z. W. Evidences for Cooperative Resonance-Assisted Hydrogen Bonds in Protein Secondary Structure Analogs. *Sci. Rep.* **2016**, *6*, 1-8.
- (81) Forsting, T.; Gottschalk, H. C.; Hartwig, B.; Mons, M.; Suhm, M. A. Correcting the record: The dimers and trimers of: Trans-N -methylacetamide. *Phys. Chem. Chem. Phys.* **2017**, *19*, 10727-10737.
- (82) Salamatova, E.; Cunha, A. V.; Bloem, R.; Roeters, S. J.; Woutersen, S.; Jansen, T. L. C.; Pshenichnikov, M. S. Hydrophobic Collapse in N -Methylacetamide-Water Mixtures. *J. Phys. Chem. A* **2018**, *122*, 2468-2478.
- (83) Jorgensen, W. L.; Gao, J. Cis-Trans Energy Difference for the Peptide Bond in the Gas Phase and in Aqueous Solution. *J. Am. Chem. Soc.* **1988**, *110*, 4212-4216.

- (84) Almeida, G. G.; Cordeiro, J. M. M. A Monte Carlo revisiting of N-methylformamide and acetone. *Journal of the Brazilian Chemical Society* **2011**, *22*, 2178-2185.
- (85) Chalaris, M.; Samios, J. Systematic molecular dynamics studies of liquid N,N-dimethylformamide using optimized rigid force fields: Investigation of the thermodynamic, structural, transport and dynamic properties. *The Journal of Chemical Physics* **2000**, *112*, 8581-8594.
- (86) Kwac, K.; Cho, M. Molecular dynamics simulation study of N-methylacetamide in water. II. Two-dimensional infrared pump-probe spectra. *The Journal of Chemical Physics* **2003**, *119*, 2256-2263.
- (87) Lei, Y.; Li, H.; Pan, H.; Han, S. Structures and Hydrogen Bonding Analysis of N , N - Dimethylformamide and. *J. Phys. Chem. A.* **2003**, 1574-1583.
- (88) Gaigeot, M. P.; Vuilleumier, R.; Sprik, M.; Borgis, D. Infrared spectroscopy of N-methylacetamide revisited by ab initio molecular dynamics simulations. *J. Chem. Theory Comput.* **2005**, *1*, 772-789.
- (89) Mennucci, B.; Martínez, J. M. How to model solvation of peptides? Insights from a quantum-mechanical and molecular dynamics study of N-methylacetamide. 1. Geometries, infrared, and ultraviolet spectra in water. *The journal of physical chemistry. B* **2005**, *109*, 9818-9829.
- (90) Aparicio-Martínez, S.; Balbuena, P. B. On the properties of aqueous amide solutions through classical molecular dynamics simulations. *Molecular Simulation* **2007**, *33*, 925-938.
- (91) Heyda, J.; Vincent, J. C.; Tobias, D. J.; Dzubiella, J.; Jungwirth, P. Ion specificity at the peptide bond: molecular dynamics simulations of N-methylacetamide in aqueous salt solutions. *The journal of physical chemistry. B* **2010**, *114*, 1213-1220.

- (92) Watanabe, H.; Yamaguchi, S.; Sen, S.; Morita, A.; Tahara, T. "Half-Hydration" At the Air/Water Interface Revealed By Heterodyne-Detected Electronic Sum Frequency Generation Spectroscopy, Polarization Second Harmonic Generation, and Molecular Dynamics Simulation. *Journal of Chemical Physics* **2010**, *132*.
- (93) Biswas, A.; Mallik, B. S. Structure and stretching dynamics of water molecules around an amphiphilic amide from FPMD simulations: A case study of N,N-dimethylformamide. *Journal of Molecular Liquids* **2020**, *302*, 112524.
- (94) Brady, J. W.; Ha, S. N. Molecular dynamics simulation of the aqueous solvation of sugars. *Advances in experimental medicine and biology* **1991**, *302*, 739-751.
- (95) Brady, J. W. Molecular dynamics simulations of carbohydrate solvation. In *Modern Methods for Multidimensional Dynamics Computations in Chemistry*, Thompson, D. L. Ed.; World Scientific, 1998; pp 384-400.
- (96) Engelsen, S.; Monteiro, C.; Penhoat, C.; Perez, S. The diluted aqueous solvation of carbohydrates as inferred from molecular dynamics simulations and NMR spectroscopy. *Biophysical Chemistry* **2001**, *93*, 103-127.
- (97) Kirschner, K. N.; Woods, R. J. Solvent interactions determine carbohydrate conformation. *Proceedings of the National Academy of Sciences* **2001**, *98*, 10541-10545.
- (98) Pereira, C. S.; Kony, D.; Baron, R.; Müller, M.; Van Gunsteren, W. F.; Hünenberger, P. H. Conformational and dynamical properties of disaccharides in water: A molecular dynamics study. *Biophysical Journal* **2006**, *90*, 4337-4344.
- (99) Ruda, A.; Widmalm, G.; Wohlert, J. O-methylation in carbohydrates: An NMR and MD simulation study with application to methylcellulose. *J. Phys. Chem. B* **2021**, *125*, 11967-11979.

- (100) Palivec, V.; Johannessen, C.; Kaminský, J.; Martinez- Seara, H. Use of Raman and Raman optical activity to extract atomistic details of saccharides in aqueous solution. *PLoS Computational Biology* **2022**, *18*, 1-28.
- (101) Yuet, P. K.; Blankschtein, D. Molecular dynamics simulation study of water surfaces: Comparison of flexible water models. *J. Phys. Chem. B* **2010**, *114*, 13786-13795.
- (102) Fan, Y.; Chen, X.; Yang, L.; Cremer, P.; Gao, Y. Q. On the structure of water at the aqueous/air interface. *J. Phys. Chem. B* **2009**, *113*, 11672-11679.
- (103) MacKerell, A. D.; Bashford, D.; Bellott, M.; Dunbrack, R. L.; Evanseck, J. D.; Field, M. J.; Fischer, S.; Gao, J.; Guo, H.; Ha, S.; et al. All-atom empirical potential for molecular modeling and dynamics studies of proteins. *J. Phys. Chem. B* **1998**, *102*, 3586-3616.
- (104) Jorgensen, W. L.; Chandrasekhar, J.; Madura, J. D.; Impey, R. W.; Klein, M. L. Comparison of simple potential functions for simulating liquid water. *J. Chem. Phys.* **1983**, *79*, 926-935.
- (105) Svishchev, I. M.; Plugatyr, A. Y. Hydroxyl radical in aqueous solution: Computer simulation. *J. Phys. Chem. B* **2005**, *109*, 4123-4128.
- (106) Guvench, O.; Greenr, S. N.; Kamath, G.; Brady, J. W.; Venable, R. M.; Pastor, R. W.; Mackerell, A. D. Additive empirical force field for hexopyranose monosaccharides. *J. Comput. Chem.* **2008**, *29*, 2543-2564.
- (107) Hatcher, E. R.; Guvench, O.; MacKerell, A. D. CHARMM Additive All-Atom Force Field for Acyclic Polyalcohols, Acyclic Carbohydrates, and Inositol. *J. Chem. Theory Comput.* **2009**, *5*, 1315-1327.
- (108) Darden, T.; York, D.; Pedersen, L. Particle mesh Ewald: An $N \cdot \log(N)$ method for Ewald sums in large systems. *J. Chem. Phys.* **1993**, *98*, 10089-10092.

- (109) Iupinov, A. Implementation of the Particle Mesh Ewald method on a GPU. Royal Institute of Technology, Stockholm, Sweden, 2016.
- (110) Phillips, J. C.; Hardy, D. J.; Maia, J. D. C.; Stone, J. E.; Ribeiro, J. V.; Bernardi, R. C.; Buch, R.; Fiorin, G.; Hémin, J.; Jiang, W.; et al. Scalable molecular dynamics on CPU and GPU architectures with NAMD. *J. Chem. Phys.* **2020**, *153*, 044130:1-33.
- (111) Martinez, L.; Andrade, R.; Birgin, E. G.; Martinez, J. M. PACKMOL: A Package for Building Initial Configurations for Molecular Dynamics Simulations. *J. Comput. Chem.* **2009**, *30* (13), 2157-2164.
- (112) Humphrey, W.; Dalke, A.; Schulten, K. Sartorius products. *J. Mol. Graph.* **1996**, *14*, 33-38.
- (113) Grønbech-Jensen, N.; Farago, O. Constant pressure and temperature discrete-time Langevin molecular dynamics. *J. Chem. Phys.* **2014**, *141*, 194108:1-12.
- (114) Wang, X.; Chen, C.; Binder, K.; Kuhn, U.; Pöschl, U.; Su, H.; Cheng, Y. Molecular dynamics simulation of the surface tension of aqueous sodium chloride: From dilute to highly supersaturated solutions and molten salt. *Atmos. Chem. Phys.* **2018**, *18*, 17077-17086.
- (115) Giorgino, T. Computing 1-D atomic densities in macromolecular simulations: The density profile tool for VMD. *Comput. Phys. Commun.* **2014**, *185*, 317-322.
- (116) Levine, B. G.; Stone, J. E.; Kohlmeyer, A. Fast analysis of molecular dynamics trajectories with graphics processing units-Radial distribution function histogramming. *J. Comput. Phys.* **2011**, *230*, 3556-3569.
- (117) Pranami, G.; Lamm, M. H. Estimating Error in Diffusion Coefficients Derived from Molecular Dynamics Simulations. *J. Chem. Theory Comput.* **2015**, *11*, 4586-4592.

- (118) Haile, J. M. Molecular dynamics simulation : elementary methods LK - <https://libwvu.on.worldcat.org/oclc/37927840>. Wiley professional paperback series TA - TT - **1997**.
- (119) Wang, J. M.; Hou, T. J. Application of Molecular Dynamics Simulations in Molecular Property Prediction. 1. Density and Heat of Vaporization. *J. Chem. Theory Comput.* **2011**, 7 (7), 2151-2165.
- (120) van der Spoel, D.; van Maaren, P. J.; Berendsen, H. J. C. A systematic study of water models for molecular simulation: Derivation of water models optimized for use with a reaction field. *Journal* 1998, 108 (Issue), 10220-10230.
- (121) Mark, P.; Nilsson, L. Structure and dynamics of the TIP3P, SPC, and SPC/E water models at 298 K. *J. Phys. Chem. A* **2001**, 105, 9954-9960.
- (122) Mahoney, M. W.; Jorgensen, W. L. Diffusion constant of the TIP5P model of liquid water. *The Journal of Chemical Physics* **2001**, 114, 363-366.
- (123) Wu, Y.; Tepper, H. L.; Voth, G. A. Flexible simple point-charge water model with improved liquid-state properties. *The Journal of Chemical Physics* **2006**, 124, 24503.
- (124) Vega, C.; De Miguel, E. Surface tension of the most popular models of water by using the test-area simulation method. *J. Chem. Phys.* **2007**, 126, 1-10.
- (125) Wang, J.; Hou, T. Application of molecular dynamics simulations in molecular property prediction II: diffusion coefficient. *J. Comput. Chem.* **2011**, 32, 3505-3519.
- (126) Leontyev, I. V.; Stuchebrukhov, A. A. Polarizable Mean-Field Model of Water for Biological Simulations with Amber and Charmm force fields. *J. Chem. Theory Comput.* **2012**, 8, 3207-3216.

- (127) Chen, Y.-D.; Li, A., Huang-Te; Wang, Y.-S.; Chao, S., D. . Molecular dynamics simulations of liquid water structure and diffusivity *Chimese Journal of Physics* **2013**, *51* (6), 1218-1229.
- (128) Yu, W.; Lopes, P. E. M.; Roux, B.; MacKerell, A. D. Six-site polarizable model of water based on the classical Drude oscillator. *The Journal of Chemical Physics* **2013**, *138*, 34508.
- (129) Braun, D.; Boresch, S.; Steinhauser, O. Transport and dielectric properties of water and the influence of coarse-graining: Comparing BMW, SPC/E, and TIP3P models. *The Journal of Chemical Physics* **2014**, *140*, 64107.
- (130) Holz, M.; Heil, S. R.; Sacco, A. Temperature-dependent self-diffusion coefficients of water and six selected molecular liquids for calibration in accurate ¹H NMR PFG measurements. *Phys. Chem. Chem. Phys.* **2000**, *2*, 4740-4742.
- (131) Price, D. J.; Brooks, C. L. A modified TIP3P water potential for simulation with Ewald summation. *J. Chem. Phys.* **2004**, *121*, 10096-10103.
- (132) De Kock, M. B.; Azim, S.; Kassier, G. H.; Miller, R. J. D. Determining the radial distribution function of water using electron scattering: A key to solution phase chemistry. *J. Chem. Phys.* **2020**, *153*, 194504:1-9.
- (133) Soper, A. K.; Phillips, M. G. A new determination of the structure of water at 25°C. *Chemical Physics* **1986**, *107*, 47-60.
- (134) Campo, M. G.; Grigera, J. R. Classical molecular-dynamics simulation of the hydroxyl radical in water. *J. Chem. Phys.* **2005**, *123* (8).
- (135) Aguilar-Pineda, J. A.; Mendez-Maldonado, G. A.; Nunez-Rojas, E.; Alexandre, J. Parametrisation of a force field of acetamide for simulations of the liquid phase. *Mol. Phys.* **2015**, *113* (17-18), 2716-2724.

- (136) Halonen, S.; Kangas, T.; Haataja, M.; Lassi, U. Urea-Water-Solution Properties: Density, Viscosity, and Surface Tension in an Under-Saturated Solution. *Emiss. Control Sci. Technol.* **2017**, *3*, 161-170.
- (137) Lee, J. Y.; Hildemann, L. M. Surface tension of solutions containing dicarboxylic acids with ammonium sulfate, D-glucose, or humic acid. *J. Aerosol. Sci.* **2013**, *64*, 94-102.
- (138) Julin, J.; Shiraiwa, M.; Miles, R. E. H.; Reid, J. P.; Pöschl, U.; Riipinen, I. Mass accommodation of water: Bridging the gap between molecular dynamics simulations and kinetic condensation models. *J. Phys. Chem. A* **2013**, *117*, 410-420.
- (139) Chen, W.; Karde, V.; Cheng, T. N. H.; Ramli, S. S.; Heng, J. Y. Y. Surface hydrophobicity: effect of alkyl chain length and network homogeneity. *Front. Chem. Sci. Eng.* **2021**, *15*, 90-98.
- (140) Gao, Y.; Duan, L.; Guan, S.; Gao, G.; Cheng, Y.; Ren, X.; Wang, Y. The effect of hydrophobic alkyl chain length on the mechanical properties of latex particle hydrogels. *RSC Adv.* **2017**, *7*, 44673-44679.
- (141) Jackson, M. B. The Hydrophobic Effect in Solute Partitioning and Interfacial Tension. *Sci. Rep.* **2016**, *6*, 6-9.
- (142) Yun, H.; Choi, Y. W.; Kim, N. J.; Sohn, D. Physicochemical properties of phosphatidylcholine (PC) monolayers with different alkyl chains, at the air/water interface. *Bull. Korean. Chem. Soc.* **2003**, *24*, 377-383.
- (143) Kwan, V.; Consta, S. Bridging electrostatic properties between nanoscopic and microscopic highly charged droplets. *Chemical Physics Letters* **2020**, 746.
- (144) Kwan, V.; Consta, S. Molecular Characterization of the Surface Excess Charge Layer in Droplets. *Journal of the American Society for Mass Spectrometry* **2021**, *32* (1), 33-45.

- (145) Jonsson, A. L.; Roberts, M. A. J.; Kiappes, J. L.; Scott, K. A. Essential chemistry for biochemists. *Essays Biochem.* **2017**, *61*, 401-427.
- (146) Monroe, J. I.; Jiao, S.; Davis, R. J.; Brown, D. R.; Katz, L. E.; Shell, M. S. Affinity of small-molecule solutes to hydrophobic, hydrophilic, and chemically patterned interfaces in aqueous solution. *Proc. Natl. Acad. Sci. U.S.A* **2021**, *118*, 1-10.
- (147) Mountain, R. D. Solvation structure of ions in water. *International Journal of Thermophysics* **2007**, *28*, 536-543.
- (148) Wick, C. D.; Xantheas, S. S. Computational Investigation of the First Solvation Shell Structure of Interfacial and Bulk Aqueous Chloride and Iodide Ions. *The Journal of Physical Chemistry B* **2009**, *113*, 4141-4146.
- (149) Long, J. A. Hydrophobic Hydration and Aggregation in Aqueous Solutions. Journal 2017, Doctor of Philosophy (PhD) (Issue).
- (150) Conti Nibali, V.; Pezzotti, S.; Sebastiani, F.; Galimberti, D. R.; Schwaab, G.; Heyden, M.; Gaigeot, M. P.; Havenith, M. Wrapping up Hydrophobic Hydration: Locality Matters. *J. Phys. Chem. Lett.* **2020**, *11*, 4809-4816.
- (151) Tabazadeh, A.; Yokelson, R. J.; Singh, H. B.; Hobbs, P. V.; Crawford, J. H.; Iraci, L. T. Heterogeneous chemistry involving methanol in tropospheric clouds. *Geophys. Res. Lett.* **2004**, *31*, 2-5.
- (152) Booyens, W.; Van Zyl, P. G.; Beukes, J. P.; Ruiz-Jimenez, J.; Kopperi, M.; Riekkola, M. L.; Vakkari, V.; Josipovic, M.; Kulmala, M.; Laakso, L. Characterising Particulate Organic Nitrogen at A Savannah-Grassland Region in South Africa. *Atmosphere* **2019**, *10* (9), 492:1-17.

- (153) Leitner, N. K. V.; Berger, P.; Legube, B. Oxidation of amino groups by hydroxyl radicals in relation to the oxidation degree of the alpha-carbon. *Environ. Sci. Technol.* **2002**, *36* (14), 3083-3089.
- (154) Borduas, N.; da Silva, G.; Murphy, J. G.; Abbatt, J. P. D. Experimental and Theoretical Understanding of the Gas Phase Oxidation of Atmospheric Amides with OH Radicals: Kinetics, Products, and Mechanisms. *J. Phys. Chem. A* **2015**, *119* (19), 4298-4308.
- (155) Wan, E. C. H.; Yu, J. Z. Analysis of sugars and sugar polyols in atmospheric aerosols by chloride attachment in liquid chromatography/negative ion electrospray mass spectrometry. *Environ. Sci. Technol.* **2007**, *41* (7), 2459-2466.
- (156) Lam, H. K.; Shum, S. M.; Davies, J. F.; Song, M.; Zuend, A.; Chan, M. N. Effects of inorganic salts on the heterogeneous OH oxidation of organic compounds: insights from methylglutaric acid-ammonium sulfate. *Atmos. Chem. Phys.* **2019**, *19* (14), 9581-9593.

4 Method development and validation of a reverse phase gas chromatographic method (GC-MS) for the simultaneous quantification of saccharides and amides.

4.1 Introduction

Atmospheric aerosol particles are heavily abundant in the atmosphere coming from emissions credited to both anthropogenic and naturogenic activities.^{1,2,10,3-9,9} The particles making the aerosol differ in their physical state (solid or liquid) and vary greatly in physical properties such as size.¹¹⁻¹⁴ However, the chemical composition of the aerosol particles have proven to be the most complex, with atmospheric aerosols having the possibility to contain virtually all compounds known to man in infinite combinations.¹⁵⁻²⁰²¹⁻²³ The influence that these atmospheric aerosols have on the environment and climate has necessitated a hefty investment in research geared at better understanding atmospheric aerosols and any associated processes.^{20,24-26}

In a bid to better understand the chemical composition of atmospheric aerosols several offline and online methods have been developed. The chemical composition of aerosol particles has generally been determined by gas- and liquid-chromatographic techniques, mostly with mass spectrometric detection for both offline and online analysis.^{27,28,37-39,29-36} The analysis of volatile organic compounds in aerosols in terms of detection and quantification has proven to be relatively straightforward. The challenge has been in the analysis of semi-volatile and nonvolatile organic compounds, especially those that also undergo thermal decomposition as opposed to boiling. Previously highlighted references showed that several offline methods that utilize derivatization prior to GC separation have been developed to address this challenge. However, most of the available methods are optimized for looking at a single class of

compounds. The method developed here was successfully optimized to simultaneously detect and quantify different classes of compounds.

The complex nature of the atmosphere makes it more challenging to study atmospheric aerosols and associated chemical processes in their natural environment. To address this challenge most research aimed at understanding atmospheric chemistry has been done in reactors designed to imitate atmospheric processes.⁴⁰⁻⁴⁸ This has necessitated the development of analytical methods specific to the needs of the different experimental setups and their objectives.

In this study, offline methods were developed and validated for the simultaneous detection of amides, urea, and saccharides using GC-MS. The methods borrow from previous methods developed for the analysis of amides⁴⁹⁻⁵² and saccharides⁵³⁻⁵⁵. Precolumn derivatization based on silylation reagents BSA and TMSC was utilized to resolve the problem of low volatility and thermal decomposition. Method development focused on generating a procedure for the analyses of aerosols collected from a flow tube reactor designed to imitate the heterogeneous oxidation of aqueous organic aerosols in the atmosphere. The methods developed focus on the specified analytes partly because of their atmospheric relevance, and primarily because of their significance to the heterogeneous oxidation experiment in chapter 5. However, the methods are flexible and can be applied to the analysis of another compound with similar functional groups that are relevant to atmospheric chemistry.

4.2 Materials and methods

4.2.1 Instrumentation and conditions

Gas chromatographic analyte separation was done using the Trace1310 gas chromatography.

Samples were handled and injected into the trace 1310 GC using the AI 1310 liquid autosampler.

Analyte detection and quantification was done via the use of the ISQ QD single quadrupole mass

spectrometer. The three were coupled and operated using the chameleon software, version 7.

Sample weighing was carried out using a high-precision analytical balance. Water was extracted from samples using the LabCorp lyophilizer.

4.2.1.1 GC-MS conditions

Chromatographic and detection parameters were set and adjusted through a vigorous optimization process. Some of the parameters, such as the mobile phase gas (He), column type (capillary column 150m x 0.25mm I.D, film thickness 0.25 μ m, TS-SQC Thermo), injection conditions (10 μ l syringe, draw speed, and 1 μ l air volume below the sample, injection port temperature 300 °C), ionization technique (EI – 70 eV), MS transfer line temperature (275°C) and scan rate (0.2s), were informed by literature and resource availability and were therefore kept constant throughout the optimization process⁵⁵. The selection of the ion source temperature was done by conducting the detection of all analytes of interest using different ion source temperatures ranging from 200 to 320°C (20°C increments). The ion source temperature giving the highest signal intensity for every analyte of interest was then chosen. The split ratio was determined through a series of trial-and-error experiments, starting with a very high ratio and moving to a lower ratio, until high S/N ratios and good peak shapes were achieved. Parameters such as initial oven temperature, temperature gradient, final temperature, carrier gas flow rate, and injection volume were all tested and adjusted to achieve the best chromatographic resolution. Table 4.1 and Table 4.2 show the optimum operating conditions established for the methods developed here.

4.2.2 Reagents and Chemicals

Propionamide 97% and chlorotrimethylsilane 98% were purchased from ACROS organics. N, O-Bis(trimethylsilyl) acetamide 95% was purchased from Thermo Scientific. D- (+)-xylose 98%,

and pyridine anhydrous 99.5% were purchased from Alfa Aesar. Methyl α -D-glucopyranoside \geq 99% and Glucose 99.5% \geq was purchased from SIGMA.

4.2.2.1 Preparation of Stock solution and calibration Standard solutions

Appropriate amounts of propionamide, MGP, xylose, urea, glucose and acetamide were weighed separately and dissolved in pyridine to give propionamide (0.01mg/ml), MGP (0.01mg/ml), xylose (0.05mg/ml), urea (0.001mg/ml), glucose (0.01mg/ml) and acetamide (0.01mg/ml) stock solutions. Working standards of the analytes were prepared from the stock solution as per need and all calibration standards were prepared in triplicates.

Table 4.1 Instrument optimum operating conditions for the MGP-Urea-Xylose method.

Parameter	Gas Chromatograph	Mass spectrometry
Ion source temperature	-	300
Ionization technique	-	EI
Transfer line temperature	-	275°C
Scan rate	-	0.2s
Start time	-	1.62mins
End time	-	16mins
Full scan	-	50-350 amu
Split ratio	300	-
Pressure	73.8ka	-
Carrier gas	Helium	-
Ionization energy	70.0eV	-
Total flow rate	1	-
Column flow	0.200ml/min	-
Injection volume	1 μ l	-
Injection port temperature	300°C	-
Purge Flow	5ml	-

Table 4.2 Instrument optimum operating conditions for the MGP-Propionamide-Urea method and Propionamide-Urea-MGP method.

Parameter	Gas Chromatograph	Mass spectrometry
Ion source temperature	-	300
Ionization technique	-	EI
Transfer line temperature	-	275°C
Scan rate	-	0.2s
Start time	-	1.62mins
End time	-	16mins
Full scan	-	50-350 amu
Split ratio	50	-
Pressure	73.8ka	-
Carrier gas	Helium	-
Ionization energy	70.0eV	-
Total flow rate	1	-
Column flow	0.200ml/min	-
Injection volume	11µl	-
Injection port temperature	300°C	-
Purge Flow	5ml	-

4.2.3 Aqueous organic aerosol collection and preparation (actual sample)

A 1 to 2mg sample of the aerosol flow was collected by placing a 0.1 micron, 47mm PTFE Laminated Membrane filter in the flow path of the aerosol for 1 to 2hrs. The filter was then removed and placed in a beaker with 5 ml of water and sonicated for 15 mins to extract the sample collected on the filter into the water. The aqueous solution from the sonication was then frozen using liquid nitrogen, before being moved to the lyophilizer to extract out all the water. The dried product from the lyophilizer was then dissolved in pyridine and taken through the silylation step.

4.2.4 Derivatization

Of the three derivatization mechanisms (alkylation, silylation, and acylation) available for GC-MS, silylation was chosen for this method. Silylation was chosen for its ability to readily

volatilize non-volatile compounds and give volatile products, and its ability to volatilize compounds that are considered unstable at high temperatures (200-300°C).⁵⁶⁻⁵⁸

4.2.4.1 BSA Silylation

The samples and standards that contained a mixture of amides, monosaccharides and urea were derivatized using BSA. BSA was used for this application because it is highly reactive towards nitrogen-containing compounds such as amino acids and amides, as well as compounds bearing hydroxyl or carboxyl groups such as methyl α -D-glucopyranose. BSA also requires very mild conditions and gives relatively more stable by-products. The volume of reagent to be used was determined by derivatizing a standard solution containing 1mg each of urea, MGP and propionamide. The volume of solvent tested ranged from 200 to 600 μ l. The optimum reagent volume was then selected based on achieving complete derivatization, the highest possible peak area, and having a satisfying amount of silylation reagent remaining (determined by observing the reagent peak from the full sample chromatographs). To determine the reaction time, a large volume (10ml) of a standard sample containing 1mg/ml of each analyte was heated at a constant temperature for 210mins. Aliquots were then withdrawn from the large volume and analyzed at 30min intervals. For the reaction temperature determination, several 1mg/ml standard solutions were reacted at different temperatures ranging from 40°C to 140°C for a fixed amount of time. Optimum conditions assured complete derivation of the sample with the use of the least possible resources.

4.2.4.2 BSA-TMCS Silylation

The samples and standards that contained a mixture of sugars and urea (MGP-Urea-Xylose method) were derivatized using BSA and TMCS. The TMCS is not a strong silylation agent due to having a poor leaving group, however, TMCS acts as a catalyst in derivatization reactions.

BSA:TMCS(2:1) reagent performance was compared and chosen as the reagent of choice to the well know TMSI:BSA:TMCS (3:3:2) reagent. The volume of reagent to be used was determined by derivatizing a standard solution containing 1mg each of urea, MGP and xylose. The volume of solvent tested ranged from 50 to 250 μ l of BSA and 25 to 125 μ l of TMCS. The optimum reagent volume was then selected based on achieving complete derivatization and having a satisfying amount of silylation reagent remaining (determined by observing the reagent peak from the full sample chromatographs). To determine the reaction time, a large volume(10ml) of a standard sample containing 1mg/ml of each analyte what heated at a constant temperature for 210mins. Aliquots were then withdrawn from the large volume and analyzed at 30min intervals. For the reaction temperature determination, several 1mg/ml standard solutions were reacted at different temperatures ranging from 40°C to 140°C for a fixed amount of time. Optimum conditions assured complete derivation of the sample with the use of the least possible resources.

4.2.5 Preparation of Calibration Curves

Internal standards calibration was used and calibration curves for each individual method were developed. The internal standards approach was used to account for routine variations in the response of the GC-MS system, the volume of sample injected into the chromatographic system(1 μ l), and retention time.

4.2.5.1 Calibration Curves for MGP-Urea-Xylose method: Internal standard xylose

Samples containing different concentrations of MGP and urea ranging from 0-1.2mg/ml and 1mg/ml Xylose were prepared from stock solutions. The chromatograms of the standard samples were obtained, and the peak areas were determined. Calibration curve were prepared by plotting the ratios of analyte peak area to internal standard peak area against ratios of analyte concentration to internal standard concentration, as shown in the results. A second calibration

curve showing the ratios of analyte peak area to internal standard peak area against analyte concentration was also plotted.

4.2.5.2 Calibration Curves for MGP-Propionamide-Urea method: Internal standard urea

Samples containing different concentrations of MGP and Propionamide ranging from 0 - 1.6mg/ml and 0.5mg/ml urea (internal standard), were prepared from standard solution. The chromatograms of the standard samples were obtained, and the peak areas were determined. A calibration curve was prepared by plotting the ratios of analyte peak area to internal standard peak area against ratios of analyte concentration to internal standard concentration, as shown in the results. A second calibration curve showing the ratios of analyte peak area to internal standard peak area against analyte concentration was also plotted.

4.2.5.3 Calibration Curves for Propionamide-Urea-MGP method: Internal standard MGP

Samples containing different concentrations of urea and propionamide ranging from 0-1.0mg/ml and 1mg/ml MGP(internal standard), were prepared from standard solution. The chromatograms of the standard samples were obtained, and the peak areas were determined. A calibration curve was prepared by plotting the ratios of analyte peak area to internal standard peak area against ratios of analyte concentration to internal standard concentration, as shown in the results.

4.3 Method Validation

4.3.1 Specificity

4.3.1.1 Identity

For each analytical method, standards containing 1mg of a single analyte were used to determine Identity specificity. The chromatograms and mass spectra from the analysis of the standard solutions were then compared.

4.3.1.2 Assay Tests

Critical separation of peaks was investigated by calculating the resolution factors of the peaks.

$$R_s = \frac{2(t_{R2} - t_{R1})}{(W_1 + W_2)}$$

$R_s = \text{peak resolution,}$

$W = \text{peak width, } t_R = \text{retention time}$

4.3.2 Precision

4.3.2.1 Repeatability

Repeatability was determined for each analytical method. 15 determinations covering the range of standard prepared were used, 3 concentrations and 5 replicates each. For the MGP-Urea-Xylose method 0.2mg /ml, 0.6mg/ml and 1.2mg/ml standards were used. For the MGP-Propionamide-Urea method 0.1mg /ml, 0.8mg/ml and 1.6mg/ml standards were used. For the Propionamide-Urea-MGP method 0.1mg /ml, 0.8mg/ml and 1.6mg/ml standards were used.

4.3.2.2 Intermediate Precision

Intra- day and inter-day precision for each analytical method were determined. For intra- day precision the standards used for repeatability were analyzed three times on the same day, with the analysis being done at 5hour intervals. For inter-day precision, the same standards were analyzed on three different days. From this data, % RSD was calculated.

4.3.3 Linearity

Linearity was determined for each analytical method. It was assessed through analysis of combined standard solutions in the range of 0.2 – 1.2mg/ml for MGP-Urea-Xylose method, 0.1-1.6mg/ml for MGP-Propionamide-Urea method, and 0.1-1.6mg/ml for Propionamide-Urea-MGP method.

4.3.4 Detection Limit

Two approaches were used to determine the detection limits of each analytical method.

4.3.4.1 Visual Evaluation

To determine the detection limit based on the visual evaluation approach, standards of known low concentrations were analyzed and a minimum concentration at which the analyte can be confidently separated from the blank signal was established.

4.3.4.2 Standard Deviation of the Response and the slope

The detection limit (DL) was calculated for each analytical method from the residual standard deviation of the calibration curve regression line using the following expression:

$$DL = \frac{.3.3\sigma}{S}$$

σ = standard deviation of the response

S = slope of the calibration curve

4.3.5 Quantitation Limit

Two approaches were used to determine the quantification limits of each analytical method.

4.3.5.1 Visual Evaluation

To determine the quantification limit based on the visual evaluation approach, standards of known low concentrations were analyzed and a minimum concentration at which the analyte can be confidently separated from the blank signal was established.

4.3.5.2 Standard Deviation of the Response and the slope

The quantification limit (QL) was calculated for each analytical method from the residual standard deviation of the calibration curve regression line using the following expression:

$$QL = \frac{10\sigma}{S}$$

σ = standard deviation of the response

S = slope of the calibration curve

4.3.6 Robustness

The robustness of the analytical methods was tested by varying two chromatographic conditions, flow rate and temperature, by $\pm 10\%$. The % RSD between the data at each variable condition was then determined.

4.3.7 Accuracy

To determine the accuracy, each analytical method was applied to the analysis of a standard with an analyte of known purity and concentration.

4.4 Results and Discussion

As the study of atmospheric chemistry and the aerosols in the atmosphere has continued it has become apparent that the aerosols in the atmosphere are small chemical reservoirs containing multiple chemical components. This, therefore, implies that anyone seeking to understand aerosols from a chemical perspective would have to have analytical methods capable of detecting and quantifying the various chemical components. The ideal methods would have to be rapid, simple, sensitive, specific, inexpensive, and capable of detecting several compounds simultaneously.

4.4.1 Method Development

4.4.1.1 Optimization of silylation derivatization

Effective derivatization is at the center of the successful quantitative analysis of saccharides, amides, and urea using GC-MS. The samples (imitations of atmospheric multi-component organic aerosols) to be analyzed by these methods are composed of species possessing functional groups (-OH, NH₂) that compete to react with the silylating agent. This competition could lead to

incomplete derivatization of all target analytes, which in turn leads to underestimation of concentration and a lack of precision. For this study, the efficiency of the derivatization was assessed using reaction time, temperature, and derivatization reagent type and quantity. For the MGP-Urea-Xylose method, the TMSI:BSA:TMCS (3:3:2) reagent and BSA:TMSC 3:2 reagents were tested. Both reagents gave satisfactory results as determined by the ability to give unique products for each target analyte, which could be clearly separated by GC-MS. The BSA:TMSC 3:2 reagent was then selected as the reagent of choice on the basis of ease of use. The influence of reaction time, reaction temperature, and reagent volume were then assessed for BSA:TMSC (Figure 4.1).

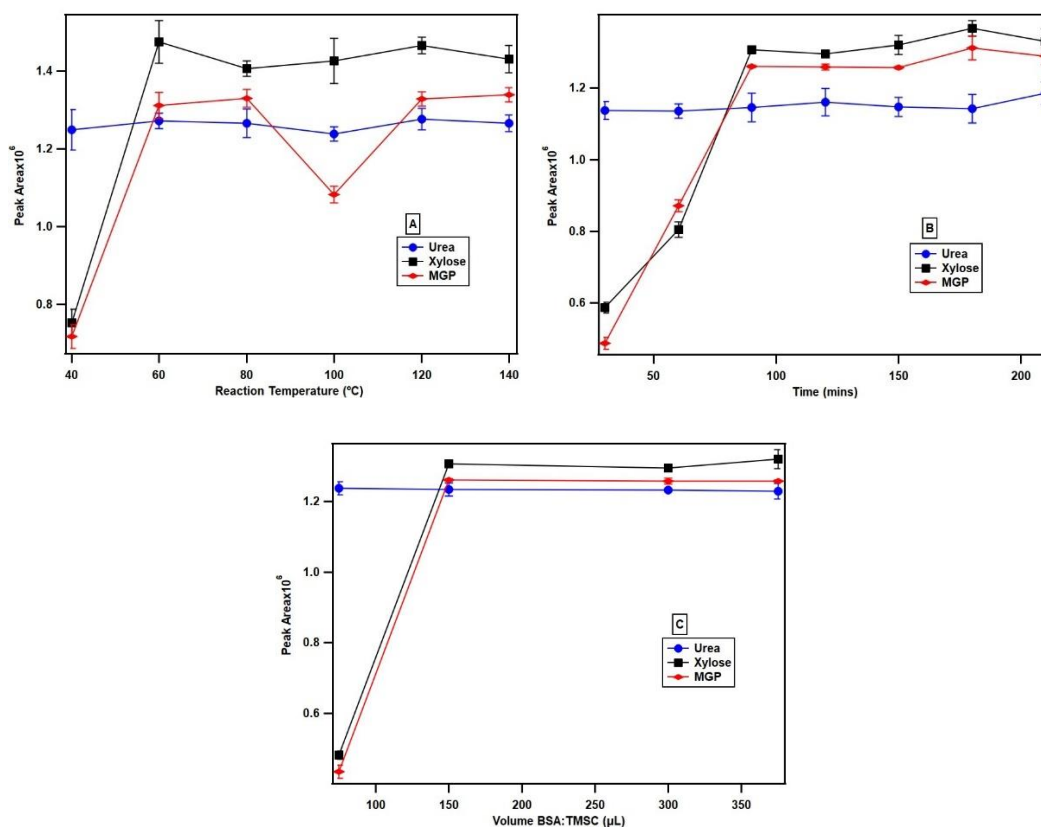


Figure 4.1 Effect of derivatization parameters; A) reaction temperature B) reaction time and C) BSA reagent volume relative to peak area.

The results showed that the complete derivatization of urea and a saccharide using BSA:TMSC 3:2 as the reagent, could be achieved after 60mins of reaction at 60°C and 150µl of reagent. The derivatization extent was not improved by increasing the reagent quantity above 150 µl and heating above 60°C for any analyte. A reaction temperature of 80°C, a reaction time of 90mins, and a reagent volume of 300µl were eventually selected as the derivation conditions. The parameters values settled on were increased to be values in the interpolation range between the first highest signal and the last of graphs in Figure 4.1 to gain some assurance for complete derivation.

For the MGP-Propionamide-Urea method and Propionamide-Urea-MGP method, the BSA:TMSC 3:2 and BSA reagents were tested. BSA:TMSC reagent was not able to derivatize the amide of interest to give products that could be detected by the GC-MS. The BSA reagent was then selected as the reagent of choice based on its ability to give unique products for each target analyte, which could be clearly separated by GC-MS. The influence of reaction time, reaction temperature, and reagent volume were then assessed for BSA (Figure 4.2).

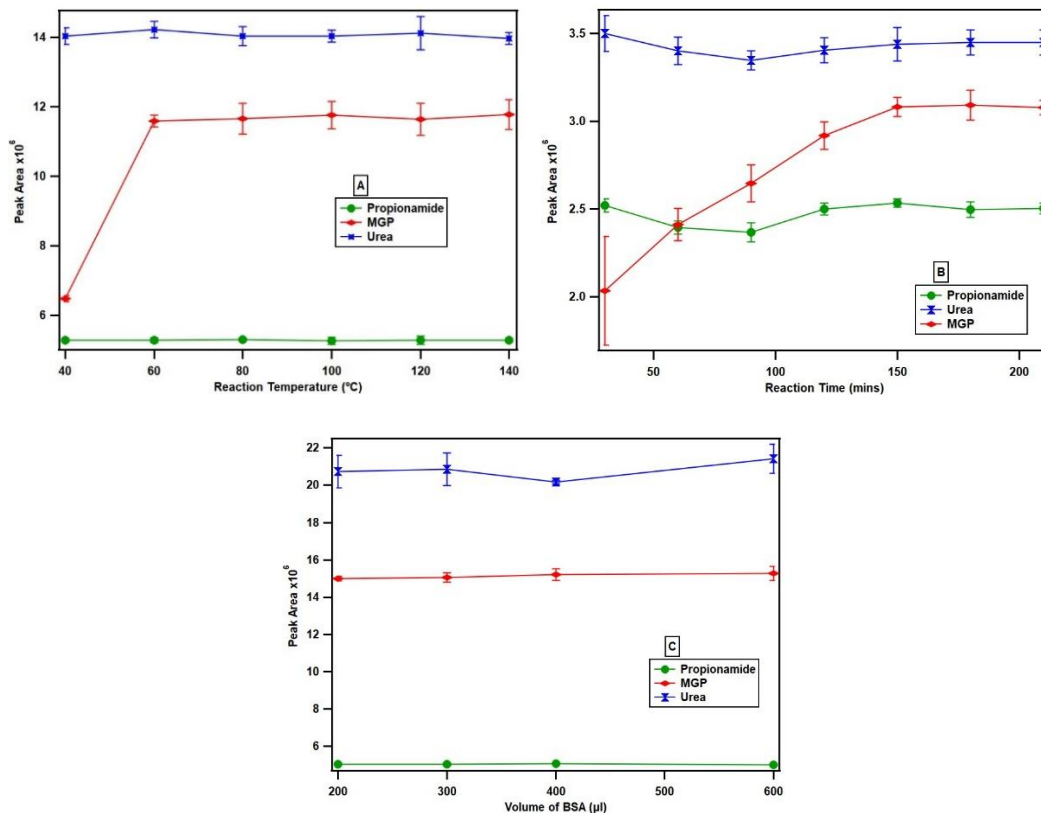


Figure 4.2 Effect of derivatization parameters; A) reaction temperature B) reaction time and C) BSA reagent volume relative to peak area.

The results showed that the complete derivatization of urea, amide, and a saccharide using BSA as the reagent, could be achieved after 150mins of reaction at 60°C and 200 μ l of reagent. The derivatization extent was not improved by increasing the reagent quantity above 200 μ l and for any analyte (Figure 4.2 C). The derivatization extent did not change with increasing reaction time for amide and Urea, while the derivatization extent for MGL stopped improving above 150mins (Figure 4.2 B). A reaction temperature of 80°C, a reaction time of 150mins, and a reagent volume of 300 μ l were eventually selected as the derivation conditions. The parameters values settled on were increased to be values in the interpolation range between the first highest signal and the last of graphs in Figure 4.2 to gain some assurance for complete derivation.

4.4.1.2 Optimization of GC-MS parameters

Without an effective way to separate and detect analytes no quantitative analysis of saccharides, amides, and urea using GC-MS is possible. It becomes of paramount importance to determine the right separation and detection conditions for any analytical method.

To develop a highly sensitive and selective instrument method, the Chromatographic and detection parameters used for the presented methods were set and adjusted through a vigorous optimization process described in the methodology section. Some of the parameters were informed by literature. The results presented below are from measurements performed under optimal operating conditions. These optimal conditions gave the best-shaped, high sensitivity, and good peak separation, while the other tested operating conditions gave either no results or relatively poor chromatograms.

4.4.1.2.1 MGP-Urea-Xylose method

For the MGP-Urea-Xylose method, analytes of interest were successfully separated using a trace 1310 GC under the chromatographic conditions listed in Table 4.1 and a Thermo (capillary column 150m x 0.25mm I.D, film thickness 0.25 μ m, TS-SQC Thermo) capillary column. The qualitative and quantitative detection was achieved using a thermos ISQ QD single quadrupole mass spectrometer under detection conditions also listed in Table 4.1. The ion source temperature was selected to be 300 $^{\circ}$ C from the tested range 200 $^{\circ}$ C to 320 $^{\circ}$ C, the results showed that 300 $^{\circ}$ C gave the highest peak intensities, therefore, implying the highest sensitivity for all analytes. A split ratio of 50 provided a high Signal to noise ratio and satisfactory peak shapes as compared to the other tried ratios. The final oven temperature gradient program settled on for this method was as follows: start at an initial temperature of 40 $^{\circ}$ C holding for 0mins, ramp to 160 $^{\circ}$ C at 30 $^{\circ}$ C/min, then ramp to 170 $^{\circ}$ C at 2 $^{\circ}$ C/min, ramp to 300 $^{\circ}$ C at 30 $^{\circ}$ C/min, and finally hold for 2 min. A solvent delay time of 1.5 min was used. The column was reconditioned at 300 $^{\circ}$ C

for 2 min to eliminate all impurities co-extracted from the matrix and reduce carry-over effects.

A chromatogram of a 1mg/ml urea, xylose, and MGP standard sample is presented in Figure 4.3.

Retention times were 3.0428 and 3.189 mins for the urea peaks (blue), 5.0494, 5.1344, 5.7466, and 6.335mins for the xylose peaks (black), and 8.0185mins for the MGP peak (red).

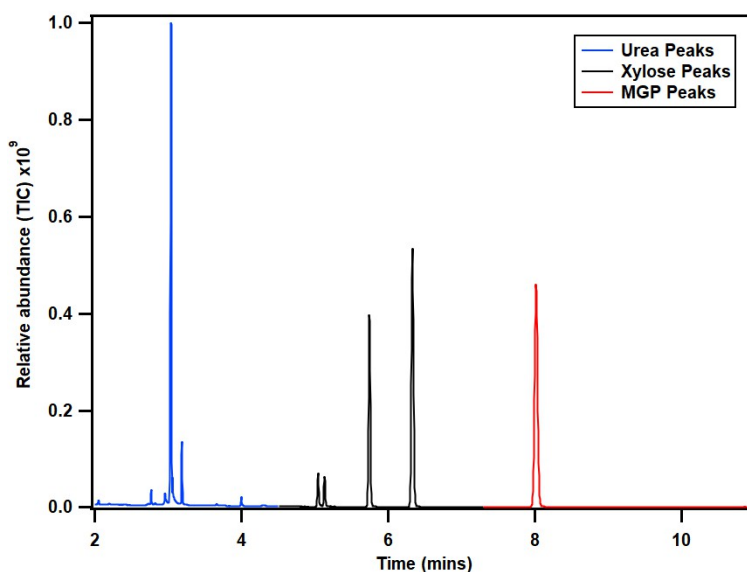


Figure 4.3 The total ion chromatogram (TIC) of an MGP-Urea aerosol sample with xylose as an internal standard. Several peaks were obtained corresponding to the derivatization products of urea (blue), Xylose (black), and MGP (red).

4.4.1.2.2 MGP-Propionamide-Urea method and Propionamide-Urea-MGP method

For the MGP-Propionamide-Urea method and Propionamide-Urea-MGP method, analytes of interest were successfully separated using a trace 1310 GC under the chromatographic conditions listed in Table 4.2 and a Thermo (capillary column 150m x 0.25mm I.D, film thickness 0.25 μ m, TS-SQC Thermo) capillary column. The qualitative and quantitative detection was achieved using a thermos ISQ QD single quadrupole mass spectrometer under detection conditions also listed in Table 4.2. The ion source temperature was selected to be 300°C from the tested range 200°C to 320°C, the results showed that 300°C gave the highest peak intensities, therefore,

implying the highest sensitivity for all analytes. A split ratio of 300 provided a high Signal to noise ratio and satisfactory peak shapes as compared to the other tried ratios. A chromatogram of a 1mg/ml propionamide, urea, and MGP standard sample is presented in Figure 4.4. Retention times for the two analytical methods were 1.7981 and 1.8662mins for the propionamide peaks (green), 2.7675 and 3.1144 mins for the urea peaks(blue) and 6.1923, 6.7841 and 8.0153mins for the MGP peaks(red). Figure 4.4 shows a full chromatogram from the analysis of an MGL-Propionamide sample with urea as the internal Standard.

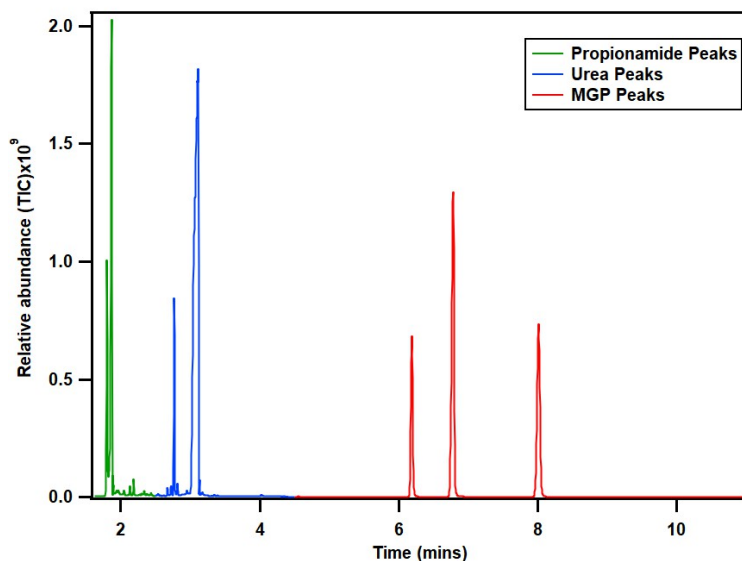


Figure 4.4 The total ion chromatogram (TIC) of an MGP-Propionamide aerosol sample with Urea as an internal standard. Several peaks were obtained corresponding to the derivatization products of propionamide (green), Urea (blue), and MGP (red).

4.4.2 Method Validation

The methods detailed here were validated using several parameters that speak to specificity, precision, accuracy, linearity, and robustness.

4.4.2.1 Specificity

4.4.2.1.1 Identity

The identity specificity of each method was determined as stated in the methodology section.

Figure 4.5, Figure 4.6, and Figure 4.7 display the results of the identity specificity for the MGP-Urea-Xylose method. For the GC-MS conditions described for this method, the three figures show that the derivatization of urea gives products that separate into two product peaks at times 2.760min and 3.0324min, while those of MGP give one peak at 8mins, and those of xylose give 4 peaks at 5.0494, 5.1344, 5.759min, and 6.335mins. The three figures also display the mass spectrum corresponding to all the major peaks and all the products corresponding to the peaks can be distinguished apart with relative ease using the mass spectrum. The data shows that using this method the molecules of interest can be told apart, and the chance of any analyte being mistaken for the others is non-existent. Molecules like the analytes of interest and which are also potential products of the oxidation of the analytes by OH-radical were analyzed and compared. For this method glucose was analyzed and compared to the results of MGP and xylose, it was clear that the three could be clearly distinguished in a mixture containing all three. However, there are peaks that would have very low resolution between MGP and Glucose peaks make quantification challenging

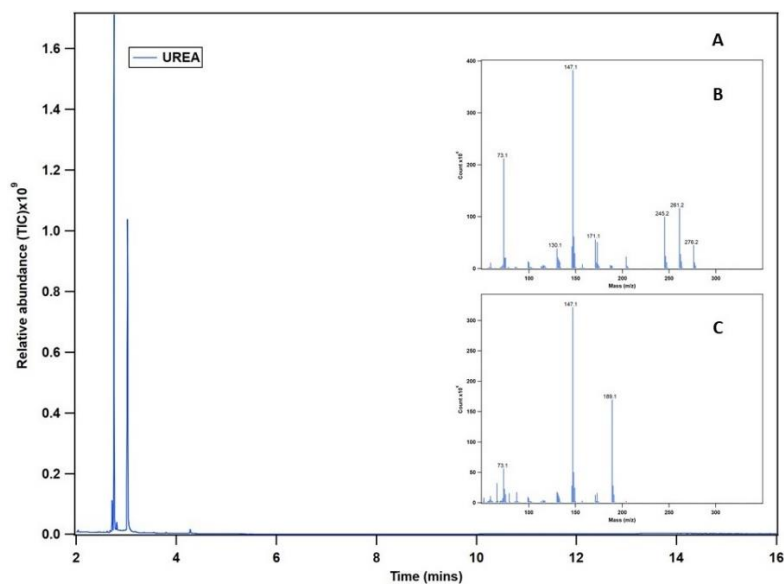


Figure 4.5 The total ion chromatogram (TIC) of a urea standard sample silylated using BSA and TMCS. A) A full chromatogram of the Derivatized Urea standard; B) Mass spectrum of first peak at retention time 2.760min. C) Mass spectrum of second peak at retention time 3.0324min.

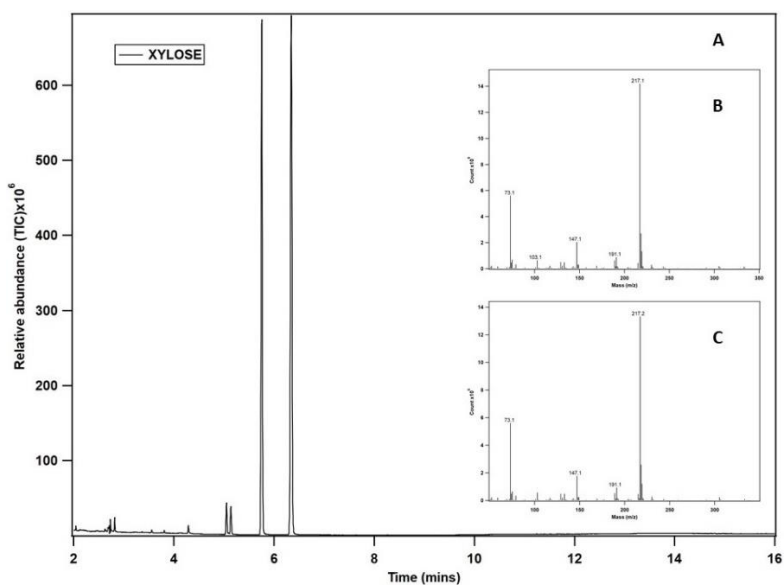


Figure 4.6 The total ion chromatogram (TIC) of a xylose standard sample silylated using BSA and TMCS. A) A full chromatogram of the Derivatized xylose standard; B) Mass spectrum of third peak at retention time 5.759min. C) Mass spectrum of fourth peak at retention time 6.348min

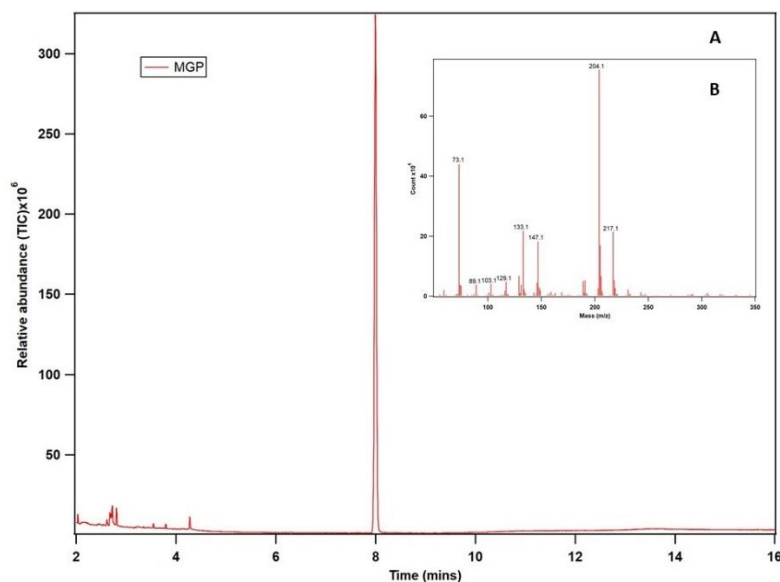


Figure 4.7 The total ion chromatogram (TIC) of a MGP standard sample silylated using BSA and TMCS. A) A full chromatogram of the Derivatized MGP standard; B) Mass spectrum the peak at retention time 7.997min.

Figure 4.8, Figure 4.9, and Figure 4.10 display the results of the identity specificity for the MGP-Propionamide-Urea method and Propionamide-Urea-MGP method. For the GC-MS conditions described for these methods, the three figures show that the derivatization of propionamide gives products that separate into two product peaks at times 1.7981 and 1.8662mins, while those of urea give two peak at 2.7675 and 3.1144 mins, and those of MGP give three peaks at 6.1923, 6.7841 and 8.0153mins. The three figures also display the mass spectrum corresponding to all the major peaks and all the products corresponding to the peaks can be distinguished apart with relative ease using the mass spectrum. The data shows that using these methods the molecules of interest can be told apart, and the chance of any analyte being mistaken for the others is close to non-existent. Molecules similar to the analytes of interest and which are also potential products of the oxidation of the analytes by OH-radical were analyzed and compared. For this method glucose (Figure 4.11) and acetamide were analyzed and compared to the results of propionamide

and MGP. The results show that the method cannot detect acetamide due to BSA not being able to silylate acetamide. The method can detect glucose (Figure 4.11) and MGP(Figure 4.10), but cannot be used to quantify the two analytes in the same sample as some of the peaks coelute.

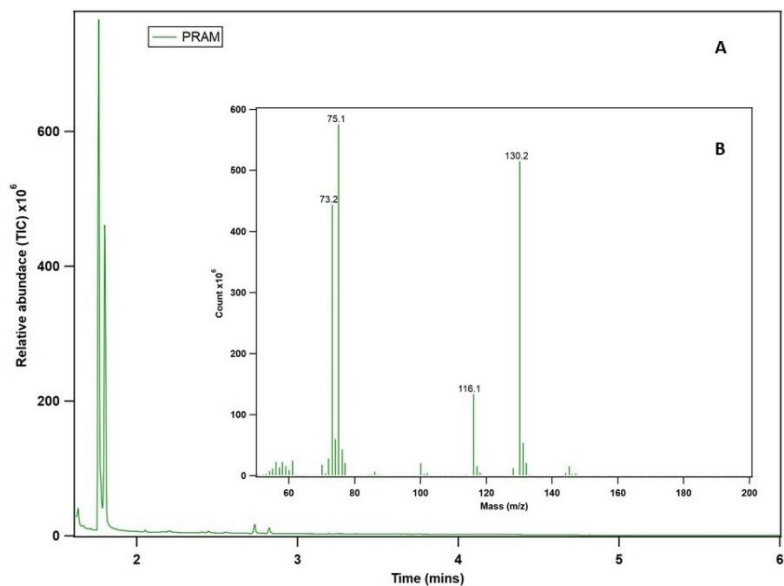


Figure 4.8 The total ion chromatogram (TIC) of a propionamide standard sample silylated using BSA. A) A full chromatogram of the Derivatized propionamide standard; B) Mass spectrum of peak at retention time 1.765min.

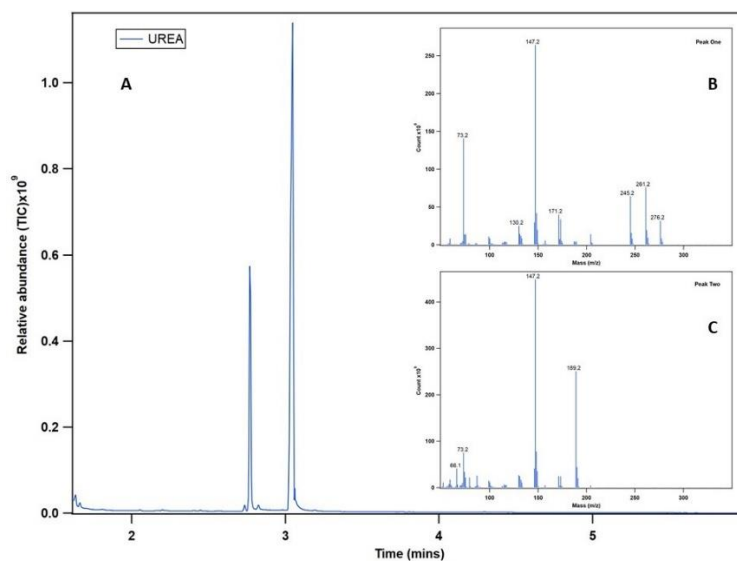


Figure 4.9 The total ion chromatogram (TIC) of a urea standard sample silylated using BSA. A) A full chromatogram of the Derivatized urea standard; B) Mass spectrum of first peak at retention time 2.770min. C) Mass spectrum of second peak at retention time 3.049min.

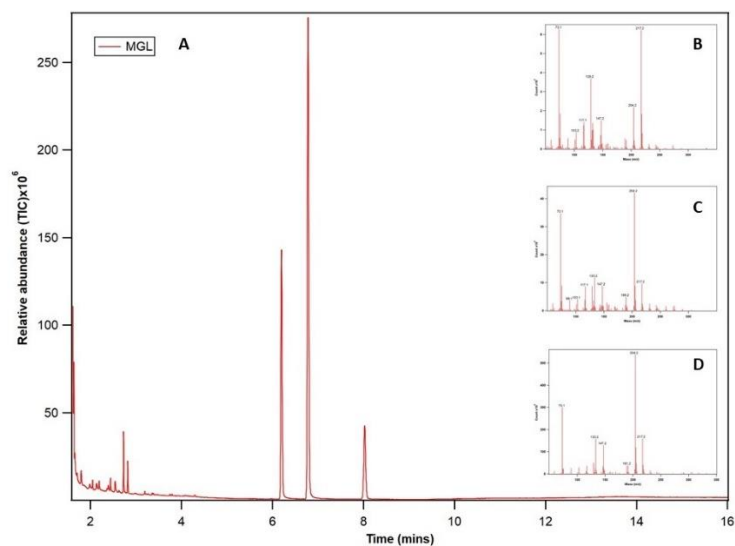


Figure 4.10 The total ion chromatogram (TIC) of an MGP standard sample silylated using BSA. A) A full chromatogram of the derivatized MGP standard; B) Mass spectrum of first peak at retention time 6.202min. C) Mass spectrum of second peak at retention time 6.784min. C) Mass spectrum of third peak at retention time 8.029min.

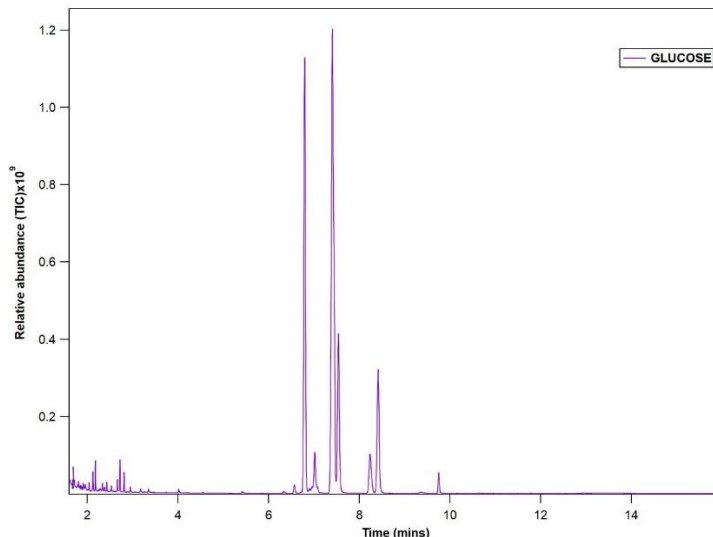


Figure 4.11 The total ion chromatogram (TIC) of a glucose standard sample silylated using BSA.

4.4.2.1.2 Assay Tests

Peak resolutions were determined to further validate the method's ability to clearly separate and identify analytes and to give a quantitative measure to the specificity of the method. Table 4.3 shows the peak resolutions of peaks from the MGP-Urea-Xylose method, while Table 4.4 shows the peak resolutions for the MGP-Propionamide-Urea method and Propionamide-Urea-MGP method. The lowest resolution of all methods are significantly above the acceptable minimum peak resolution (1.5) for regulated analytical procedures.⁵⁹ These results point out to both methods being highly capable of separating the molecules of interest.

Table 4.3 Peak resolutions for MGP-Urea-Xylose method.

	Urea		Xylose				MGP
	Peak 1	Peak 2	Peak1	Peak2	Peak3	Peak4	Only Peak
Retention Time	3.041	3.190	5.049	5.137	5.748	6.336	8.022
Width (mins)	0.030	0.022	0.033	0.036	0.044	0.054	0.076
Resolution	5.740	67.974	2.551	15.444	12.066		25.932

Table 4.4 Peak resolutions for MGP-Propionamide-Urea method and Propionamide-Urea-MGP method

	Propionamide		Urea		MGP		
	Peak 1	Peak 2	Peak1	Peak2	Peak1	Peak2	Peak3
Retention Time	1.797	1.864	2.768	3.084	6.190	6.781	8.015
Width (mins)	0.020	0.032	0.021	0.124	0.05	0.065	0.077
Resolution	2.560	34.323	4.384	35.640	10.208		17.404

4.4.2.2 Precision

4.4.2.2.1 Repeatability

The repeatability of each method was determined as described in the methodology section. Table 4.5 shows the standard samples used to determine the repeatability of the MGP-Urea-Xylose method and the %RSD. The %RSD for all analytes fall below 2% indicating that the method is highly reproducible. The repeatability for the three analytes was not affected by the concentration level.

Table 4. 5 Repeatability calculations for MGP-Urea-Xylose method.

Repeatability	Concentration (mg/ml)	Mean (n=5) Ratio of Areas	SD	%RSD
Urea	0.2	0.12386	0.00170	1.37
	0.6	0.46147	0.00602	1.30
	1.2	1.0208	0.01143	1.12
Xylose	1.0	(Area) 1405751	20279	1.44
MGP	0.2	0.14451	0.00298	2.06
	0.6	0.50285	0.00341	0.68
	1.2	1.09148	0.009794	0.90

Table 4.6 shows the standard samples used to determine the repeatability of the MGP-Propionamide-Urea method and Propionamide-Urea-MGP method, and the %RSD. The %RSD for all analytes fall below 2% indicating that the method is highly reproducible. The repeatability for the three analytes was not affected by the concentration level.

4.4.2.2.2 Intermediate Precision

The intermediate precision was determined as described in the methodology section. Table 4.7 shows the standard samples used to determine the repeatability of the MGP-Urea-Xylose method and the %RSD. The %RSD for all analytes at given concentrations goes above 2% indicating that the method loses precision over the 72-hour period. The loss of precision is due to the degradation of the derivatization products. These results and the intraday low RSD (below 2%) obtained for intra-day precision led to the conclusion that all prepared samples should be analyzed within 24 hours of being prepared.

Table 4.6 Repeatability calculations for MGP-Propionamide-Urea method and Propionamide-Urea-MGP method.

Repeatability	Concentration (mg/ml)	Mean (n=5) Ratio of Areas	SD	%RSD
Propionamide	0.1	0.05924412	0.000480548	0.81
	0.8	0.453043585	0.006295163	1.39
	1.6	0.830965	0.009562603	1.15
Urea		(Area)		
	0.5	22671165.8	193236.1628	0.85
	1.0	41974843.7	814680.8527	1.94
MGP	0.1	0.08393971	0.001407062	1.68
	0.8	1.173717565	0.012060518	1.03
	1.6	2.161978229	0.025326	1.17

Table 4.8 shows the standard samples used to determine the repeatability of MGP-Propionamide-Urea method and Propionamide-Urea-MGP method, and the %RSD. The %RSD for all analytes at given concentrations goes above 2% indicating that the method loses precision over the 72-hour period. The loss of precision is due to the degradation of the derivatization products. These results and the intraday low RSD (below 2%) obtained for intra-day precision led to the conclusion that all prepared samples should be analyzed within 24 hours of being prepared.

Table 4.7 Inter-day precision calculations for MGP-Urea-Xylose method.

Inter- day	Concentration (mg/ml)	Mean (n=15) Ratio of Areas	SD	%RSD
Urea	0.2	0.12526	0.00787	6.29
	0.6	0.45146	0.02356	5.22
	1.2	1.09955	0.02574	2.34
Xylose	1.0	(area) 1421939.858	40973.46	2.88
MGP	0.2	0.14410	0.00726	5.04
	0.6	0.53864	0.01340	2.49
	1.2	1.1159	0.019794	1.77

Table 4.8 Inter-day precision calculations for for MGP-Propionamide-Urea method and Propionamide-Urea-MGP method.

Inter- day	Concentration (mg/ml)	Mean (n=15) Ratio of Areas	SD	%RSD
Propionamide	0.1	0.058352316	0.003261816	5.59
	0.8	0.45942477	0.011756486	2.56
	1.6	0.827099519	0.013107641	1.58
Urea	0.5	(Area) 22631211.7	294464.0112	1.30
	1.0			
MGP	0.1	0.082870102	0.001598011	1.93
	0.8	1.171162188	0.013931066	1.19
	1.6	2.16862541	0.072934563	3.36

4.4.2.3 Calibration Curves, Linearity, Range, L.O.D and L.O.Q

The calibration range for the MGP-Urea-Xylose method was determined using solutions starting from 0.2mg/ml to 1.2mg/ml. The linearity was assessed by plotting calibration curves shown in Figure 4.12 and determining the regression coefficients, reported in Table 4.9. The L.O.D and the L.O.Q of the method were determined and presented in Table 4.10 and 4.11 respectively.

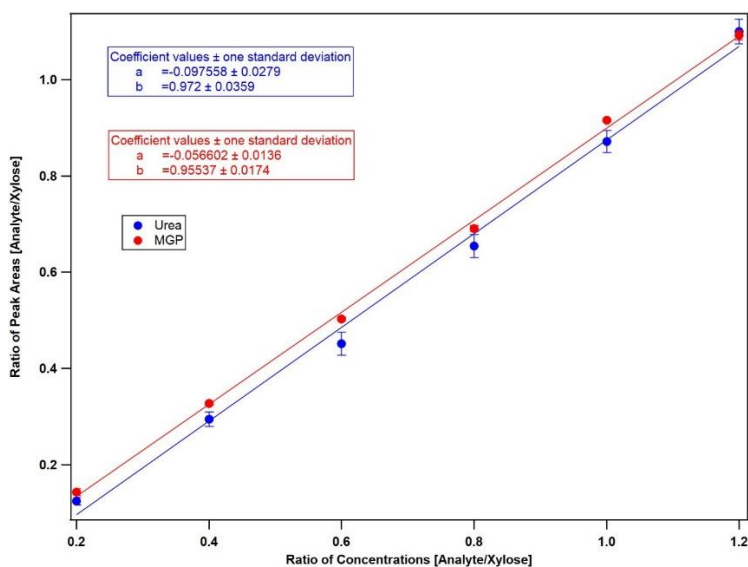


Figure 4.12 Standard calibration curve for MGP(red) and urea(blue) obtained for the MGP-Urea-Xylose method. The coefficients a and b represent the y-intercept and the slope respectively.

Table 4.9 linearity and range for MGP-Urea-Xylose method.

	Linearity and range	Regression Coefficient	Slope	Intercept
Urea	0.1-1.2mg/ml	0.997	0.972	-0.096
MGL	0.1-1.2mg/ml	0.999	0.955	-0.057

Table 4.10 L.O.D MGP-Urea-Xylose method.

L.O.D	Visual Evaluation	SD of regression line
Urea	0.05mg/ml	0.095
MGL	0.05mg/ml	0.047

Table 4. 11 L.O.Q MGP-Urea-Xylose method.

L.O.Q	Visual Evaluation	SD of regression line
Urea	0.05mg/ml	0.287
MGL	0.05mg/ml	0.142

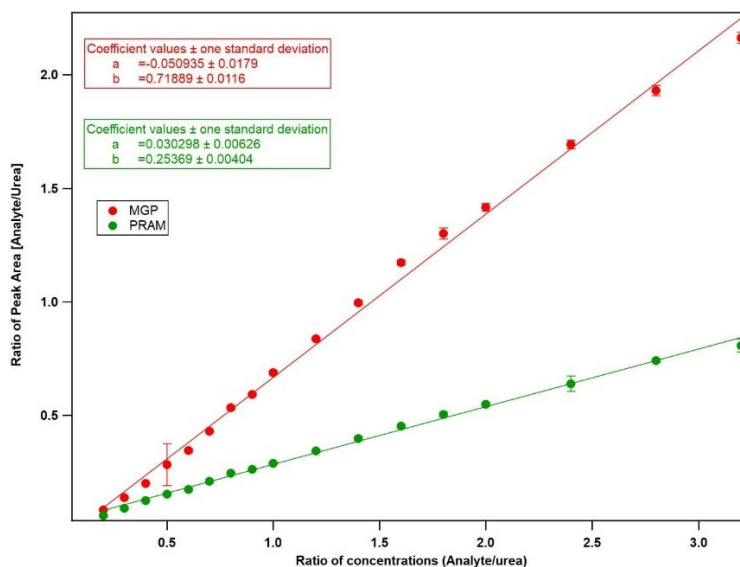


Figure 4.13 Standard calibration curve for propionamide(green) and MGP(red) obtained for the MGP-Propionamide-Urea method. The coefficients a and b represent the y-intercept and the slope respectively.

Table 4.12 linearity and range for MGP-Propionamide-Urea method.

	Linearity and range	Regression Coefficient	Slope	Intercept
Pram	0.1-1.6mg/ml	0.998	0.254	0.030
MGL	0.1-1.6mg/ml	0.998	0.719	-0.051

Table 4.13 L.O.D for MGP-Propionamide-Urea method.

L.O.D	Visual Evaluation	SD of regression line
Pram	0.02mg/ml	0.081
MGL	0.02mg/ml	0.082

Table 4.14 L.O.Q for MGP-Propionamide-Urea method.

L.O.Q	Visual Evaluation	SD of regression line
Pram	0.03mg/ml	0.247
MGL	0.03mg/ml	0.249

The calibration range for the MGP-Propionamide-Urea method was determined using solutions starting from 0.1mg/ml to 1.6mg/ml. The linearity was assessed by plotting calibration curves shown in Figure 4.13 and determining the regression coefficients, reported in Table 4.12. The L.O.D and the L.O.Q of the method were determined and presented in Table 4.13 and 4.14 respectively.

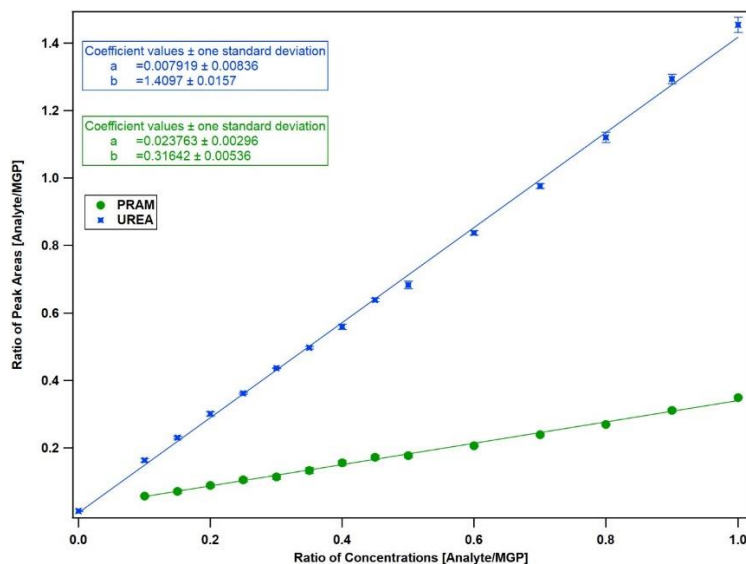


Figure 4.14 Standard calibration curve for propionamide (green) and urea (blue) obtained for the Propionamide-Urea-MGP method. The coefficients a and b represent the y-intercept and the slope respectively.

Table 4.15 linearity and range for Propionamide-Urea-MGP.

	Linearity and range	Regression Coefficient	Slope	Intercept
Pram	0.1-1.0 mg/ml	0.999	0.316	0.024
Urea	0.1-1.0 mg/ml	0.998	1.41	0.008

Table 4.16 L.O.D for Propionamide-Urea-MGP.

L.O.D	Visual Evaluation	SD of regression line
Pram	0.02 mg/ml	0.031
Urea	0.02mg/ml	0.020

Table 4.17 L.O.Q for Propionamide-Urea-MGP.

L.O.Q	Visual Evaluation	SD of regression line
Pram	0.03mg/ml	0.094
Urea	0.03mg/ml	0.059

The calibration range for the Propionamide-Urea-MGP method was determined using solutions starting from 0.1mg/ml to 1.0mg/ml. The linearity was assessed by plotting calibration curves shown in Figure 4.14 and determining the regression coefficients, reported in Table 4.15. The L.O.D and the L.O.Q of the method were determined and presented in Table 4.16 and 4.17 respectively.

The results show that the limits of detection greatly depends on the method used to determine the value. All the results confirm that the methods developed here can be used for the quantitative analysis of sample containing amides, urea, and saccharides.

4.4.3 Analysis of a real sample

Several samples of aqueous organic aerosols were collected from a flow tube reactor as described in the methodology section. The samples were collected after being subjects to varying degrees of OH exposure. The samples where then analyzed following the methods developed here. The analytes of interest were successfully detected and quantified. The concentration of the analytes detected was observed to decrease with increasing OH exposure.

4.5 Conclusion

Analytical methods suitable for the offline simultaneous detection of monosaccharides, urea, and amides in aqueous organic aerosols has been developed successful. The use of internal standards in the methods preserve the high analytical quality of the methods. The method validations prove the methods are capable and accurate.

Application of the methods to the real samples showed no challenges such as coelution or unidentified species. The method is best suited for the analysis of samples from the flow tube reactor, however with slight alterations it can be expanded to be used for other analysis.

Reference

1. Boulon J, Sellegri K, Hervo M, Laj P. Observations of nucleation of new particles in a volcanic plume. *Proc Natl Acad Sci U S A*. 2011;108(30):12223-12226.
doi:10.1073/pnas.1104923108
2. Putaud JP, Van Dingenen R, Alastuey A, et al. A European aerosol phenomenology - 3: Physical and chemical characteristics of particulate matter from 60 rural, urban, and kerbside sites across Europe. *Atmos Environ*. 2010;44(10):1308-1320.
doi:10.1016/j.atmosenv.2009.12.011
3. Rönkkö T, Lähde T, Heikkilä J, et al. Effects of gaseous sulphuric acid on diesel exhaust nanoparticle formation and characteristics. *Environ Sci Technol*. 2013;47(20):11882-11889. doi:10.1021/es402354y
4. Hu S, Fruin S, Kozawa K, Mara S, Paulson SE, Winer AM. A wide area of air pollutant impact downwind of a freeway during pre-sunrise hours. *Atmos Environ*. 2009;43(16):2541-2549. doi:10.1016/j.atmosenv.2009.02.033
5. Pey J, Querol X, Alastuey A, Rodríguez S, Putaud JP, Van Dingenen R. Source apportionment of urban fine and ultra-fine particle number concentration in a Western Mediterranean city. *Atmos Environ*. 2009;43(29):4407-4415.
doi:10.1016/j.atmosenv.2009.05.024
6. Levin Z, Cotton WR. *Aerosol Pollution Impact on Precipitation: A Scientific Review*.; 2009. doi:10.1007/978-1-4020-8690-8
7. Bauer SE, Tsigaridis K, Miller R. Significant atmospheric aerosol pollution caused by world food cultivation. *Geophys Res Lett*. 2016;43(10):5394-5400.
doi:10.1002/2016GL068354

8. Nascimento JP, Bela MM, Meller BB, et al. Aerosols from anthropogenic and biogenic sources and their interactions-modeling aerosol formation, optical properties, and impacts over the central Amazon basin. *Atmos Chem Phys*. 2021;21(9):6755-6779.
doi:10.5194/acp-21-6755-2021
9. Viana M, Pey J, Querol X, Alastuey A, de Leeuw F, Lükewille A. Natural sources of atmospheric aerosols influencing air quality across Europe. *Sci Total Environ*. 2014;472:825-833. doi:10.1016/j.scitotenv.2013.11.140
10. Tomasi C, Lupi A. Primary and Secondary Sources of Atmospheric Aerosol. In: ; 2016:1-86. doi:10.1002/9783527336449.ch1
11. Barrie LA. International Glaciological Society ATMOSPHERIC PARTICLES : THEIR PHYSICAL AND CHEMICAL CHARACTERISTICS , AND DEPOSITION PROCESSES RELEVANT TO THE. *Ann Glaciol*. Published online 1985:100-108.
12. Hughes LS, Allen JO, Kleeman MJ, et al. Size and composition distribution of atmospheric particles in Southern California. *Environ Sci Technol*. 1999;33(20):3506-3515. doi:10.1021/es980884a
13. Boyer HC, Dutcher CS. Atmospheric Aqueous Aerosol Surface Tensions: Isotherm-Based Modeling and Biphasic Microfluidic Measurements. *J Phys Chem A*. 2017;121(25):4733-4742. doi:10.1021/acs.jpca.7b03189
14. Huang Y, Mahrt F, Xu S, Shiraiwa M, Zuend A, Bertram AK. Coexistence of three liquid phases in individual atmospheric aerosol particles. *Proc Natl Acad Sci U S A*. 2021;118(16). doi:10.1073/pnas.2102512118
15. S K, K T, Saarnio K, et al. Chemical composition of atmospheric aerosols between Moscow and Vladivostok. *Atmos Chem Phys Discuss*. 2007;7. doi:10.5194/acpd-7-7473-

2007

16. Pio CA, Legrand M, Alves CA, et al. Chemical composition of atmospheric aerosols during the 2003 summer intense forest fire period. *Atmos Environ.* 2008;42(32):7530-7543. doi:10.1016/j.atmosenv.2008.05.032
17. Moschos V, Schmale J, Aas W, et al. Elucidating the present-day chemical composition, seasonality and source regions of climate-relevant aerosols across the Arctic land surface. *Environ Res Lett.* 2022;17(3). doi:10.1088/1748-9326/ac444b
18. Tomlin JM, Weis J, Veghte DP, et al. Chemical composition and morphological analysis of atmospheric particles from an intensive bonfire burning festival. *Environ Sci Atmos.* 2022;2(4):616-633. doi:10.1039/d2ea00037g
19. Parshintsev J, Hartonen K, Riekkola ML. Chapter 24 - Environmental analysis: Atmospheric samples. In: Fanali S, Haddad PR, Poole CF, Riekkola ML, eds. *Liquid Chromatography (Second Edition)*. Second Edi. Elsevier; 2017:769-798. doi:https://doi.org/10.1016/B978-0-12-805392-8.00024-4
20. Ouafou-Leumbe MR, Galy-Lacaux C, Liousse C, et al. Chemical composition and sources of atmospheric aerosols at Djougou (Benin). *Meteorol Atmos Phys.* 2018;130(5):591-609. doi:10.1007/s00703-017-0538-5
21. Theodosi C, Panagiotopoulos C, Nouara A, et al. Sugars in atmospheric aerosols over the Eastern Mediterranean. *Prog Oceanogr.* 2018;163:70-81. doi:https://doi.org/10.1016/j.pocean.2017.09.001
22. Verma SK, Kawamura K, Chen J, Fu P. Thirteen years of observations on primary sugars and sugar alcohols over remote Chichijima Island in the western North Pacific. *Atmos Chem Phys.* 2018;18(1):81-101. doi:10.5194/acp-18-81-2018

23. Scaramboni C, Urban RC, Lima-Souza M, et al. Total sugars in atmospheric aerosols: An alternative tracer for biomass burning. *Atmos Environ.* 2015;100:185-192.
doi:<https://doi.org/10.1016/j.atmosenv.2014.11.003>
24. Pöschl U. Atmospheric aerosols: composition, transformation, climate and health effects. *Angew Chem Int Ed Engl.* 2005;44(46):7520-7540. doi:10.1002/anie.200501122
25. Zhang B. The Effect of Aerosols to Climate Change and Society. *J Geosci Environ Prot.* 2020;08(08):55-78. doi:10.4236/gep.2020.88006
26. Tomasi C, Fuzzi S, Kokhanovsky AA. Atmospheric Aerosols: Life Cycles and Effects on Air Quality and Climate. In: ; 2017.
27. Claeys M, Vermeylen R, Yasmeeen F, et al. Chemical characterisation of humic-like substances from urban, rural and tropical biomass burning environments using liquid chromatography with UV/vis photodiode array detection and electrospray ionisation mass spectrometry. *Environ Chem.* 2012;9(3):273-284. doi:10.1071/EN11163
28. Mashayekhy Rad F, Zurita J, Gilles P, et al. Measurements of Atmospheric Proteinaceous Aerosol in the Arctic Using a Selective UHPLC/ESI-MS/MS Strategy. *J Am Soc Mass Spectrom.* 2019;30(1):161-173. doi:10.1007/s13361-018-2009-8
29. Grace DN, Sebold MB, Galloway MM. Separation and detection of aqueous atmospheric aerosol mimics using supercritical fluid chromatography-mass spectrometry. *Atmos Meas Tech.* 2019;12(7):3841-3851. doi:10.5194/amt-12-3841-2019
30. Laskin A, Laskin J, Nizkorodov SA. Mass spectrometric approaches for chemical characterisation of atmospheric aerosols: Critical review of the most recent advances. *Environ Chem.* 2012;9(3):163-189. doi:10.1071/EN12052
31. Johnston M V., Kerecman DE. Molecular Characterization of Atmospheric Organic

- Aerosol by Mass Spectrometry. *Annu Rev Anal Chem.* 2019;12:247-274.
doi:10.1146/annurev-anchem-061516-045135
32. Winterhalter R, Van Dingenen R, Larsen BR, Jensen NR, Hjorth J. LC-MS analysis of aerosol particles from the oxidation of α -pinene by ozone and OH-radicals. *Atmos Chem Phys Discuss.* 2003;3(1):1-39.
 33. Sengupta D, Samburova V, Bhattarai C, Watts AC, Moosmüller H, Khlystov AY. Polar semivolatile organic compounds in biomass-burning emissions and their chemical transformations during aging in an oxidation flow reactor. *Atmos Chem Phys.* 2020;20(13):8227-8250. doi:10.5194/acp-20-8227-2020
 34. Sheesley RJ, Mieritz M, DeMinter JT, Shelton BR, Schauer JJ. Technical note. *Atmos Environ.* 2015;123(PA):251-255. doi:10.1016/j.atmosenv.2015.10.047
 35. Sheesley RJ, Deminter JT, Meiritz M, Snyder DC, Schauer JJ. Temporal trends in motor vehicle and secondary organic tracers using in situ methylation thermal desorption GCMS. *Environ Sci Technol.* 2010;44(24):9398-9404. doi:10.1021/es102301t
 36. Mologousi AI, Bakeas EB. Multivariate optimization of a simple and sensitive method for the determination of secondary biogenic organic compounds in airborne particles. *Anal Methods.* 2016;8(20):4047-4055. doi:10.1039/C5AY02758F
 37. Zhao Y, Kreisberg NM, Worton DR, Teng AP, Hering S V., Goldstein AH. Development of an in situ thermal desorption gas chromatography instrument for quantifying atmospheric semi-volatile organic compounds. *Aerosol Sci Technol.* 2013;47(3):258-266. doi:10.1080/02786826.2012.747673
 38. Chan AWH, Kreisberg NM, Hohaus T, et al. Speciated measurements of semivolatile and intermediate volatility organic compounds (S/IVOCs) in a pine forest during BEACHON-

- RoMBAS 2011. *Atmos Chem Phys*. 2016;16(2):1187-1205. doi:10.5194/acp-16-1187-2016
39. Zhang Y, Williams BJ, Goldstein AH, Docherty K, Ulbrich IM, Jimenez JL. A technique for rapid gas chromatography analysis applied to ambient organic aerosol measurements from the thermal desorption aerosol gas chromatograph (TAG). *Aerosol Sci Technol*. 2014;48(11):1166-1182. doi:10.1080/02786826.2014.967832
40. Peng Z, Jimenez JL. Radical chemistry in oxidation flow reactors for atmospheric chemistry research. *Chem Soc Rev*. 2020;49(9):2570-2616. doi:10.1039/c9cs00766k
41. Hidy GM. Atmospheric chemistry in a box or a bag. *Atmosphere (Basel)*. 2019;10(7). doi:10.3390/atmos10070401
42. Dobson CM, Ellison GB, Tuck AF, Vaida V. Atmospheric aerosols as prebiotic chemical reactors. *Proc Natl Acad Sci U S A*. 2000;97(22):11864-11868. doi:10.1073/pnas.200366897
43. Peng Z, Day DA, Ortega AM, et al. Non-OH chemistry in oxidation flow reactors for the study of atmospheric chemistry systematically examined by modeling. *Atmos Chem Phys*. 2016;16(7):4283-4305. doi:10.5194/acp-16-4283-2016
44. Xu N, Collins DR. Design and characterization of a new oxidation flow reactor for laboratory and long-term ambient studies. *Atmos Meas Tech*. 2021;14(4):2891-2906. doi:10.5194/amt-14-2891-2021
45. Fomete SKW, Johnson JS, Casalnuovo D, Jen CN. A tutorial guide on new particle formation experiments using a laminar flow reactor. *J Aerosol Sci*. 2021;157(March):105808. doi:10.1016/j.jaerosci.2021.105808
46. Pereira KL, Rovelli G, Song YC, Mayhew AW, Reid JP, Hamilton JF. *A New Aerosol*

- Flow Reactor to Study Secondary Organic Aerosol*. Vol 12.; 2019. doi:10.5194/amt-12-4519-2019
47. Li R, Palm BB, Ortega AM, et al. Modeling the radical chemistry in an oxidation flow reactor: Radical formation and recycling, sensitivities, and the OH exposure estimation equation. *J Phys Chem A*. 2015;119(19):4418-4432. doi:10.1021/jp509534k
 48. Lambe AT, Ahern AT, Williams LR, et al. Characterization of aerosol photooxidation flow reactors: Heterogeneous oxidation, secondary organic aerosol formation and cloud condensation nuclei activity measurements. *Atmos Meas Tech*. 2011;4(3):445-461. doi:10.5194/amt-4-445-2011
 49. Vismeh R, Haddad D, Moore J, et al. Exposure Assessment of Acetamide in Milk, Beef, and Coffee Using Xanthidrol Derivatization and Gas Chromatography/Mass Spectrometry. *J Agric Food Chem*. 2018;66(1):298-305. doi:10.1021/acs.jafc.7b02229
 50. GC-MS Approaches to the Analysis of Acrylamide. Published online 2003.
 51. Salem AA. Analysis of some chlorophenoxy acids and carbamate herbicides in water and soil as amide derivatives using gas chromatography-mass spectrometry. *J Chromatogr Sci*. 2007;45(3):131-139. doi:10.1093/chromsci/45.3.131
 52. Walla D, Hudson R. Analytical and Applied Pyrolysis, I (1985) 231-247 Elsevier Science Publishers B.V., Amsterdam - Printed in The Netherlands 231. Published online 1985:231-247.
 53. Walford SN. GC-MS as a tool for carbohydrate analysis in a research environment. *Proc Int Soc Sugar Cane Technol*. 2010;27:1-15.
<http://members.issct.org/prozone/docs/Proceedings/2010>, XXVII ISSCT Congress, Veracruz, Mexico/2010 Walford, GC-MS AS A TOOL FOR CARBOHYDRATE

54. Choi NR, Yoon YJ, Park KT, et al. Trace Level Determination of Saccharides in Pristine Marine Aerosols by Gas Chromatography-Tandem Mass Spectrometry. *Toxics*. 2021;9(4). doi:10.3390/toxics9040086
55. Boubou Cisse, Stephane Luchini JPM. To cite this version : *Rev Teledetect*. 2006;8(1):17-34.
56. Orata F. Derivatization Reactions and Reagents for Gas Chromatography Analysis. *Adv Gas Chromatogr - Prog Agric Biomed Ind Appl*. Published online 2012. doi:10.5772/33098
57. Lin DL, Wang SM, Wu CH, Chen BG, Liu RH. Chemical derivatization for the analysis of drugs by GC-MS - A conceptual review. *J Food Drug Anal*. 2008;16(1):1-10. doi:10.38212/2224-6614.2373
58. Fluka Analytical, Supelco. Derivatization Reagents For Selective Response and Detection in Complex Matrices Serving the Analytical World through Innovation , Quality and Leadership. *Supelco*. Published online 2016.
59. Webster GK, Diaz AR, Seibert DS, Weekley BS, Jackson JD. Plate number requirements for establishing method suitability. *J Chromatogr Sci*. 2005;43(2):67-72. doi:10.1093/chromsci/43.2.67

5 Heterogeneous oxidation of multi-component aqueous organic aerosols: The effect of transport phenomena and reaction compartment on reaction kinetics.

5.1 Introduction

In a previous study¹, we looked at the heterogeneous oxidation of aqueous aerosol particles composed of methyl β -D-glucopyranoside (MGP)-only, lactose-only, and any equimolar mixture of lactose and MGP by OH radicals. The kinetic results showed that the reactivity (as demonstrated by uptake coefficient and reaction rate) of lactose towards OH radicals was reduced in the presence of MGP. In the absence of significant quantities of MGP, the reactive uptake coefficient of lactose goes as high as $10.6(\pm 4.0)$. The lactose-only particles also showed that the rate of reaction of the lactose with OH radicals reduced as the reaction proceeded due to the formation of glucose (one of the products of lactose oxidation). The decay of lactose starts with an initial rate coefficient of $13(\pm 5) \times 10^{-12} \text{ cm}^3 \text{ s}^{-1}$, which then falls to $3.0(\pm 1.0) \times 10^{-13} \text{ cm}^3 \text{ s}^{-1}$ as oxidation continues. We explain this observation as being caused by the partitioning difference between Lactose and the other competing particle bulk reactants glucose and MGP. We demonstrate the partitioning difference quantitatively by calculating the $\Delta_p G^o$ of partitioning. We also demonstrate the partitioning difference qualitatively and quantitatively using MD simulation. From this study several questions emerged that required us to investigate: the influence of one solute type on the chemical and physical processes of another solute in a multi-component aqueous aerosol particle, and the influence of partitioning ability on the oxidation of a solute in an aqueous organic particle. The MD simulation done for this earlier study did not also address intramolecular interactions between the solutes, solutes to solvent, solvent to OH radicals, and solutes to OH radicals. The mentioned computational shortfalls were

addressed in a later study presented, in chapter 3 of this thesis, to get a better understanding of the effect of surface-bulk partitioning on Heterogenous chemistry.

The partitioning of molecules at the interface not only affects the chemistry of the solutes in the particle but also affect the physical properties of the particle such as size.²⁻⁴ Surface active molecule greatly reduces the surface tension of the aqueous particles therefore leading to formation of smaller particles.⁵⁻⁷ This affects the capability of the particles to participate as nucleation sites and most likely impacts on the uptake of the gas-phase reactants.^{8,9} Numerous studies of OH radical reacting with different organic species in bulk solution have been conducted. The studies include the reaction of OH radicals with saccharides, amide, and urea. Several also exist for the reaction of OH radical with organic molecules in the gas phase. Both the gas-phase studies and the bulk solution studies were used as foundation blocks for this study.¹⁰⁻¹³

In this chapter results of the oxidation of several organic solutes in aqueous aerosols are presented. The results are presented with the aim to show: the influence of partitioning on heterogeneous oxidation, the effect of particle composition evolution on particle size, the effect of particle size on reactivity of a solute, and the influence of coexisting components on the oxidation of another component. The results also seek to demonstrate that the oxidation of a solute in an aqueous aerosol particle is dependent of its accesses to the interface. Table 5.1 lists the solutions made and used to generate the aqueous aerosols for this study.

Table 5.1 List of aqueous solutions used to generate aerosols along with available corresponding density, viscosity, and surface tension data.

Solute	Concentration mol L⁻¹	Density(ρ) (Kg/m³)	Viscosity (mPa.s)	Surface tension (mNm⁻¹)
MGP	0.0258	-	-	-
Glucose	0.0258	0.999 ⁽¹⁴⁾	0.92 ⁽¹⁴⁾	75 ⁽¹⁵⁾
Urea	0.0258	0.997 ⁽¹⁶⁾	0.89 ⁽¹⁷⁾	72 ^(18,19)
Water		0.997 ⁽²⁰⁾	0.89 ⁽²¹⁾	72 ⁽²²⁾
Propionamide	0.0258	-	-	-
Acetamide	0.0258	0.997 ⁽²³⁾	0.89 ⁽²⁴⁾	-
MGP	0.0129	-	-	-
Urea	0.0129	-	-	-
MGP	0.0129	-	-	-
Propionamide	0.0129	-	-	-

5.2 MD simulation

MD simulations were done to determine the effect of the gas phase oxidant, OH radical, on the size of aqueous particles. The simulations were setup as described in chapter 3. However, the content of the water box was kept constant, 13 000 water, 120 MGP, and 120 urea molecules, while varying the number of OH radicals from 0 to 360.

5.3 Experimental results

5.3.1 Particle size characterization

Table 5.2 Mean diameter of aerosol particles made from different solutions.

Particle	Mean weighted Diameter(nm)
MGP	255.0 (± 2.0)
Glucose	252.0 (± 1.0)
MGP-Urea	230.6 (± 1.4)
MGP-Pram	237.7 (± 1.3)
Urea	176.5 (± 1.3)
Water	91.9 (± 0.8)
Propionamide	92.7 (± 1.6)
Acetamide	107.6 (± 0.9)

Table 5.3 Mean number of aerosol particles made from different solutions.

Particle	# /cm³ Particles 0 OH exposure	#/cm³ Particles Max OH exposure
MGP	490000 (± 6300)	340000 (± 13000)
Glucose	410000 (± 2900)	260000 (± 3400)
MGP-Urea	430000 (± 1800)	370000 (± 1700)
MGP-Pram	330000 (± 2700)	260000 (± 3000)
Urea	160000 (± 2600)	150000 (± 2100)
Water	57000 (± 1100)	57000 (± 800)
Propionamide	29000 (± 700)	30000 (± 800)
Acetamide	31000 (± 900)	32000 (± 900)

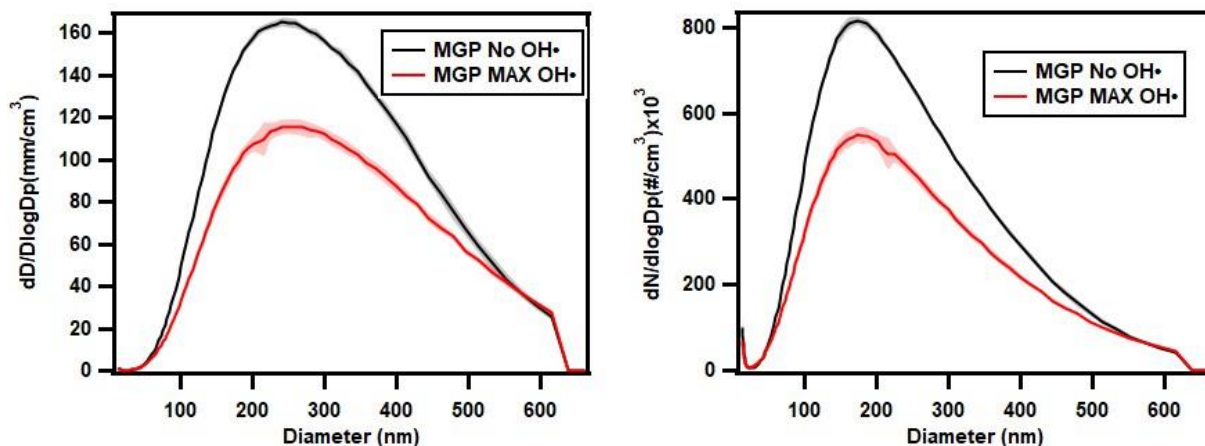


Figure 5.1 Particle size distribution for an aerosol generated from a pure MGP solution before exposure to OH radical (black) and after (red). Left) size distribution expressed as diameter concentration(mm/cm^3) and right) size distribution expressed as number concentration ($\#/\text{cm}^3$).

Figure 5.1 displays the particle size distribution of an aerosol generated from an aqueous solution of MGP (relative humidity of 100%). The displayed particles range from 14.3nm to 673.2nm in diameter due to the cutoff limits of the SMPS method limitations. The graphs indicated that when the aerosol is exposed to the maximum amount of OH radical the particle number concentration decreases considerably, reaching up to 38%. The diameters over which the particles are distributed do not change and the weight given to each diameter remains unchanged relative to the other diameters after exposure to OH radical.

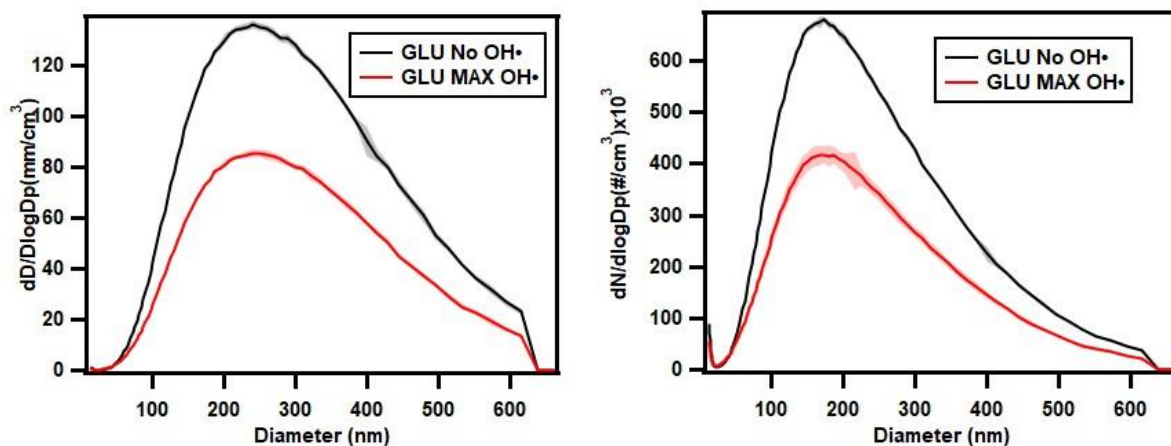


Figure 5.2 Particle size distribution for an aerosol generated from a pure glucose solution before exposure to OH radical (black) and after (red). Left) size distribution expressed as diameter concentration (mm/cm^3) and right) size distribution expressed as number concentration ($\#/\text{cm}^3$).

Figure 5.2 displays the particle size distribution of an aerosol generated from an aqueous solution of glucose (Table 5.1). Like MGP solution results (Figure 5.1), graphs indicated that when the aerosol is exposed to the maximum amount of OH radical the particle number concentration decreases considerably. The diameters over which the particles are distributed do not change and the weight given to each diameter remains unchanged relative to the other diameters after exposure to OH radical. Figure 5.2 also shows the number of particles generated using the MGP solution is greater than that generated using the glucose solution.

Figure 5.3 displays the particle size distribution of an aerosol generated from an aqueous solution of urea (Table 5.1). The graphs indicated that when the aerosol is exposed to the maximum amount of OH radical the particle number concentration decreases, however, the decrease is less pronounced as compared to that of MGP and glucose. The diameters over which the particles are distributed show a slight shift to lower diameters, and weight given to each diameter increases in favor of lower diameters. Figure 5.3 also shows the number of particles generated using the urea solution is far less than that generated using the MGP or Glucose solutions. This is expected

because of the difference in molecule size, mass and density of solution. However, partitioning properties of the three molecules would suggest all three having almost similar number and diameter concentrations.

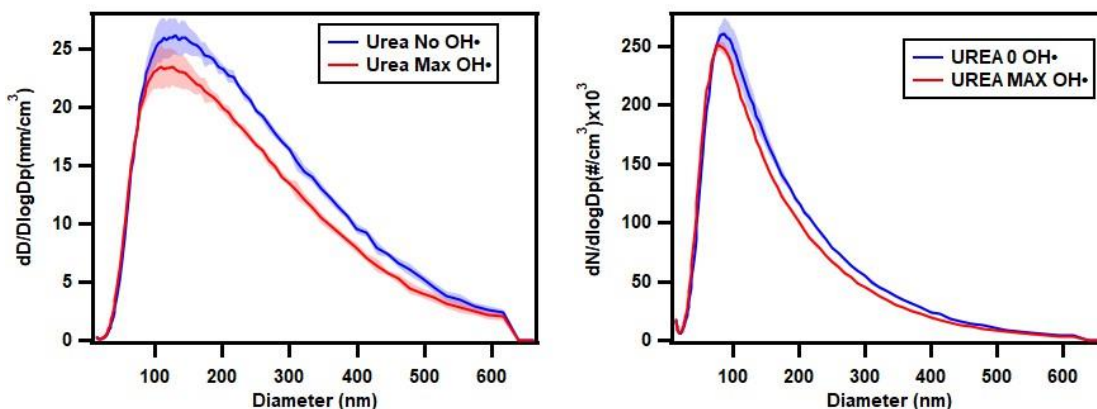
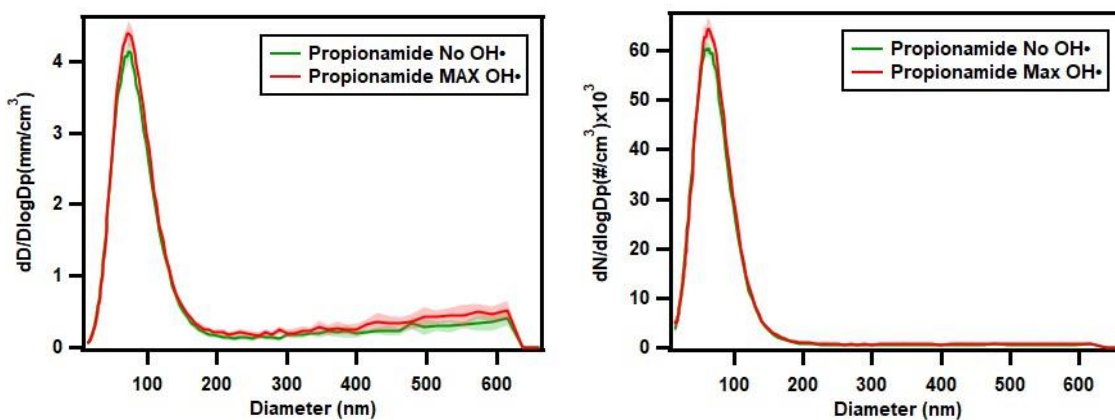


Figure 5.3 Particle size distribution for an aerosol generated from a pure urea solution before exposure to OH radical (blue) and after (red). Left) size distribution expressed as diameter concentration(mm/cm^3) and right) size distribution expressed as number concentration ($\#/\text{cm}^3$).

Figure 5.4 and 5.5 displays the particle size distribution of an aerosol generated from aqueous solutions of propionamide and acetamide respectively (Table 5.1). The graphs indicated that when the aerosol is exposed to the maximum amount of OH radical the particle number concentration slightly increases. The diameters over which the particles are distributed do not change and the weight given to each diameter remains unchanged relative to the other diameters after exposure to OH radical. Figure 5.4 and Figure 5.5 also show that the number of particles generated using the acetamide or propionamide solutions is far less than that generated using the Urea, MGP or Glucose solutions.

Figure 5.6 displays a comparison of the particle size distributions of aerosols generated from aqueous solutions of propionamide(green), acetamide(purple), urea (dark blue) and pure water(black) respectively. The graphs indicated that aerosols generated by urea solution have the

highest particle number concentration, followed by water, acetamide and propionamide having the least. Figure 5.6 also indicated that the urea solution generated aerosols also have a wider range of particles and larger Particles. Figure 5.6 shows that solutions with a higher surface tension than water generate more and larger particles.



Figur 5.4 Particle size distribution for an aerosol generated from a pure propionamide solution before exposure to OH radical (green) and after (red). Left) size distribution expressed as diameter concentration(mm/cm^3) and right) size distribution expressed as number concentration ($\#/\text{cm}^3$).

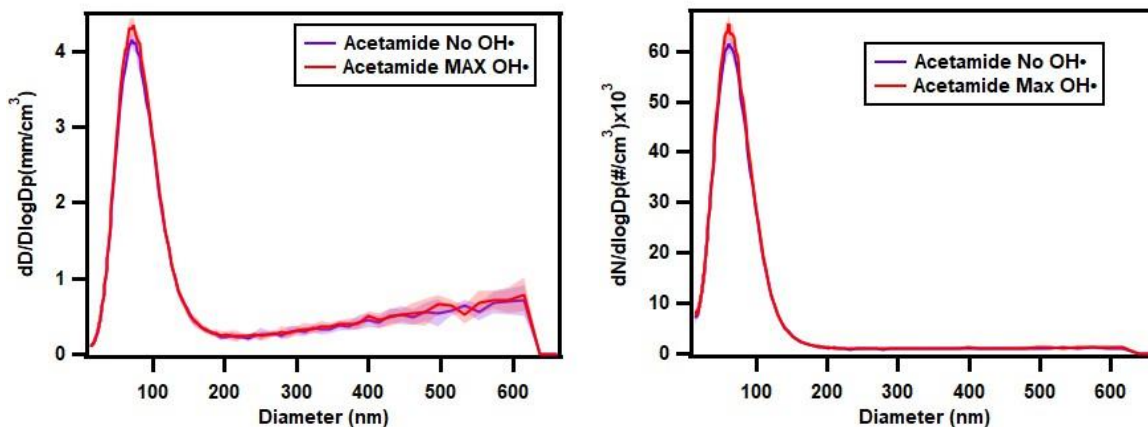


Figure 5.5 Particle size distribution for an aerosol generated from a pure acetamide solution before exposure to OH radical (purple) and after (red). Left) size distribution expressed as diameter concentration(mm/cm^3) and right) size distribution expressed as number concentration ($\#/\text{cm}^3$).

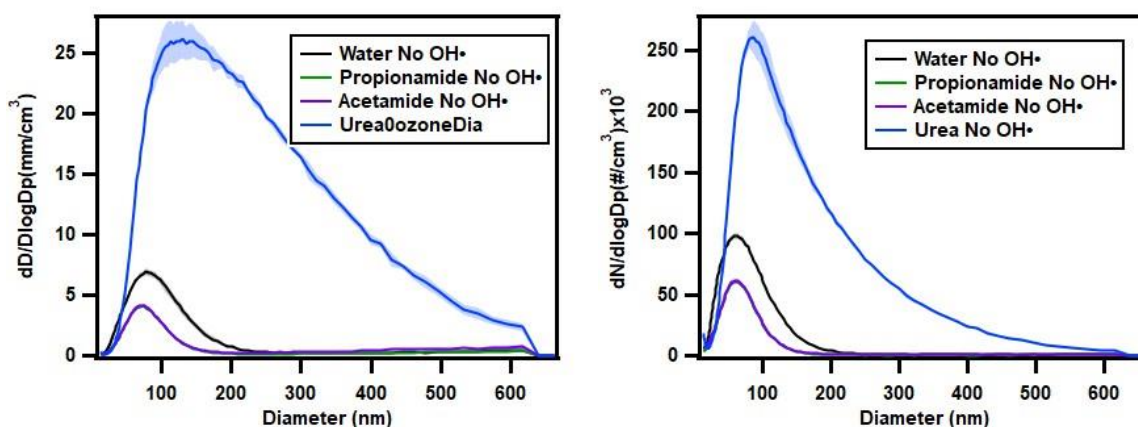


Figure 5.6 Particle size distribution for aerosols generated from a pure Urea solution (dark Blue), water (turquoise), acetamide (purple), and propionamide (green) before exposure to OH radical. Left) size distribution expressed as diameter concentration(mm/cm^3) and right) size distribution expressed as number concentration ($\#/\text{cm}^3$).

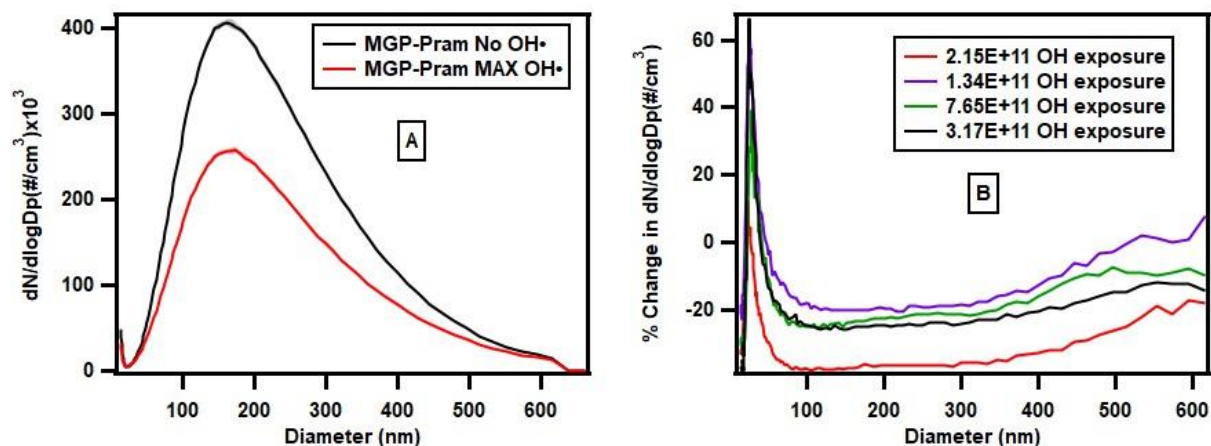


Figure 5.7 a) Particle size distribution for an aerosol generated from a pure MGP-Propionamide solution before exposure to OH radical (purple) and after (red), size distribution expressed as number concentration ($\#/cm^3$). b) Percentage change in number concentration ($\#/cm^3$) at different OH exposures.

Figure 5.7 displays the particle size distribution of an aerosol generated from an aqueous solution containing MGP and Propionamide (Table 5.1). Figure 5.7 a) indicated that when the aerosol is exposed to the maximum amount of OH radical the particle number concentration decreases considerably. The diameters over which the particles are distributed do not change and the weight given to each diameter remains unchanged relative to the other diameters after exposure to OH radical. Figure 5.7 a) also shows the number of particles generated using the MGP-Propionamide solution is less than that generated using the MGP and glucose solution. The most abundant particles have a count of 8.2×10^5 ($\#/cm^3$), 6.8×10^5 ($\#/cm^3$), and 4.1×10^5 ($\#/cm^3$), for MGP, glucose and MGP-propionamide aerosols respectively. Table 5.3 also displays the difference in the total number of particles per cm^3 . Figure 5.7 b) displays the percentage change in particle number concentration per diameter with varying OH exposure of an aerosol generated from MGP-propionamide aqueous solution. The graphs indicate that the particle number concentration of smaller particles increases when the aerosol is exposed to OH radicals, up to

66% particle gain. All the other particles experience a decrease in number concentration, with particles ranging from 80nm to 450nm experiencing the greatest decrease in number density up to 37% particle loss. A similar behavior is also observed for the aerosols generated from single solute solutions that experience significant change in number and diameter concentration, MGP, glucose and urea Figure 5.7 b) also indicates that while the highest OH exposure gives the greatest percentage change always, there is no clear correlation between the amount of OH exposure and percentage change.

5.3.2 Kinetic results

The decay rate of reactants in the equimolar aerosol particles due to oxidation with OH radicals can be expressed by the following equation:

$$\frac{[M]_t}{[M]_0} = \exp(-k \langle \text{OH} \rangle \cdot t) \quad (5.1)$$

where k ($\text{cm}^3 \text{s}^{-1}$) is the second-order rate constant for OH oxidation, and $[M]_t$ and $[M]_0$ are the concentrations of reactant before and after oxidation with OH radical, and $\langle \text{OH} \rangle \cdot t$ is the OH exposure. The rate coefficient for heterogenous process is dependent on particle size, this makes it inappropriate for use to compare the reactivity of systems with different particle sizes. The best term to express and compare the reactivity of aerosol particles is the reactive uptake:

$$\gamma_{eff} = \frac{2kd_p\rho_0N_A}{3cM} \quad (5.2)$$

Table 5.4 Reaction and diffusion parameters from bulk solution studies.

	OH Rate coefficient ($\text{cm}^3 \text{s}^{-1}$)	Bulk diffusion coefficient ($\text{cm}^2 \text{s}^{-1}$)
MGP	5.8×10^{-12} (1)	4.5×10^{-6} (25)
Urea	-	1.4×10^{-5} (26)
Propionamide	1.78×10^{-12} (27)	1.2×10^{-5} (26)
Acetamide	$(0.4-1.1) \times 10^{-12}$ (27)	1.25×10^{-5} (23,28)
OH	-	2.8×10^{-5} (29)

Table 5.5 Rate constant and uptake coefficients for the heterogeneous oxidation of organic compounds in aqueous aerosol particles.

Particle composition	Rate coefficient ($\text{cm}^3 \text{s}^{-1}$)	Uptake coefficients
MGP	$1.2(\pm 0.1) \times 10^{-11}$	$8.5(\pm 0.7)$
Urea	$8.0(\pm 0.6) \times 10^{-12}$	$18.2(\pm 1.4)$
MGP	$4.7(\pm 0.3) \times 10^{-12}$	$3.3(\pm 0.2)$
Propionamide	$1.1(\pm 0.1) \times 10^{-11}$	$21.2(\pm 1.9)$
Urea	$1.1(\pm 0.6) \times 10^{-11}$	$17.5(\pm 9.5)$
MGP	$1.1(\pm 0.1) \times 10^{-11}$	$8.6(\pm 0.8)$

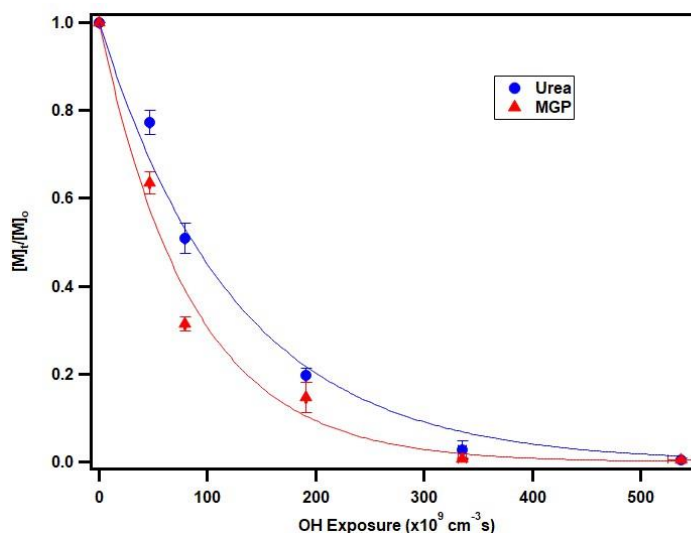


Figure 5.8 Relative signal of unreacted urea (blue dots) and methyl β -D-glucopyranoside (red triangles) in mixed equimolar aqueous aerosols as a function of OH exposure. The solid lines are exponential fits to the experimental data over the whole full range.

Figure 5.8 displays the relative signal of urea (blue dots) and MGP (red triangles) reactants in aqueous aerosols as a function of OH exposure. Each displayed data points are an average of three independent measurements taken under the same conditions. The solid lines represent exponential fits applied to the experimental data. The exponential fit on urea gives back a rate coefficient of $8.0(\pm 0.6) \times 10^{-12} \text{ cm}^{-3}\text{s}^{-1}$ and $1.2(\pm 0.1) \times 10^{-11} \text{ cm}^{-3}\text{s}^{-1}$ for urea and MGP respectively.

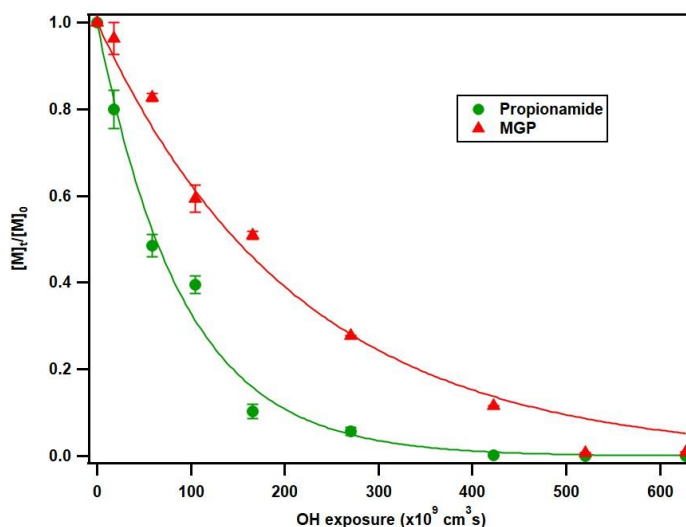


Figure 5.9 Relative signal of unreacted propionamide (green dots) and methyl β -D-glucopyranoside (red triangles) in mixed equimolar aqueous aerosols as a function of OH exposure. The solid lines are exponential fits to the experimental data over the whole full range.

Figure 5.9 displays the relative signal of propionamide (green dots) and MGP (red triangles) reactants in aqueous aerosols as a function of OH exposure. Each displayed data points are an average of three independent measurements taken under the same conditions. The solid lines represent exponential fits applied to the experimental data. The exponential fit on propionamide gives back a rate coefficient of $1.1(\pm 0.1) \times 10^{-11} \text{ cm}^{-3}\text{s}^{-1}$ and $4.7(\pm 0.3) \times 10^{-12} \text{ cm}^{-3}\text{s}^{-1}$ for propionamide and MGP respectively.

The good exponential fits for all the traces in Figure 5.8 and 5.9 are suggestive of all the reaction proceeding via pseudo first order. This affirms that the reactions are not governed by the diffusion of the reactants. The uptake coefficients were calculated accordingly and are presented in Table 5.5 alongside the rate coefficients.

5.4 Discussion

5.4.1 Particle characterization

Using water as the reference point, the solutions under study shown in Table 5.1 can be divided into two distinct groups. Group one made up of solutions that generate a higher number of particles over a wider range of diameters than pure water upon atomization. Group two made up of solutions that generate a lower number of particles and have a shorter range of diameters. Solutions made of molecules with relatively lower partitioning coefficients (K_p), glucose, MGP, and urea make up group one. Solutions made up of molecules with relatively higher K_p values, acetamide, and propionamide, make up group two. The liquid properties that are important to atomization are surface tension, viscosity, and density (Table 5.1). The difference in the number concentration and particle size distribution of these solution implies that the addition of the above mention solutes to water greatly alter the density, viscosity, and/or surface tension of water. Surface tension influences the stability of the fluid by resisting the formation of new surfaces, and fluids with higher surface tension tend to have larger particles³⁰. Following this logic, results shown in Figures 5.1 to 5.3 show that solutions made from group one molecules have a higher surface tension than water, while Figures 5.4 to 5.5 show that solutions from group two molecules have a lower surface tension. This gives a bit of confidence that surface active molecules and surface inactive molecules maintain their partitioning properties even in nanoparticles. However, the observed difference could also be because of how the molecules

affect viscosity. Within group one, the noted difference in number concentration and size distribution can be attributed to a difference in the density of the solutions. Based on surface tension alone glucose and MGP solutions should give very similar results while urea solution should give a higher number concentration and larger particles. However, MGP-solution has the higher number concentration because of a higher density.

Figure 5.1 to 5.3 and Figure 5.7 a) all clearly indicate a loss of particles when aerosols MGP, glucose or urea are exposed to OH radical. Table 5.3 also indicates a significant change between initial total number of particles and total number of particles after exposure to OH. Several explanations can be given to rationalize the observation. Change in average size and particle number concentration due to water evaporation in response to relative humidity changes can be ruled out on the basis that the relative humidity (RH) before exposure to OH and after is the same ~100% (wet aerosols were never dried). A simple water diffusion-controlled³¹ evaporation can also be ruled out on the fact that the high RH conditions do not encourage such evaporation, and in the event this was happening the effect would be the same before and after exposure to OH radicals³². The next possibility would be evaporation of water from the particles that is induced by the presence of the gas phase oxidant, OH radical, at/or near the air-water interface. The presence of the OH radical does affect interfacial properties as has been shown for surface tension in chapter 3. However, our MD simulation studies suggest that there is no significant change in movement of water molecules (evaporation) from the surface to the gas-phase with increase in OH radicals. The increase in the number of OH radicals does not affect the overall distribution of water molecule in the simulation. The MD simulation results reduce the merit of the OH radical induced water evaporation. In this study solute composition has been shown to contribute immensely to aerosol particle size distribution and number concentration (Figure 5.1

to 5.7). Therefore, it is a plausible explanation that the change in number particle experienced after exposure to OH radicals is due to particle composition change. The composition change being due to the oxidation of the initial solute by OH radical to form smaller molecules and molecules with higher K_p values. Such a change in composition would reduce particle solution density and surface tension which in turn would lead to secondary atomization^{5-7,30}. Secondary atomization is the breakdown of larger aerosol particles into much smaller particles or total disintegration. Results displayed in Figure 5.7 b) suggest secondary atomization, looking at the change per diameter it is apparent that while larger particles ($> 80\text{nm}$) are lost, some smaller particles ($< 80\text{nm}$) are gained. The results in Figure 5.4 to 5.5 which show that no significant change in number concentration is observed for particle made from solutes with high K_p and low density, can be justified by this same explanation. For the acetamide and propionamide aerosols no new solutes formed are significantly different from the initial solutes, hence no change in number concentration or particle size distribution. The previous explanation assumes a mass conservation for the solute and a water mass flux between the gas-phase and particle. However, another possibility would be a loss of both water and solute. The oxidation of solute by OH radical could lead to the formation of volatile and semi-volatile components that leave the particle on formation and subsequently cause the loss of water molecules from the particle. while the last two explanations a plausible, there is need for further investigation into the oxidation products and the effect of composition change.

5.4.2 Kinetics

Information from bulk aqueous solution studies was used as the foundation for this study, mostly to validate major assumptions. Using bulk solution diffusion coefficients (Table 5.4) and mean particles diameters (Table 5.3), the time taken by each analyte to fully sample a spherical volume

of diameter equal to the mean diameter of appropriate aerosol was determined. The obtained times are several orders of magnitude smaller than the reaction time 18 s. This eliminates difference in diffusion of molecules in the aerosol particles as a cause for any observed reactive differences. The reactivity of the analytes of interest towards OH radical in bulk solutions are similar. This similarity is shown by the reaction rates coefficient which are in close proximity of each other (Table 5.4).

The two rate coefficients obtained for methyl β -D-glucopyranoside are both different from the bulk solution value. The rate coefficient from the MGP-Urea ($1.2(\pm 0.1) \times 10^{-11}$) solution was higher than the bulk value (5.8×10^{-12}), while that value from the MGP-Propionamide ($4.7(\pm 0.3) \times 10^{-12} \text{ cm}^3\text{s}^{-1}$) was lower than the bulk value. The two rate coefficients seem to suggest that the reactivity of MGP towards the OH radical increases slightly in aerosols which include a highly surface inactive molecule (Urea) and is reduced in the presence of surface-active molecules (propionamide). However, the aerosol size distributions for the two solutions are different and hence rate coefficients cannot be used to make such a conclusion. Particle size is a major contributor to heterogenous reactivity, hence the reactivity of MGP in these two aerosols are best compared using uptake coefficients. The uptake coefficient determined for MGP from the oxidation of the MGP-Propionamide aqueous aerosol is $3.3(\pm 0.2)$, while that determine for MGP from the oxidation of the MGP-Urea is $8.5(\pm 0.7)$ (see Table 5.5). The uptake coefficients show that the reactivity of MGP towards OH radicals is higher in particles containing urea (a surface inactive molecule) as compared to particles containing propionamide (a surface-active molecule). The reactive uptake coefficient for MGP ($8.6(\pm 0.8)$) determined from the oxidation of just MGP aqueous aerosol is similar to the one determined from MGP-Urea aqueous aerosol. This suggests that the reactivity of MGP was suppressed by the presence of propionamide in the

MGP-Propionamide aerosol. Assuming that surface reactions dominate heterogeneous oxidation, this observation can be explained by the difference in partitioning ability of Urea, MGP and propionamide between the gas and particle bulk liquid phase. The partitioning difference of the compounds are quantitatively demonstrated by the Gibbs free energy of partitioning calculate from solvent accessible surface area (SASA). Propionamide has a negative $\Delta_p G^o$, which suggests a high concentration at the particle surface, while the $\Delta_p G^o$ positive values of MGP and Urea indicate a higher concentration in the particle bulk than at the surface. Molecular dynamics studies presented in chapter 3 of this thesis, demonstrate the partitioning differences of the three components and the difference of interaction with the gas phase oxidant. MGP and Urea are shown to be highly surface inactive spending over 50% of the simulation time in the particle bulk. Propionamide is highly surface active spending over 50% at the particle surface. The MD simulation show that OH radical spends an average of 45% of the simulation time at the surface, 24% in the gas phase, and the remaining 31% in the bulk. The simulation show that the molecules with high surface activity have a higher chance to interact with the gas phase oxidant. The MD simulations also show that the solvation structure of the molecules in the bulk and at the interface are also very different, with bulk solvation including multiple solvation shells that increase the energy cost of reactive interactions.³³ The OH radical is shown to be able to penetrate the second and first solvation shell of the solutes at the interface, something that was rare in the particle bulk. The simulations suggest stronger interactions between OH radical and the particle reactants when at the surface as compared to the bulk. However, the simulation also show that in the event of none reactive coexistence, one solute does not affect the partitioning and solvation properties of another solute. The change in the reactivity of MGP in the different aerosols also seem to suggest that heterogeneous oxidation mainly occurs at the interface. The

reactivity of MGP is suppressed by restricted access to the interface caused by the presence of the surface active propionamide. The reduced reactivity of the MGP could also be due to the increased competition for OH radicals at the interface. The propionamide which is present at the interface in larger quantities reacts with the OH radical before it can react with the MGP molecules being supplied slowly from the particle bulk. The uptake coefficient determined for urea from the oxidation of the MGP-Urea aqueous aerosol is $18.2(\pm 1.4)$, while that determined for urea from the oxidation of the Urea only aqueous aerosol is $17.5(\pm 9.5)$. The uptake coefficients show that the reactivity of urea towards OH radicals is not significantly altered by the presence of MGP in the particles. The particle size distribution is significantly different between MGP-urea aerosols and Urea only aerosol. However, the similarity in the uptake coefficients of Urea seem to suggest that the size of the particle did not affect the uptake of the gas-phase reactants.

5.5 Conclusion

The heterogeneous oxidation of multi-component aqueous aerosols particles show a difference in reactivity for a monosaccharide with changing aerosol composition. Methyl β -D-glucopyranoside (MGP) displayed a much higher reactive uptake coefficient when in a particle consisting of a surface inactive molecule, urea, as compared to when in a particle consisting of a surface active molecule, propionamide. The difference in reactivity of the MGP in the different aerosols seems to be due to difference in access to the particle surface and competitive reactions occurring at the surface. The kinetic data coupled with MD simulation presented in chapter 3 and available partitioning data all suggest that solutes sharing the same particle do not alter each other's mobility and overall distribution in the particle. This only applies for molecules that share a non-reactive coexistence. The kinetic data presented here reaffirms the effect of partitioning on the reactivity of components in aqueous atmospheric aerosols.

The physical particle characterization of aerosols demonstrates the change in particle diameter with change of the particle chemical composition and change in number concentration when exposed to OH radicals. The data allows for the discussion of the causes of change in particle size with chemical aging. Using MD simulation the study dismissed the idea of the gas-phase oxidate having any contribution to particle size change before reacting with the particle components. The diffusion of water molecules from the aerosol particles to the gas phase due to low relative humidity is also discredited. The results favor change in particle size due to change in chemical composition that results in secondary atomization and change due to leaving products. The inclusion of the finding of this study in atmospheric chemistry models will help improve the predictive power of these models.

Reference

1. Fan H, Wenyika Masaya T, Goulay F. Effect of surface-bulk partitioning on the heterogeneous oxidation of aqueous saccharide aerosols. *Phys Chem Chem Phys*. 2019;21(6):2992-3001. doi:10.1039/c8cp06785f
2. Malila J, Prisle NL. A Monolayer Partitioning Scheme for Droplets of Surfactant Solutions. *J Adv Model Earth Syst*. 2018;10(12):3233-3251. doi:10.1029/2018MS001456
3. George IJ, Abbatt JPD. Heterogeneous oxidation of atmospheric aerosol particles by gas-phase radicals. *Nat Chem*. 2010;2(9):713-722. doi:10.1038/nchem.806
4. Shiraiwa M, Zuend A, Bertram AK, Seinfeld JH. Gas-particle partitioning of atmospheric aerosols: Interplay of physical state, non-ideal mixing and morphology. *Phys Chem Chem Phys*. 2013;15(27):11441-11453. doi:10.1039/c3cp51595h
5. Chen Y, Demauro EP, Wagner JL, et al. Aerodynamic Breakup and Secondary Drop Formation. 2017;(2011):1-15.
6. Atomizer SP swirl. 17-20 May 1998 The Doubletree Hotel Sacramento , · california. 2015;(August).
7. Davanlou A, Lee JD, Basu S, Kumar R. Effect of viscosity and surface tension on breakup and coalescence of bicomponent sprays. *Chem Eng Sci*. 2015;131(March 2018):243-255. doi:10.1016/j.ces.2015.03.057
8. Fletcher NH. Size Effect in Heterogeneous Nucleation. *J Chem Phys*. 1958;29(3):572-576. doi:10.1063/1.1744540
9. Thanh NTK, Maclean N, Mahiddine S. Mechanisms of nucleation and growth of

- nanoparticles in solution. *Chem Rev.* 2014;114(15):7610-7630. doi:10.1021/cr400544s
10. Guay DF, Cole BJW, Fort RC, Genco JM, Hausman MC. Mechanisms of Oxidative Degradation of Carbohydrates During Oxygen Delignification. I. Reaction of Methyl β -D-Glucopyranoside with Photochemically Generated Hydroxyl Radicals. *J Wood Chem Technol.* 2000;20(4):375-394. doi:10.1080/02773810009351890
 11. Minakata D. Development of aqueous phase hydroxyl radical reaction rate constants predictors for advanced oxidation processes. *ProQuest Diss Theses.* Published online 2010:395.
http://search.proquest.com/docview/862297334?accountid=10673%5Cnhttp://openurl.ac.uk/athens:_edu?url_ver=Z39.88-2004&rft_val_fmt=info:ofi/fmt:kev:mtx:dissertation&genre=dissertations+%26+theses&sid=ProQ:ProQuest+Dissertations+%26+Theses+Global&atitle=&tit
 12. Nbs 46.
 13. Hayon E, Iyata T, Lichtin NN, Simic M. Sites of Attack of Hydroxyl Radicals on Amides in Aqueous Solution. *J Am Chem Soc.* 1970;92(13):3898-3903. doi:10.1021/ja00716a011
 14. Ali A, Bidhuri P, Malik NA, Uzair S. Density, viscosity, and refractive index of mono-, di-, and tri-saccharides in aqueous glycine solutions at different temperatures. *Arab J Chem.* 2019;12(7):1684-1694. doi:10.1016/j.arabjc.2014.08.027
 15. Petters SS, Petters MD. Journal of geophysical research. *Nature.* 1955;175(4449):238. doi:10.1038/175238c0
 16. Halonen S, Kangas T, Haataja M, Lassi U. Urea-Water-Solution Properties: Density,

- Viscosity, and Surface Tension in an Under-Saturated Solution. *Emiss Control Sci Technol.* 2017;3(2):161-170. doi:10.1007/s40825-016-0051-1
17. Kawahara K, Tanford C. Viscosity and density of aqueous solutions of urea and guanidine hydrochloride. *J Biol Chem.* 1966;241(13):3228-3232. doi:10.1016/s0021-9258(18)96519-1
 18. Kapusta ŁJ, Sutkowski M, Rogóż R, Zommara M, Teodorczyk A. Characteristics of water and urea-water solution sprays. *Catalysts.* 2019;9(9). doi:10.3390/catal9090750
 19. Birkhold F, Meingast U, Wassermann P, Deutschmann O. Analysis of the injection of urea-water-solution for automotive SCR DeNO_x-systems: Modeling of two-phase flow and spray/wall-interaction. *SAE Tech Pap.* 2006;(May 2014). doi:10.4271/2006-01-0643
 20. Tanaka M, Girard G, Davis R, Peuto A, Bignell N. Recommended Table for the Density of Water Between 0 °C and 40 °C Based on Recent Experimental Reports. *Metrologia.* 2003;38:301. doi:10.1088/0026-1394/38/4/3
 21. Kiselev SP, Vorozhtsov E V., Fomin VM. Ideal Fluid. Published online 2017:187-266. doi:10.1007/978-3-319-66149-0_4
 22. Hauner IM, Deblais A, Beattie JK, Kellay H, Bonn D. The Dynamic Surface Tension of Water. *J Phys Chem Lett.* 2017;8(7):1599-1603. doi:10.1021/acs.jpcclett.7b00267
 23. Christoffers HJ, Kegeles G. The Diffusion Coefficients, Densities, and Viscosities of Solutions of Acetamide in Water. *J Am Chem Soc.* 1963;85(17):2562-2565. doi:10.1021/ja00900a005
 24. Makarov DM, Egorov GI, Kolker AM. Volumetric Properties of Aqueous Solutions of

- Acetamide in the 274.15–333.15 K Range of Temperatures. *Russ J Phys Chem A Focus Chem*. 2020;94(4):693-697. doi:10.1134/s0036024420040111
25. Dunlop PJ, Gosting LJ. A Study of the Diffusion of Glycolamide in Water at 25° with the Gouy Interference Method. *J Am Chem Soc*. 1953;75(20):5073-5075.
doi:10.1021/ja01116a051
 26. Institutes N. lithium /. 1969;78(4):1963-1964.
 27. Borduas N, da Silva G, Murphy JG, Abbatt JPD. Experimental and theoretical understanding of the gas phase oxidation of atmospheric amides with OH radicals: kinetics, products, and mechanisms. *J Phys Chem A*. 2015;119(19):4298-4308.
doi:10.1021/jp503759f
 28. Winkelmann J. Diffusion coefficient of 2-methylpropyl-benzene in cyclohexane. *Diffus Gases, Liq Electrolytes*. Published online 2018:1334-1334. doi:10.1007/978-3-662-54089-3_899
 29. Codorniu-Hernández E, Kusalik PG. Mobility mechanism of hydroxyl radicals in aqueous solution via hydrogen transfer. *J Am Chem Soc*. 2012;134(1):532-538.
doi:10.1021/ja208874t
 30. Ejim CE, Rahman MA, Amirfazli A, Fleck BA. Effects of liquid viscosity and surface tension on atomization in two-phase, gas/liquid fluid coker nozzles. *Fuel*. 2010;89(8):1872-1882. doi:10.1016/j.fuel.2010.03.005
 31. Wallace BJ, Preston TC. Water Uptake and Loss in Viscous Aerosol Particles with Concentration-Dependent Diffusivities. *J Phys Chem A*. 2019;123(15):3374-3382.

doi:10.1021/acs.jpca.9b00907

32. Combe NA, Donaldson DJ. Water Evaporation from Acoustically Levitated Aqueous Solution Droplets. *J Phys Chem A*. 2017;121(38):7197-7204.

doi:10.1021/acs.jpca.7b08050

33. Gallo Jr. A, Muskopf NH, Liu X, et al. On the formation of hydrogen peroxide in water microdroplets. *Chem Sci*. 2022;13(9):2574-2583. doi:10.1039/d1sc06465g

6 Conclusion

The thesis captures research work done to investigate three key areas in the heterogeneous oxidation of aqueous organic aerosols:

- The effect of intramolecular interaction between coexisting solutes, the solvent, and the gas-phase reactant, on chemical and physical evolution of aqueous aerosols.
- The effect of chemical composition change on the reactivity of reactive species in the aqueous aerosols.
- The importance of interfacial interactions and reaction on the heterogeneous oxidation of aqueous aerosols.

Detailed below in sections 6.1 and 6.2 are the major conclusions of this study

6.1 MD simulation studies

- (1) Bulk properties are reached within the first 2 nm of the surface. Surface active molecules are found to accumulate within the top 2 nm of the droplet while surface inactive molecules form a depletion zone at the surface. For a particle containing a mixture of urea and acetamide, the properties of the outer phase are solely defined by acetamide, while those of the inner phase are mostly defined by urea. The MD simulations also show that the OH radicals preferentially accumulate within the 2-nm interfacial region. The dimension of the interface is comparable to the diffusion–reaction length (~1–2 nm) of the radical under reactive conditions. This overlap is likely to lead to interface-specific reaction mechanisms and kinetics. For aqueous aerosol for which diffusion of the reactants to the surface is not the rate limiting step, surface active molecules are rapidly consumed while surface inactive molecules are shielded from direct reaction with the oxidant.

- (2) Surface active solutes lose rotational freedom and orient themselves with the hydrophobic group pointing toward the water surface. Methyl-substituted glucose is mostly surface inactive with low surface concentrations but still displays a preferred surface orientation due to the presence of a methyl group. Hydrophobic organic groups will become more accessible for reaction, changing the likely reaction mechanism compared to that of the bulk. Such behavior is expected for surfactant with large alkyl chains and is shown to happen here for smaller molecules.
- (3) Reduced OH radical and solute solvation at the interface leads to an increased number of OH radicals coming into contact with surface active solutes. The number of water molecules in the radical and solutes solvation spheres is found to decrease considerably within the interface. The extent of this decrease depends on the molecular structure. This is also confirmed by a tighter interaction between the OH radical and the organic solute within the interface as observed in the radial pair distribution functions. The effects will contribute to a change in reaction rate coefficients within the interface compared to the bulk.

6.2 The kinetics of OH+aqueous organic particles

- (1) Heterogeneous oxidation of equimolar molar aqueous aerosol particles reveals a much higher reactive uptake coefficient for a monosaccharide, MGP, when in coexistence with a surface inactive molecule, urea, as compared to when in coexistence with propionamide. Such a behavior is not expected for molecules in aqueous solutions where the diffusion of the reactants has been shown not to be the rate limiting process. The difference in reactivity seems to be due to difference in partitioning properties and

competitive reactions at the surface of the particle. The finding also shows the importance of surface reactions over bulk reactions in the oxidation of atmospheric aerosol particles.

- (2) The reactive uptake coefficient of urea does not change with a change in the size of the aerosol particles being subjected to OH radical.

7 APPENDIX A

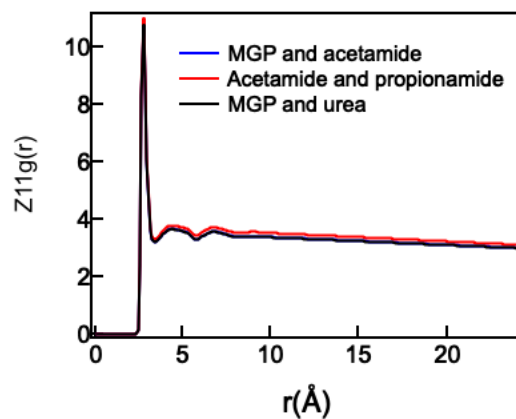


Figure A1 Radial pair distribution functions for water O-water O for different simulation setups.

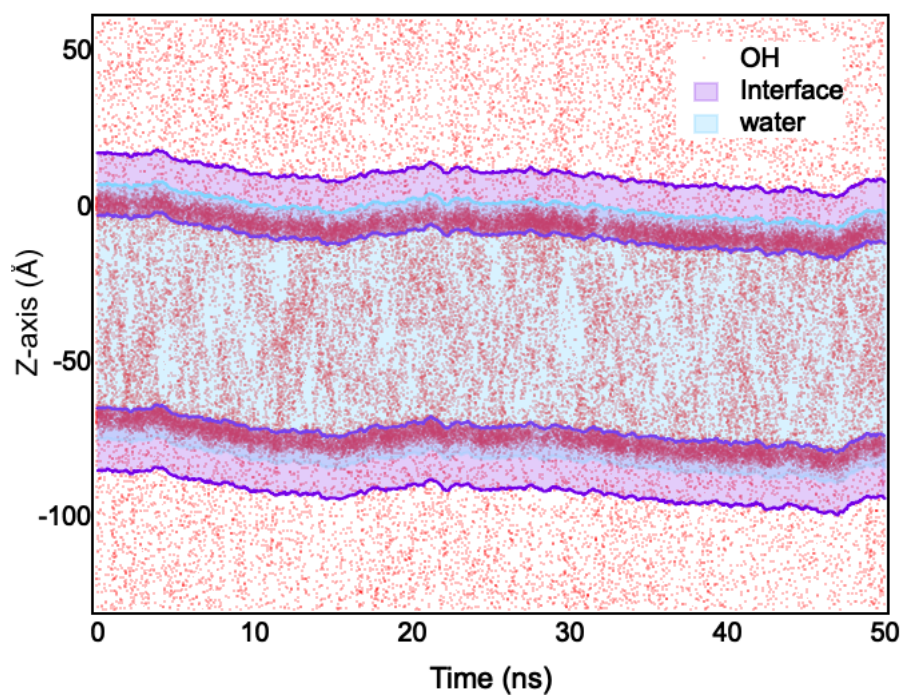


Figure A2 Scattering plot of 40 OH radicals (red dots) within the last 50 ns of the simulation. The interfacial region is indicated by the purple area, and the turquoise blue area represents the water box.

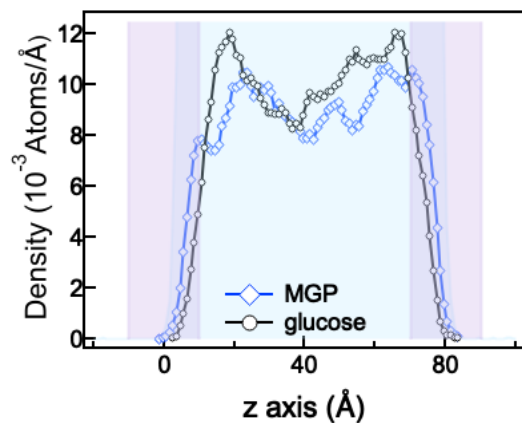


Figure A3. Density profiles of MGP (blue open diamonds) and glucose (black open circles), (b) acetamide (purple stars) and propionamide (open green triangles), and (c) acetamide (purple)

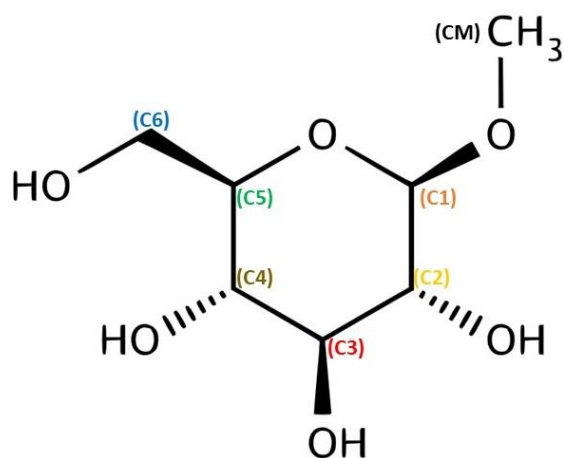


Figure A4. Labeling of the carbon atom in methyl b-D-glucopyranoside (MGP)

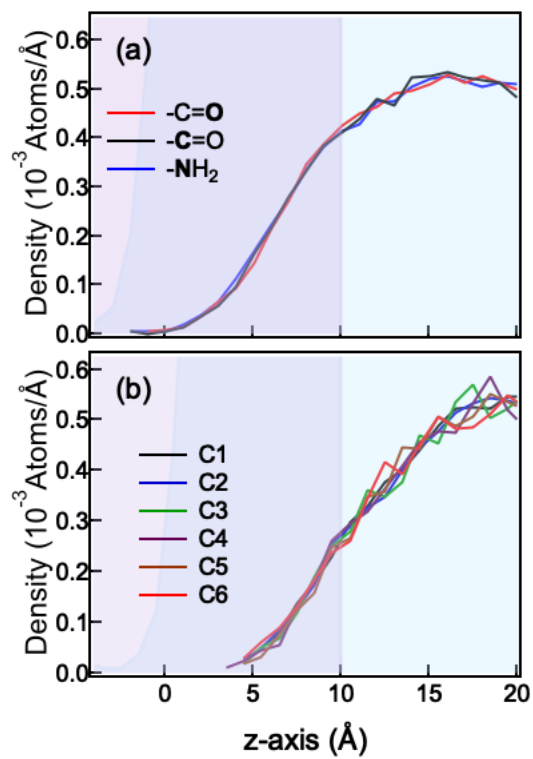


Figure A5. Atom density profiles for (a) urea and (b) glucose across the water-bulk (turquoise blue), air-water interface (purple) interface).

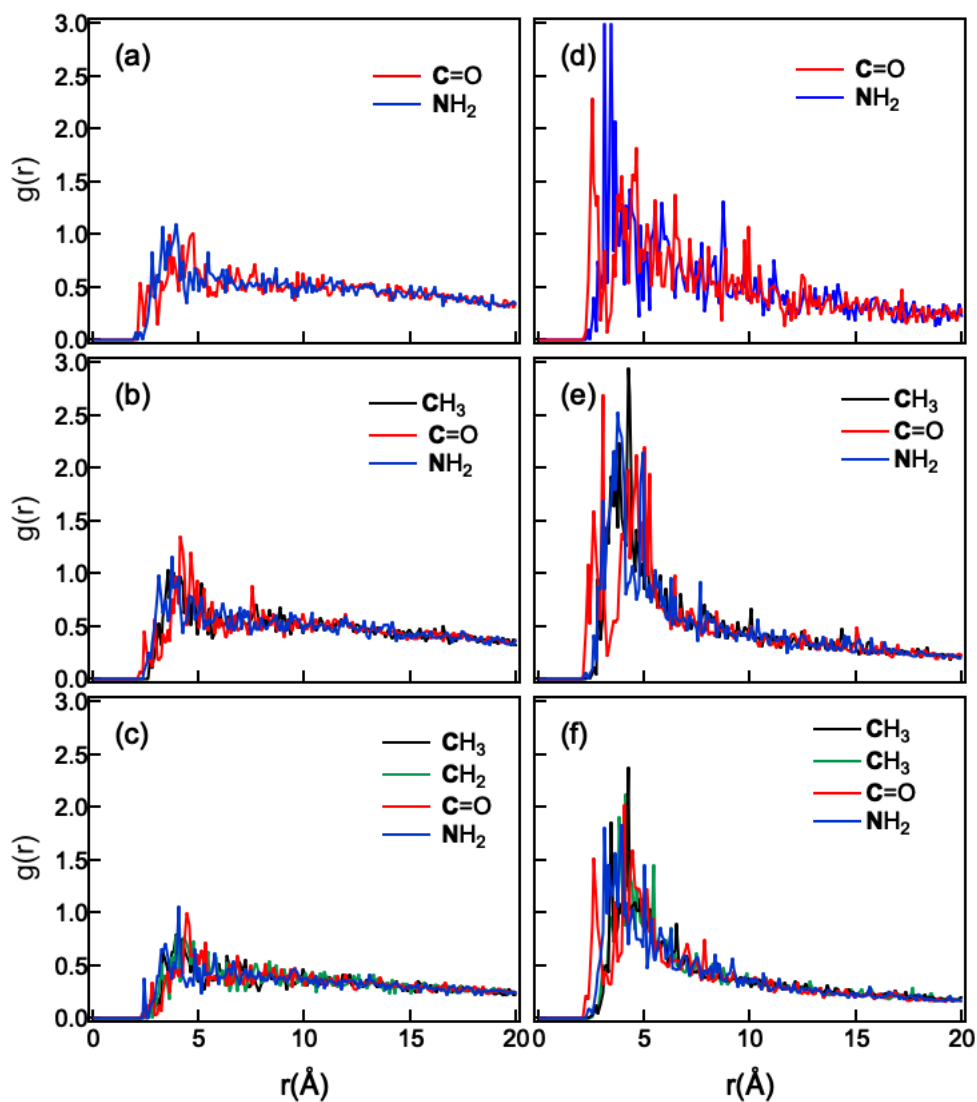


Figure A6. Radial pair distribution functions of the OH radical H atom with the nitrogen and carbon atoms of (a and d) urea, (b and e) acetamide, and (c and f) propionamide in the bulk (a, b, c) and at the air-water interface (d, e, f). The profiles are normalized by the area under the curve.